UiA University of Agder

Master

Numerical modelling, calibration and analysis of an offshore floating photovoltaic concept

KHAMZAT SAITOV

SUPERVISORS
Zhiyu Jiang, University of Agder (UiA)
Graeme Mackie, Oceanflow Energy Ltd

University of Agder, 2024
Faculty of Engineering and Science
Department of Engineering and Sciences

Individual/group Mandatory Declaration

The individual student or group of students is responsible for the use of legal tools, guidelines for using these and rules on source usage. The statement will make the students aware of their responsibilities and the consequences of cheating. Missing statement does not release students from their responsibility.

1.	I/We hereby declare that my/our report is my/our own work and that I/We have not used any other sources or have received any other help than mentioned in the thesis.	Yes
2.	**I/we further declare that this thesis:** • has not been used for another exam at another department/university/university college in Norway or abroad; • does not refer to the work of others without it being stated; • does not refer to own previous work without it being stated; • have all the references given in the literature list; • is not a copy, duplicate or copy of another's work or manuscript.	Yes
3.	I/we am/are aware that violation of the above is regarded as cheating and may result in cancellation of exams and exclusion from universities and colleges in Norway, see Universitets- og høgskoleloven §§4-7 og 4-8 og Forskrift om eksamen §§ 31.	Yes
4.	I/we am/are aware that all submitted theses may be checked for plagiarism.	Yes
5.	I/we am/are aware that the University of Agder will deal with all cases where there is suspicion of cheating according to the university's guidelines for dealing with cases of cheating.	Yes
6.	I/we have incorporated the rules and guidelines in the use of sources and references on the library's web pages.	Yes

Publishing Agreement

Authorization for electronic publishing of the thesis.

Author(s) have copyrights of the thesis. This means, among other things, the exclusive right to make the work available to the general public (Åndsverkloven. §2).

All theses that fulfill the criteria will be registered and published in Brage Aura and on UiA's web pages with author's approval.

Theses that are not public or are confidential will not be published.

I hereby give the University of Agder a free right to make the task available for electronic publishing:	Yes
Is the thesis confidential? (confidential agreement must be completed and signed by the Head of the Department)	No
- If yes: Can the thesis be published when the confidentiality period is over?	Yes/No
Is the task except for public disclosure? (contains confidential information. see Offl. §13/Fvl. §13)	No

Acknowledgements

I would like to express my gratitude to Zhiyu Jiang and Graeme Mackie for their guidance throughout the duration of this project. Their expertise, willingness to share their knowledge and insights, and constructive criticism were instrumental in analyzing and interpreting the results, and led to a deeper understanding of the research. I deeply appreciate the time and effort that they invested, and thank them for their mentorship.

Abstract

Among various renewable energy technologies, offshore Floating Photovoltaics (FPV) represents a new and favorable approach to the constantly diminishing amounts of fossil fuels and the need to reduce carbon emissions in the pursuit of a sustainable future. The advantages of an FPV system include the conservation of land areas and high PV efficiency because of the water cooling effect. Despite the advantages, offshore FPV technologies also face significant technical and economical challenges, and there are few robust systems that can withstand harsh offshore environmental conditions.

To address the technical challenges of a recently proposed novel FPV concept using semi-submersible floats and rope connections, this thesis created, calibrated, and studied a numerical model for a model-scale FPV array. The FPV array consists of 3 by 2 modules with cross-shaped rope connection and horizontal moorings. The time-domain numerical simulations were carried out in OrcaFlex, which accounts for the structural behaviour of the FPV array and the fluid-structure interaction under wave loads. The numerical simulation results were compared against those obtained from hydrodynamic model tests for a physical model. Ten regular waves and three irregular waves with different wave periods and heights are considered. During the numerical study, the motion of a single floating body within the array, tension in mooring lines and the ropes connecting the floating bodies are analysed in detail.

The results show that the Reponse Amplitude Operators (RAOs) of the numerical model have a percentage difference of less then 5.67% compared with those of the physical model in heave. An analysis of the tension in connecting ropes that tie the floating bodies together reveal that the diagonal ropes can experience snatch loads. A sensitivity study reveals that reducing the line stiffness can eliminate these snatch loads. Furthermore, spectral density graphs show a good comparison for irregular waves, the numerical and experimental surge and heave motion response appears to be excited at similar frequencies with similar spectral density.

The outcomes of this study contribute to improved numerical modelling and comparison against physical models and more robust design of critical structural components (e.g., rope connection) for the novel FPV system.

Contents

List of Figures

List of Tables

Acronyms

DOF Degree(s) of Freedom.

QD Quadratic Damping.

RAO Response Amplitude Operator.

DNV Det Norske Veritas.

UiA Universitet i Agder.

FPV Floating PhotoVoltaic.

FEM Finite Element Method.

ULS Ultimate Limit State.

STD Standard Deviation.

WR Regular Wave.

WIRR Irregular Wave.

RMS Root Mean Square.

JONSWAP Joint North Sea Wave Project.

UPM Technical University of Madrid.

Symbols

Φ	Potential function
ω	Wave angular frequency
λ	Wavelength
ρ	Density
T	Period
f	Frequency
H	Wave Height
H_s	Significant Wave Height
σ	Standard Deviation
ζ_a	Wave Amplitude
h	Water depth

Chapter 1

Introduction

1.1 Background

In the transition to renewable sources of energy, solar power has emerged as a promising solution to the problem of diminishing fossil fuels. However, traditional solar farms face many obstacles, such as the need to conserve land resources and loss of efficiency at high cell temperatures, among others. Of the solar based energy technologies known to us today, Floating Photovoltaics (FPV), presents a novel and efficient solution to these obstacles.

One advantage of FPV farms is that they conserve valuable land resources. Installing a solar farm on land requires a lot of space. For example, a crystalline panel farm would need roughly $16187m^2$ of land for every megawatt of power [1]. Simply moving the solar farm onto a body of water would mean less deforestation and avoiding harming local eco-systems [2], as well as make this land available for other purposes such as infrastructure and agriculture. Installing them on water might, in some cases, be even faster than on land considering that preparing land for a solar farm requires excavating and levelling, which can take a long time. The same can also be said when it comes to expansion. On land one would have to remove a variety of obstacles, out at sea however, with no buildings or forests around, expansion is much easier.

Another benefit of FPV is that the panels provide shading. This not only reduces algae growth, leading to better water quality, but also reduces evaporation. Limiting evaporation by placing an FPV system on a reservoir or lake helps especially in places where water is scarce [3]. The energy production may also improve because of the cooling effects of water [2].

Still, FPV farms face their own unique set of engineering challenges, specifically understanding and managing their interaction with water and other environmental loads such as waves, winds, and currents.

A study on the hydrodynamics of an FPV system with ten bodies arranged in a single row, [4], concluded that such a system was fairly stable and had good sea-keeping. Another paper, [5], analysed three different 3x3 FPV array models in OrcaFlex focusing on waves smaller than 1 meter, and compared the results to a reference model based on accuracy and computational time. It was found that model A, a model where hydrodynamic interaction is not considered, gave the best results. The author concluded that it was effective when it came to simulating the motion response of an FPV array.

This thesis deals with the numerical modelling, calibration and analysis of a model scale (1:60) floating PV array modelled in OrcaFlex and how it compares to a physical model, the goal of which is to understand its behaviour by analysing the motion of a single floating body withing the array and select lines in the system, when subject to regular and irregular waves.

The analysis focuses on the surge and heave motion of a single floating body in the array during regular waves of both operational and extreme conditions, as well as irregular waves that aim to replicate realistic sea conditions. The behaviour of connecting ropes and mooring lines are also scrutinized. Additionally, the results from the numerical model are compared against results for the corresponding floating body and lines of the physical model, obtained from a model-scale experimental FPV array tested in a wavemaker basin [6].

By analysing and comparing the RAOs, motion, and tension results of the numerical model against the physical model, a firm basis has been formed for understanding how the moored FPV system responds to a variety waves, which is an important step forwards in the implementation of a stable FPV system in an offshore environment.

1.2 Components of a Floating Photovolatic System

1.2.1 Photovoltaics

Photovoltaics (PV) are a steadily progressing renewable energy technology, continuing to improve in efficiency and cost-effectiveness. The purpose of PV technology is to convert solar energy into electricity. The cells on a PV panel are made from semiconducting materials. The most commonly used material is silicon, but there are others such as Indium, Germanium, and Selenide [7]. However, these are far more scarce than Silicon, and thus less commonly used. When sunlight hits the solar cells, electrons are excited and form electron-hole pairs. A current is created by capturing these free electrons. This process where sunlight is used to generate electricity is called the photovoltaic effect. In addition, there are a variety of silicon cell technologies. For instance, mono-crystalline, multi-crystalline, and amorphous cells among others. A PV system requires many components besides the PV modules to function, for example inverters, batteries to store the energy, regulators, wiring, monitoring systems, and many others [7].

1.2.2 Floating Platforms

Installing PV panels on bodies of water naturally requires floating platforms. These need to be buoyant enough to take the mass of the PV panels and at the same time be able to endure environmental loads such as waves and currents for long periods of time. A commonly used material for floating platforms in FPV systems is High-Density Polyethylene (HDPE), which is UV and corrosion resistant in addition to having high tensile strength [8]. Each floating platform will usually carry a certain amount of PV panels. Connecting many of these together forms an array or system of interconnecting floating platforms. A benefit of this type of system is that it is easily expanded.

1.2.3 Mooring Systems

The main purpose of a mooring system is to prevent the FPV array from overturning or drifting away. It consists of a number of lines connected to the floating platform on one end and anchored to an unmoving landmark or structure at the other. These lines can be made up of chains, wires, synthetic rope, or other materials [9][10][11].

The most common types of mooring systems are taut-leg and catenary moorings. The taut-leg mooring, as the name implies, connects the floating platform to the seabed using taut mooring lines. The floating platform is kept in position by tension in the lines. This type of mooring is mostly used in deep waters. In contrast, a catenary system uses far more material because part of the line has to be lying on the seabed. Here, instead of tension, most of the

work is actually done by the curved shape of the mooring lines [11][9].

Mooring systems can also be divided by how the mooring lines are distributed, namely single point and spread mooring systems. As the names imply, for a single point mooring, all the lines are gathered in one place, whereas a spread system distributes the mooring lines to different parts of the floating platform [11].

There are many factors that influence the choice of mooring system, some of which are water depth, FPV array size, and environmental conditions.

1.3 FPV Concepts

With FPV being a relatively new field, FPV farms installed on bodies of water are rare. Some examples of concepts that have been tried are given below.

One concept, described in [12], was a flexible thin film PV array. This concept used no floating platforms, by relying on the low mass of thin film PV panels to let them float. The FPV panels were held together by a neoprene mesh, which is a rubber-like material, coated to the backside of the panels. The FPV array had 3 panels on either side of a central bus which held the inverters. A prototype of this model was tested on a pond in Sudbury, Canada. Another offshore PV concept where the PV panels are installed on an elevated platform has also been attempted. An article published by PV Magazine, [13], shows a offshore platform for PV arrays where platform is elevated high above water as seen in figure 1.1.

Figure 1.1: An offshore elevated floating PV system installed at the Port of Ostend, in the North Sea coast of Belgium [13].

The concept which was the basis for the experimental model described in chapter 3, was to use lightweight, hollow floating pontoons made of HDPE, connected to each other by lightweight ropes, and held in position with multiple mooring lines anchored to the seabed[6] (Fig. 1.2).

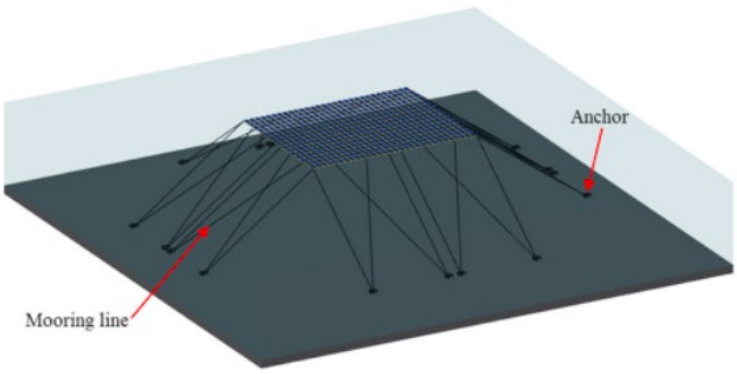

Figure 1.2: Illustration of FPV concept that served as a basis for the experimental model described in chapter 3 [6].

1.4 Motivation

Among sustainable energy technologies, offshore floating photovoltaic systems have in recent years gained a lot of attention. Implementing PV systems on bodies of water solve many of the problems that traditional land-based PV farms face. Thus, this section looks at the motivations for researching floating PV systems.

Being a new and emerging field, there has not been done much research on Floating PV farms, especially when it comes to numerical models and comparisons between numerical and physical models. Some different types of FPV concepts that have been research are described in chapter 1.3. Thus, the research done in this thesis is a vital step towards creating efficient and reliable FPV systems. In addition, research into FPV systems using different body types, materials, and water depths are still in the nascent stages.

Environmentally, it is also important that FPV concepts are researched as they represent a step towards a more sustainable future, reducing carbon emissions and avoiding the use of fossil fuels.

1.5 Objectives

As stated previously, the objective of this thesis is to develop a numerical model of an offshore floating solar photovoltaic concept, that is calibrated to match the results from a physical multi-body model. The results are then to be compared against those of the physical model. This entails the following:

- Present a numerical model that simulates realistic results.
- Analyse the behaviour of the numerical offshore FPV system model when subject to waves.
- Create a reliable, global model for dynamic motion behaviour of a floating PV array.

1.6 Research Questions

The research questions for thesis are divided into a main research question with three sub-questions. They are as follows:

- How to numerically model and evaluate the global dynamic response characteristics of a 3 by 2 Floating Photovoltaic (FPV) array?
  - How do the ropes connecting the floating bodies to each other behave when the FPV array is exposed to waves?
  - How do the numerical mooring lines compare to the mooring lines in the physical model during the different waves?
  - How does the surge and heave motion of the numerical floating body compare against the physical model?

1.7 Limitations & Assumptions

- The numerical model does not fully capture all the properties of the material used for the pontoons and lines.
- Environmental loads such as winds and currents are not considered.
- This thesis does not investigate the power performance of the FPV system, only motion and structural response.
- The thesis is limited in time by a deadline, which means efficiency is key when trying to complete the project.

1.8 Thesis Outline

The thesis is split into the following chapters:

- **Chapter 2 - Theory:** Supplies the reader with a basic understanding of the theoretical concepts applied.
- **Chapter 3 - Experimental Setup:** Presents the system used in the experimental setup, whose results the numerical model is measured against.
- **Chapter 4 - Numerical Model:** Describes the process of designing the floating photovoltaic system, from meshing of floating bodies to creation of position keeping system.
- **Chapter 5 - Results & Discussion:** Reviews and discusses various aspects of the project, from design to simulated results, including alternative solutions. The numerical results are compared against experimental ones.
- **Chapter 6 - Conclusions & Further Work:** Summarises the results and key conclusions, in addition to suggestions for further research.

Chapter 2

Theory

2.1 Linear Wave Theory

2.1.1 Regular Waves

Regular waves are an ideal type of wave characterized by their constantly repeating shape and motion. This means that their period, wavelength, amplitude, direction, and wave height, among other things, are all constant. And because of this, regular waves are simple and easy to predict, and thus useful for studying structure and wave interaction in a controlled environment, such as in a wave tank or numerical models [9, p. 5-2].

In figure 2.1, the water surface is represented by ζ. Measured from still water level, which is the water surface when subject to no waves, to wave crest is ζ_a, which stands for the wave amplitude. The wavelength and period are symbolized by λ and T respectively. H refers to the wave height and represents the vertical distance from trough to crest, trough being the lowest point on the wave, while crest is the highest point. The water depth, h, is the vertical distance from the surface of the water when it is calm, to the seabed. For a wave moving in the positive x-direction, the wave can be described as seen in equation (2.1), where the wave number, k, and the circular wave frequency, ω, can be written as $k = \frac{2\pi}{\lambda}$ and $\omega = \frac{2\pi}{T}$ [9, p.5-4].

$$\zeta = \zeta_a \cdot cos(kx - \omega t) \tag{2.1}$$

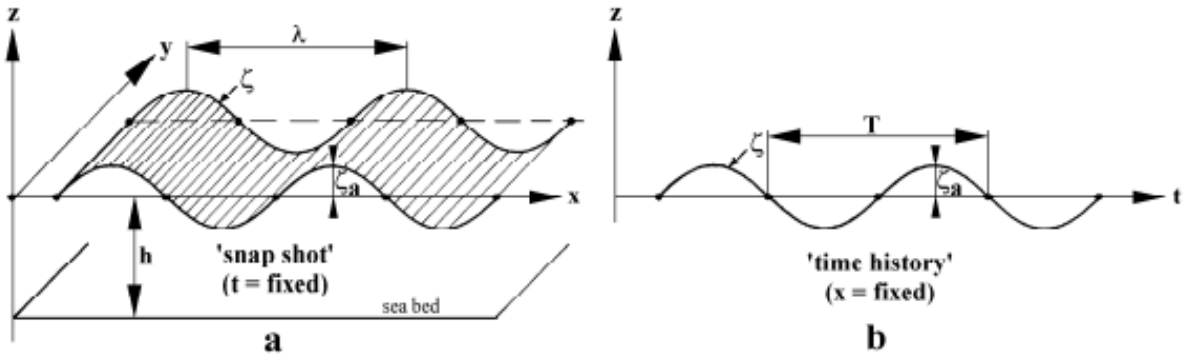

Figure 2.1: Visual representation of a regular wave [9, p.5-4].

2.1.2 Irregular Waves

Irregular waves are a more realistic representation of actual sea conditions, where waves are influenced by wind and tides among other factors. These waves are made up of different wave components, all with different periods, wavelengths, and amplitudes. An irregular wave changes continuously with time without repeating itself.

As seen in figures 2.2a and 2.2b, an irregular wave is constructed from two or more regular waves, all superimposed on one another. The result is a complex wave that is much harder to predict and analyse. And because of this complexity, one is often required to use statistical approaches to characterize their properties [9, p.5-29].

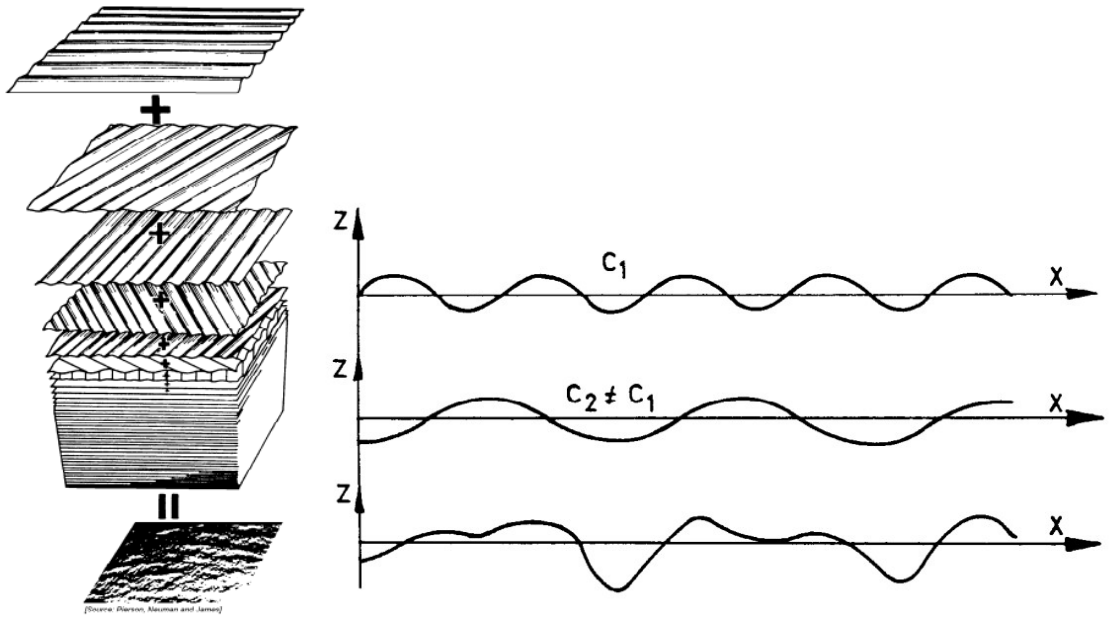

(a) (b)

Figure 2.2: Irregular waves made up of multiple super-positioned regular waves.

2.1.3 Wave Spectrum

The Pierson-Moskowitz spectrum is a model developed for unidirectional, fully developed seas with stable wind and nearly unlimited fetch, such as the North Atlantic Ocean. It describes the energy distribution of waves for a range of frequencies. The Pierson-Moskowitz spectrum is expressed mathematically as [14, p. 5][15, pp. 324-328]:

$$S(\omega) = \frac{\alpha \cdot g^2}{\omega^5} exp(-\beta(g/U\omega)^4) \tag{2.2}$$

Here $S(\omega)$ represents the spectral density, ω is the angular frequency, g is the gravitational acceleration, and α and β are constants determined through experimentation to be $\alpha \approx 8.1 \cdot 10^{-3}$ and $\beta \approx 0.74$ [15, pp. 327-328].

The Joint North Sea Wave Project (JONSWAP), is another spectrum that was developed for the North Sea but with limited fetch. It is commonly used in the design and analysis of offshore structures. It shows higher peaks than the Pierson-Moskowitz model and also a narrower bandwidth [9, p. 5-45][15, p. 331][14, pp. 6-7].

2.2 Potential Flow Theory

In hydrodynamics, potential theory is used to explain fluid motion around objects. Waves and currents affect the floating body differently. And the relationship between these environmental loads and a floating body may be understood and predicted with the use of potential flow theory. According to the theory, fluid motion can be described by a potential function.

2.2.1 Continuity Equation

The conservation of mass in an important concept in fluid dynamics, it is essential in fluid analysis and is explained using the continuity equation. The idea is that the moving fluid can only be redistributed when considering a closed system [9, p. 3-2][16, pp. 529-530].

The equation is given in (2.3), where ρ is the fluid density, t is time, and $\vec{V}$ is the fluid velocity vector [9, p. 3-3].

$$\frac{\partial \rho}{\partial t} + \nabla \cdot (\rho \vec{V}) = 0 \tag{2.3}$$

The continuity equation can be simplified further as seen in (2.4) by assuming that the flow is incompressible. If considered incompressible, the density, ρ, becomes constant, and can thus be cancelled [9, p. 3-3][15, p. 61].

$$\nabla \vec{V} = 0 \tag{2.4}$$

2.2.2 Potential Function

A potential function is a function where at every location in the flow, the velocity in any one direction is just the derivative of this potential function in that specific direction. Which is the case if it fulfills laplace's equation [9, p.3-7].

$$\nabla^2 \Phi = 0 \tag{2.5}$$

A second condition that must be fulfilled is that the potential theory solution is irrotational, for which equation (2.6), must hold true for the x, y, and z-planes [16, p. 531][15, pp. 108-110].

$$\frac{\partial v}{\partial x} - \frac{\partial u}{\partial y} = 0 \; in \; the \; (x, y) - plane. \tag{2.6}$$

Potential flow theory assumes that the fluid flow is continuous, incompressible, irrotational, and inviscid [9, p.3-7][17].

2.2.3 Diffraction Theory

The sum of the potentials from the diffraction of the undisturbed incoming wave on the fixed body (Φ_d), the undisturbed incoming wave (Φ_w), and the radiation potentials from each degree of freedom (Φ_j), according to potential theory, form the floating body potential. The mathematical expression is given in equation (2.7)[9, p.7-38].

$$\Phi = \sum_{j=1}^{6} \Phi_j + \Phi_w + \Phi_d \tag{2.7}$$

2.2.4 Elementary Flows

A uniform flow is the simplest type of flow, where the fluid moves uniformly, at a constant velocity, in one direction [18, p. 6].

In a source flow, the fluid is injected at a point, the source of the fluid, and pours outwards from that point uniformly in all directions. In contrast to this, in a sink flow, the fluid flow moves inwards towards a single point, where it is absorbed or disappears. The flow rate is positive for a source flow, and negative for a sink flow. To put it simply, a sink can be considered a negative source [18, p. 7][16, p. 533].

Another elementary flow is a vortex. Here, the flow moves circularly around a single point. For this kind of flow, it is important to exclude the origin point during integrations in the fluid, since the velocity goes to infinity at this point [18, p. 8].

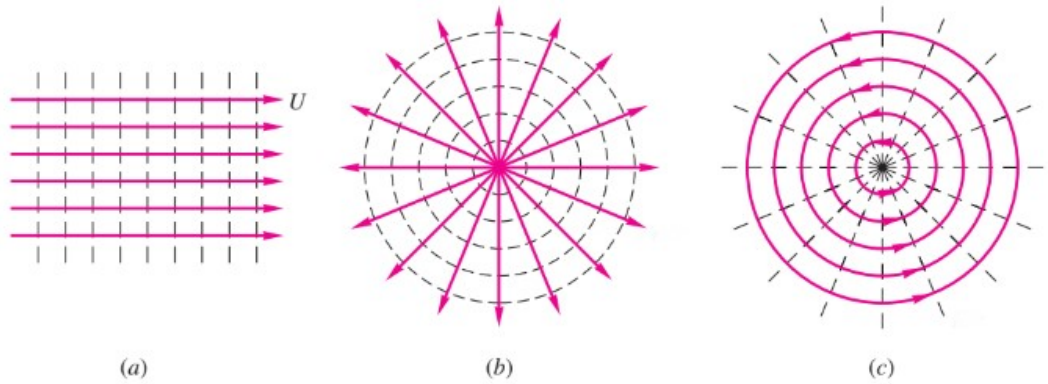

Figure 2.3: Common elementary flows used in potential theory. a) Uniform flow, b) source flow, c) vortex flow [16, p. 533].

One can also create more complicated flows by combining simpler flows. For example, one can make a doublet flow, where a source and sink are placed close to each other so that the source emits fluid that is subsequently absorbed by the sink [9, pp.3-13, 3–17].

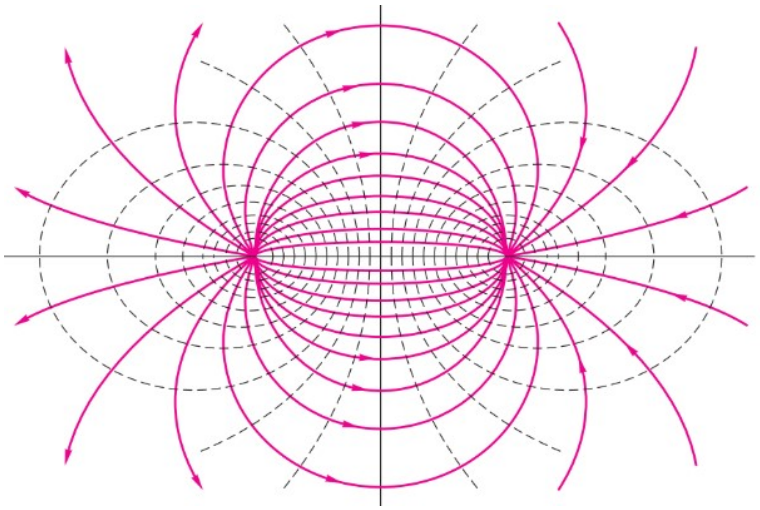

Figure 2.4: A doublet flow, created by placing a sink and source element close to one another [16, p. 534].

2.3 Dynamics of Floating Bodies

2.3.1 Equation of Motion & Cummin's Equation

The equation of motion is used in hydrodynamics to describe how a body in water moves when subject to forces such as gravity, buoyancy, and waves, among others. For a moored offshore floating PV array, like the one described in this thesis, this equation is essential if one is to model a safe and stable system. It also plays an important role when trying to optimize the energy production, since one has to understand the motion of the body to orient the FPV array in the best way possible [9].

Cummin's equation expands on the equation of motion by taking into account the memory effect by adding the convolution integral. It is derived from the linear potential flow theory and accounts for the fact that the body in its current state is affected by past wave excitation. By combining added mass and damping because of water, it gives an accurate picture of the body dynamics [9, p.6-36][19].

$$(\mathbf{M}+\mathbf{A})\ddot{x}(t)+\int_{\tau=0}^{\infty}\mathbf{B}(\tau)\dot{x}(t)(t-\tau)d\tau+\mathbf{C}x(t)=\mathbf{X}(t) \tag{2.8}$$

Cummin's equation is given in (2.8), where $\mathbf{A}$ is the added mass, $\mathbf{B}$ is the retardation function, $\mathbf{C}$ is the restoring stiffness, $\mathbf{M}$ is the mass. $\mathbf{X}$(t) represents the hydrodynamic loads on the body [9].

2.3.2 Displacement RAOs

A Response Amplitude Operator (RAO) is a dimensionless unit which describes how a body in water responds to waves at a given frequency. Or more specifically, the relationship between the incoming wave amplitude and the response amplitude of the vessel in the degree of freedom of interest [20][9, p. 6-23].

An RAO will have both a magnitude and phase, revealing the vessels movement and the time lag between excitation and response. For example, the surge RAO magnitude might tell a person how much a vessel moves back and forth when subject to a wave, while the phase tells a person the response's time in relation to the wave excitation. If the phase is zero, the structure is in sync with the wave crest. At a 180 degree phase, it is in sync with the trough.

One can get the RAO from the complex transfer function, $H(\omega)$. The equation for which is given in equation (2.9), where $S_{yy}(\omega)$ is the measured motion response spectrum and $S_{xx}(\omega)$ is the input wave spectrum [21, p. 93].

$$|H(\omega)|^2=\frac{S_{yy}(\omega)}{S_{xx}(\omega)} \tag{2.9}$$

2.4 Hydrodynamic Forces on Slender Structures

2.4.1 Added Mass

Added mass comes about as a result of a body accelerating while immersed in a fluid. When submerged, a body will displace water. And when accelerating while immersed in water, it has to move the fluid surrounding it too, which increases its inertia. The total added mass increases with every body immersed because the flow of water around one body can affect another, especially if they are close to each other [22][17].

The added mass is proportional to the acceleration of the body. The body and water particles move at the same speed. Those closer to the body, however, will accelerate differently to those further away. All the particles accelerate some as the body moves, and the added mass is the weighted total of this acceleration [15, p. 147].

2.4.2 Damping

Hydrodynamic damping is important when trying to understand the behaviour of a body in water, since it has an impact on both the movement and stability of a floating body, especially when there are waves present. Damping is a way of dissipating energy. Like a resistance that the body experiences that slowly reduces its motion until it stops completely. The damping comes from the fact that the fluid has its own density, and to move through it, the object would also have to move the fluid around it [9][15, pp. 306-308]. For example, if one were to push a log floating on a body of water, it would drift until eventually the resistance from the water dissipated enough energy for it to come to a stop.

2.5 Free Decay Test

A free decay test is usually performed in order to get the natural frequency and damping of a floating body in water. Initially the body is in equilibrium, before being displaced and subsequently released. The body will then oscillates without being affected by any outside forces save gravity and hydrodynamic forces. These oscillations will decrease over time until the body finds equilibrium again. Besides the natural period and damping, a free decay test can also provide information about the added mass of an object, which can help improve the model [9, pp. 6-15, 6–17][21, pp. 85-88].

$$\frac{\zeta}{\sqrt{1-\zeta^2}} = \frac{1}{2\pi} ln(\frac{z(t)}{z(t+T_z)}) \tag{2.10}$$

$$\zeta = \frac{1}{2\pi} ln(\frac{z(t)}{z(t+T_z)}) \tag{2.11}$$

The non-dimensional damping coefficient, ζ, is calculated as shown in equation (2.10), where $z(t)$ is value of the first peak and $z(t+T_z)$ is the peak value after one full period. The natural period, T_n, is the time between two peaks [9, pp. 6-15, 6–17]. It can also be approximated using (2.11) for k values smaller than 0.4 [6, p. 12][21, p. 87].

The linear and quadratic damping coefficients for a system can be estimated from a free decay test. For example, for a system with a single degree of freedom that accounts for quadratic damping, the equation of motion can be written as seen in Equation (2.12). Where, M is the mass and added mass, B_1 is the linear damping, B_2 is the non-linear damping, and C is the restoring stiffness [21, p. 85].

$$M\ddot{x} + B_1\dot{x} + B_2\dot{x}|\dot{x}| + Cx = 0 \tag{2.12}$$

$$\ddot{x} + B_1\dot{x} + B_2\dot{x}|\dot{x}| + Cx = 0 \tag{2.13}$$

$$B_{EQ} = B_1 + \frac{8}{3\pi}\omega x_0 B_2 \tag{2.14}$$

By dividing the equation of motion, Eq. (2.12), by M, one gets Eq. (2.13). And using the equivalent linearization technique, one can replace the quadratic term with a linear term, as seen in Eq. (2.14), where ω is the frequency and x_0 is the amplitude of the oscillations respectively. The end result is Equation (2.15)[21, pp. 85-88][23, p. 252].

$$\ddot{x} + B_{EQ}\dot{x} + Cx = 0 \tag{2.15}$$

Chapter 3

Experimental Model Test of 3x2 Array

This chapter delves into the experimental endeavor that served as the comparative baseline for the numerical model. This test was carried out in October 2021 by researchers at the Technical University of Madrid (UPM), Spain.

3.1 Test Setup

Figure 3.1 depicts the setup used for the experimental tests. The model was positioned in the middle of a 100 meter long, 3.8 meter wide, and 2.245 meter deep towing tank, and moored using a four-point above-water mooring system [6].

The mooring lines were glued to the FPV array at one end and to the towing tank at the other end using a spring connected to a aluminum profile via a HBM U9C load cell used to measure the tensile force. The load cells had an accuracy class of 0.2 and the data was collected using a measuring system called Spider 8. Each float also had a hole with a diameter of 2.5mm drilled on each of its corners, exactly 7.5mm on a 45° from the corner in order to link the floating bodies together using connecting ropes and to attach the mooring lines. Both the mooring lines and the connecting ropes used to keep the floating bodies together were made of wires with a density of $0.0005\frac{kg}{mm^3}$. The pretension in the mooring lines was set to 0.245N (model-scale). A pulley was placed under each of the aluminium profiles to create the horizontal part of the mooring system. The angle between mooring lines and the water surface was approximately 4°. The floating bodies were made of polyurethane, which absorbs some water over tim [6].

Additionally, optical tracking cameras were attached to each of the floating bodies to capture the motion of the bodies, and wave probes were used to analyse the waves, which were generated by a wave-maker located at one end of the towing tank [6].

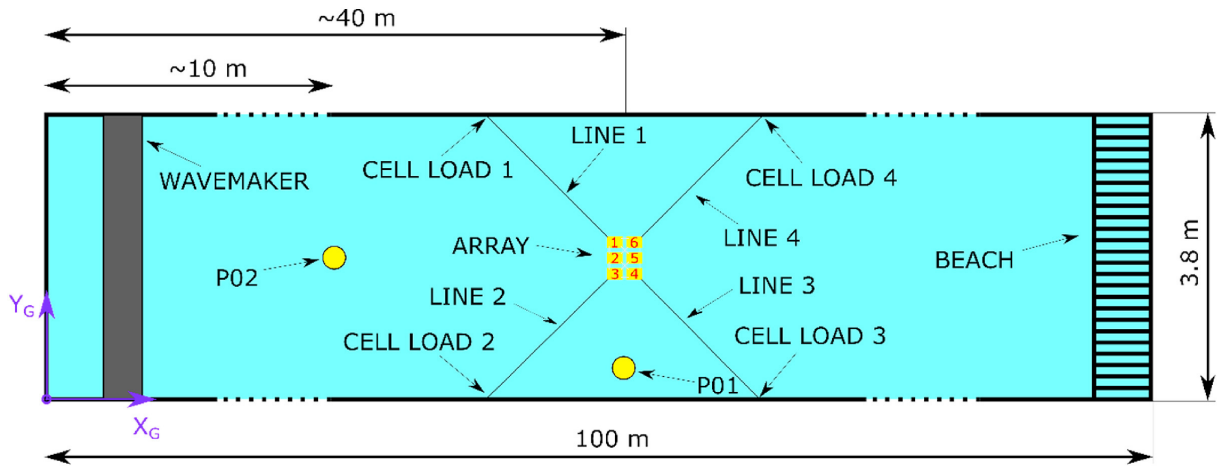

Figure 3.1: Schematic representation of experimental setup [6].

3.2 Load Cases

The load cases considered in the experimental setup are given in Tables 3.1 and 3.2. Regular waves 1 through 9 represent operational wave conditions, while regular wave 10 is an extreme wave representing survival conditions. The irregular waves are meant to mimic realistic wave conditions and thus have no fixed wave height or period.

Table 3.1: Regular wave load cases.

	Full scale		Model scale	
ID	Period [s]	Height [m]	Period [s]	Height [mm]
Regular Wave 1 (WR1)	7.8	1.9	1.00	31.67
Regular Wave 2 (WR2)	8.6	2.1	1.11	35
Regular Wave 3 (WR3)	9.3	2.7	1.20	45
Regular Wave 4 (WR4)	10.0	3.1	1.29	51.67
Regular Wave 5 (WR5)	10.6	3.4	1.37	56.67
Regular Wave 6 (WR6)	11.2	3.9	1.45	65
Regular Wave 7 (WR7)	11.8	4.5	1.52	75
Regular Wave 8 (WR8)	12.3	4.8	1.59	80
Regular Wave 9 (WR9)	12.8	5.1	1.65	85
Regular Wave 10 (WR10)	12.0	15.3	1.55	255

Table 3.2: Irregular wave load cases [6, p. 9].

ID	λ/L	T_{M*}	H*/λ	h*/λ	$H_{s(F)}$	$T_{s(F)}$
Irregular Wave 1 (WIRR1)	6.7	0.86	1.8	1.87	1.2	6.7
Irregular Wave 2 (WIRR2)	12.8	1.19	2.1	0.98	2.8	9.2
Irregular Wave 3 (WIRR3)	17.9	1.41	3.9	0.70	7.2	10.9

Table 3.2 shows the irregular wave load cases used for the experimental tests. λ is the wavelength, $H_{s(F)}$ is the full-scale significant wave height, and $T_{s(F)}$ is the full-scale significant wave period. T_{M*} is the model-scale measured period (the asterisk (*) denotes measured values). H*/λ is the relationship between the measured significant wave height and the wave period, and h*/λ is the relationship between the measured water depth and wavelength. L is the characteristic length of the floating body [6].

Chapter 4

Numerical modelling

This chapter presents the design, development, and configuration of the numerical model, from design of geometry and mesh in GeniE, hydrodynamic frequency analysis in OrcaWave, to system modelling in OrcaFlex, and its alignment with the physical experiment's conditions. For a more detailed explanation on each of the software programs, please refer to appendix B. The modelling procedure is shown in Fig. 4.1.

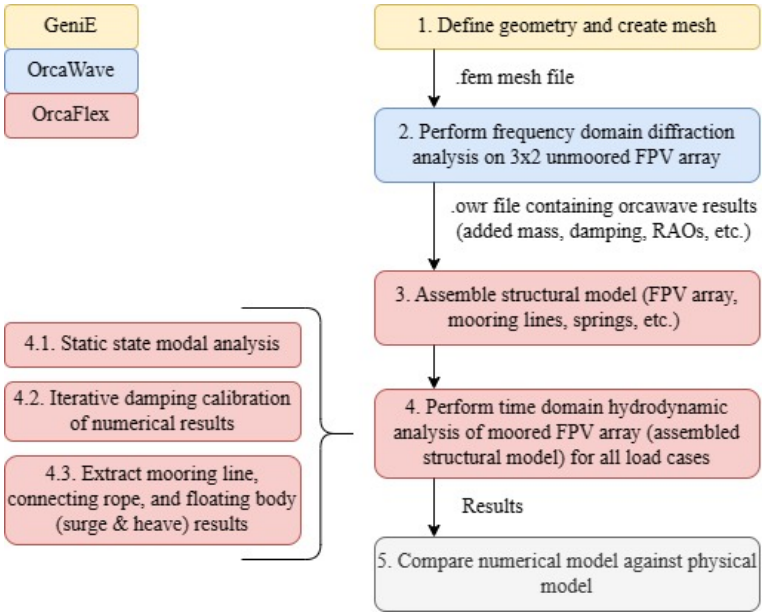

Figure 4.1: Flowchart for the modelling and calibration procedure.

Similarly to the experimental model, the numerical model is created at model-scale. The scaling factor (1:60) and how it applies to different parameters is shown in Table 4.1.

Table 4.1: Scaling factors between model- and full-scale parameters.

Parameter	Scaling factor
Acceleration	1
Time	$\alpha^{\frac{1}{2}}$
Velocity	$\alpha^{\frac{1}{2}}$
Linear dimensions	α
Area	α^2
Volume	α^3
Mass	α^3
Force	α^3
Moment	α^4

4.1 Geometry & Mesh

To begin with, the model scale body geometry is created using GeniE. The dimensions of the floating body for both full-scale and model-scale are given in Table 4.2. After the general geometry is defined, it is meshed. The result is as seen in Figs. 4.2a and 4.2b. The mesh consists of 4246 panels, with a mesh density of 2mm. The dimension of the elements is chosen to guarantee sufficient accuracy while limiting computational demands.

Table 4.2: FPV test array variables, model scale is 1:60 of full scale [6].

Variables	Full scale	Model scale
Float length	4.7m	78.3mm
Float width	2.9m	48.3mm
Float heigth	0.6m	10mm
Float density	352kg/m^3	352kg/m^3
Float draft	0.2142m	3.57mm
Array length	10.7m	178.3mm
Array width	10.4m	173.3mm
Float gap	1m	16.7mm
Marker length	-	12mm
Marker width	-	12mm
Marker height	-	34mm
Marker mass	-	0.000188kg
Water density	1000kg/m^3	1000kg/m^3

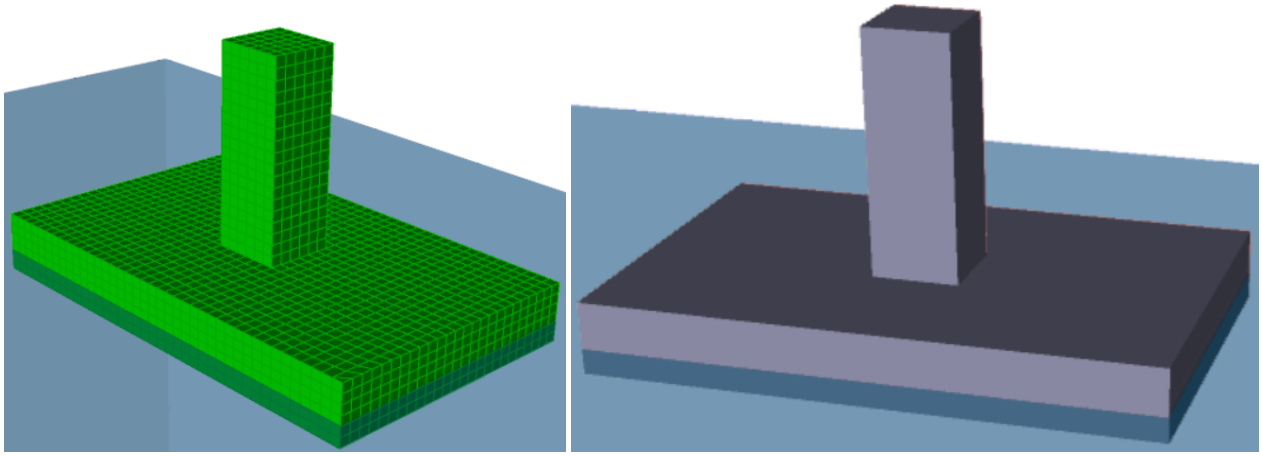

(a) (b)

Figure 4.2: Single floating body mesh as seen in Sesam GeniE [17].

4.2 Frequency Domain Numerical Modelling

The frequency domain numerical model is created in OrcaWave (refer to appendix B.2 for an explanation of the program). OrcaWave calculates loading and response for the parts of a structure that are immersed in water when there are surface waves present using potential flow theory [24].

The mesh file extracted from GeniE is imported into OrcaWave and used to create a 3x2 array. The diffraction solve type, the load RAO calculation method, and the linear solve method are set to the standard "potential formulation only", diffraction, and "direct LU" respectively.

Waves are referred to by periods, of which there are 20, ranging from 0.1 to 2 seconds, which corresponds to 0.77 to 15.49 seconds at full-scale. 9 wave headings are simulated; 0, 15, 30, 45, 60, 75, 90, 180, and 270°. The 180 and 270 degree headings were included because in a multi-body array a wave heading at 0 and 180 degrees would yield different RAOs, damping, and added mass results, among others. Take for example the array seen in Fig. 4.3a, if a person were to analyse the RAOs of body 1 within the array, a wave with a 0° (moving in the positive x-direction) would hit body 1 directly, while a wave with a 180° heading would have to travel through body 6 to reach body 1, dispersing some of the wave energy in the process, thus yielding different RAOs for the same body for different wave headings.

The moment of inertia tensor is important when trying to understand how the body resists rotational motion. OrcaWave requires that the user inputs the body's inertia into a 3x3 matrix in order to calculate the rigid body dynamics (matrix is given in appendix G.1). For this project, the mass of the floating body is 0.0135kg, and the centre of mass is defined as (0.0, 0.0, 1.736). Note that zero on the z-axis is the water surface.

The imported mesh (from GeniE) is as seen in Fig. 4.3b. OrcaWave automatically separates the body into wet and dry-body panels. The wet-body panels are the panels of the mesh that are beneath the water line. The red coordinate system seen in figure 4.3b is the local coordinate system of the floating body.

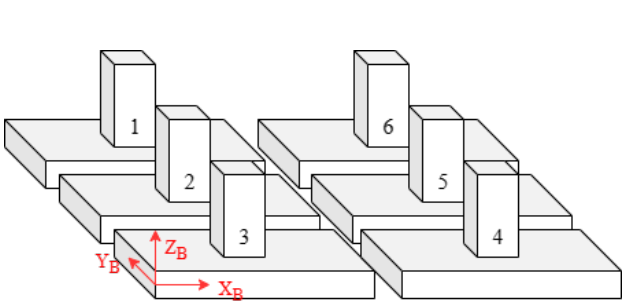

(a) FPV array configuration used in OrcaWave [17].

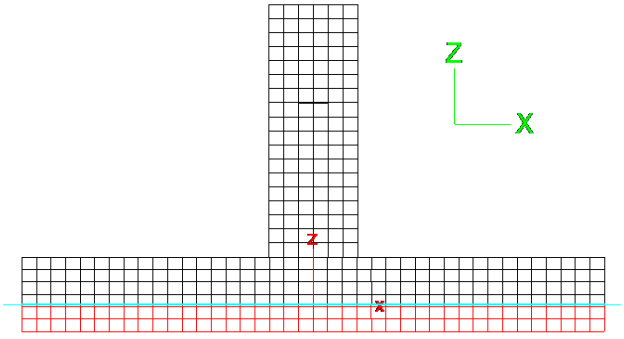

(b) OrcaWave mesh side profile of a single floating body.

Figure 4.3

Once a simulation is run, OrcaWave outputs results such as the added mass, damping, and displacement RAOs. The results are different for each floating body, capturing the effects of hydrodynamic interaction in a multi-body array.

4.3 Time Domain Numerical Modelling

This section describes how the OrcaFlex numerical model was created. This includes the objects used to assemble the structural model and their properties.

4.3.1 Floating Pontoons

When the OrcaWave file is imported into OrcaFlex, the 3x2 array of floating pontoons are automatically established as vessel objects, using the data provided by OrcaWave.

Firstly, all six degrees of freedom are included in the static analysis of the vessel. The primary motion is set to "Calculated (6 DOF)". This option allows OrcaFlex to compute the motion of the vessel in each of the six DOFs by taking into account loads from any connecting lines or other secondary objects in addition to the other effects that are included. Data for each included effect, the vessel type's stiffness, as well as the reference origin must all be specified when utilizing this option [25].

The included effects are *1st order wave loads*, *wave drift load*, *wave drift damping*, *added mass and damping*, and *other damping*. All other settings are standard (see Fig. G.4). With the exception of wave drift loads and other damping, the data for the other effects are obtained from the imported OrcaWave file. Wave drift loads are calculated by OrcaFlex using Newman's approximation, while the other damping (linear and quadratic damping coefficients applied to the floating bodies) are specified by the user for each DOF [25].

The body type data imported from OrcaWave is different for each floating pontoon, meaning each body has different displacement RAOs, added mass, damping, etc (see Figs. G.2 and G.3). The reason for which is, if one looks at Fig. 4.3a, a wave moving in the positive x-direction would hit the first row of floating bodies, before reaching the second. Therefore some of the wave energy will be dispersed before the wave reaches the second row of floats and the impact on the them would be smaller. Also, the flow of water around one body can affect the added mass and damping of another body. The results would also vary depending on the heading, since the a wave with a 0° heading compared to one with a 90° heading would produce very different motion response.

4.3.2 Mooring Lines & Connecting Ropes

The mooring lines are modelled using the line object. OrcaFlex makes the line using a number of nodes of mass joined together by segments of massless springs, called a lumped mass model. Mass, drag, and other properties of each segment of the line are lumped at the nodes, hence the name "lumped mass model" [26].

The mooring lines described in this thesis are 1932.5mm long, and divided into 19 segments. While a higher number of segments would mean higher accuracy and more realistic results, it also increases the computational time significantly.

OrcaFlex also has a line type wizard. By providing it with basic data such as the diameter of the line and the density, it can approximate the line type data [27]. The lines in the original paper, [6], had a diameter of 0.9mm and a density of 500e-9kg/mm^3, though did not say what material they were made of. The line type wizard required a material type. Among the many types available, polypropylene came closest to the density and diameter that was required. The diameter of each line in the numerical model is 0.8405mm, with a density of 500e-9kg/mm^3. Other line type data calculated by OrcaFlex are given in Figure 4.3.

Table 4.3: Approximated properties of a multiplait 8-strand polypropylene mooring line per unit length as calculated by OrcaFlex line type wizard.

Parameter	Value
Weight	4.9e-6 N/mm
Buoyancy	5.44e-6 N/mm
Submerged weight	-542e-9 N/mm
Mass	500e-9 kg/mm
Displaced mass	-555e-9 kg/mm
Submerged mass	-55.3e-9 kg/mm
Diameter to submerged weight ratio	-1.551e6$\frac{mm}{kg/mm}$
Diameter to submerged mass ratio	-15.21e6$\frac{mm}{kg/mm}$
Min breaking load	117.077N

The link object is used to model the ropes connecting the floating bodies to one another. OrcaFlex allows for two options when creating links, tethers and spring/dampers. In this FPV system, the tether is deemed suitable because the links used in the physical model were ropes which do not offer resistance like dampers and springs when compressed.

The unstretched length of the link object is so that it is 0.01mm shorter than the actual distance between the bodies, allowing OrcaFlex to recognize that the link is in tension during static analysis. The tension experienced by the links during simulation are calculated by OrcaFlex using the stiffness and unstretched length input by the user. It is calculated as seen in equation (4.1), where k is the stiffness, l_0 the unstretched length, and l is the stretched length [28].

$$T = \begin{cases} \frac{k(l-l_0)}{l_0}, & \text{for } l > l_0 \\ 0, & \text{for } l \leq l_0 \end{cases} \tag{4.1}$$

4.3.3 Springs & Winches

Winches, in OrcaFlex, provide the user with a way of connecting two or more points using a winch wire. The winch object can be either speed or tension controlled to feed or retract the wire, or simply act as a fixed length of wire[29].

Of the two types of winches available; simple and detailed winches, the simple winch was utilized. While the detailed winch allows the modelling of a more realistic winch, in the case of the numerical model described in this thesis, the winch only needed to act as a length of wire that connected the mooring line and the spring. It was used despite its ideal nature in order to prioritize reliability and ease of integration over the more complex alternative [29].

The spring is modelled using a constraint object which can introduce, fix, and apply displacements on individual degrees of freedom. It is made up of an in-frame and out-frame coordinate system. If the constraint is attached to an object, its translational and rotational motion will be connected to that object [30]. If a secondary object is fixed to the constraint, it gets attached rigidly to the out-frame, and moves with the out-frame. The out-frame will move with respect to the in-frame [30].

In the case of the FPV system described in this thesis, a fixed 3D-buoy object with virtually no mass or volume is made the primary object of the spring. This ensures that one end of the spring does not move at all. The other end of the spring is connected to the winch wire (secondary object), and restricted in all but the vertical (z) DOF. Finally, the spring is given a stiffness of 950e-6$\frac{N}{mm}$ (3.43$\frac{kN}{m}$ at full-scale).

4.3.4 Assembled Structural Model

The final design is as seen in Figs. 4.4b, 4.4a, and 4.4c. The red squares represent the floating bodies. The yellow lines are the mooring lines. The winches, which are colored orange, connect the mooring lines and the springs, through an intermediate point (green dot). The intermediate point is considered by OrcaFlex as a frictionless, ideal pulley. One end of the spring is connected to the winch wire, and the other to the fixed 3D buoy object (blue circle).

Table 4.4: OrcaFlex FPV system object parameters.

Object	Parameter	Value
Straight links	stiffness	0.183N/mm
Diagonal links	stiffness	0.130N/mm
Mooring Lines	Mass per unit length	500e-9kg/mm
Mooring Lines	Diameter	0.841mm
Springs	Tension	950e-6N/mm

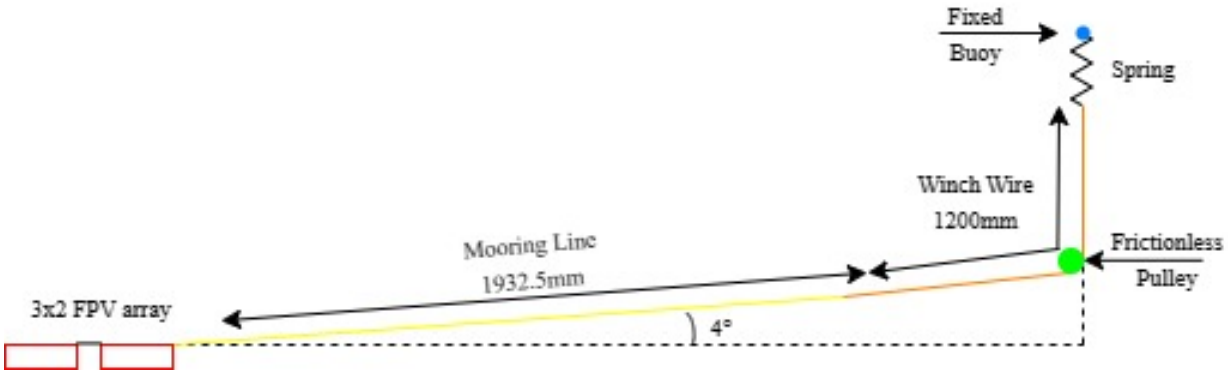

(a) FPV array side-view schematic.

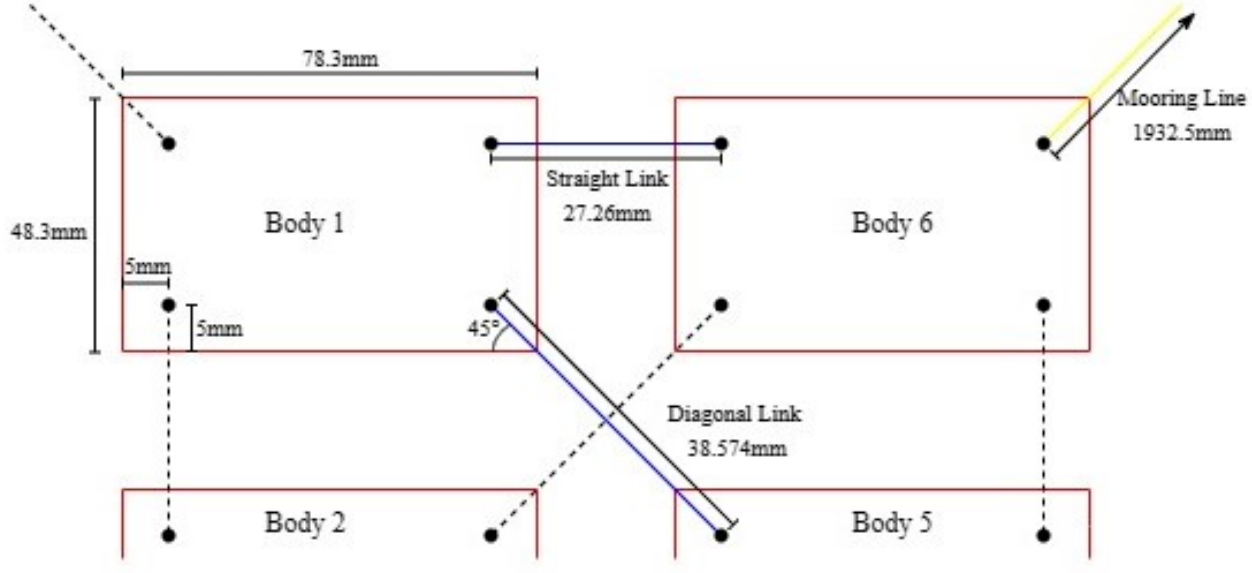

(b) FPV array overhead view schematic.

Figure 4.4: Schematics explaining the assembled structural model.

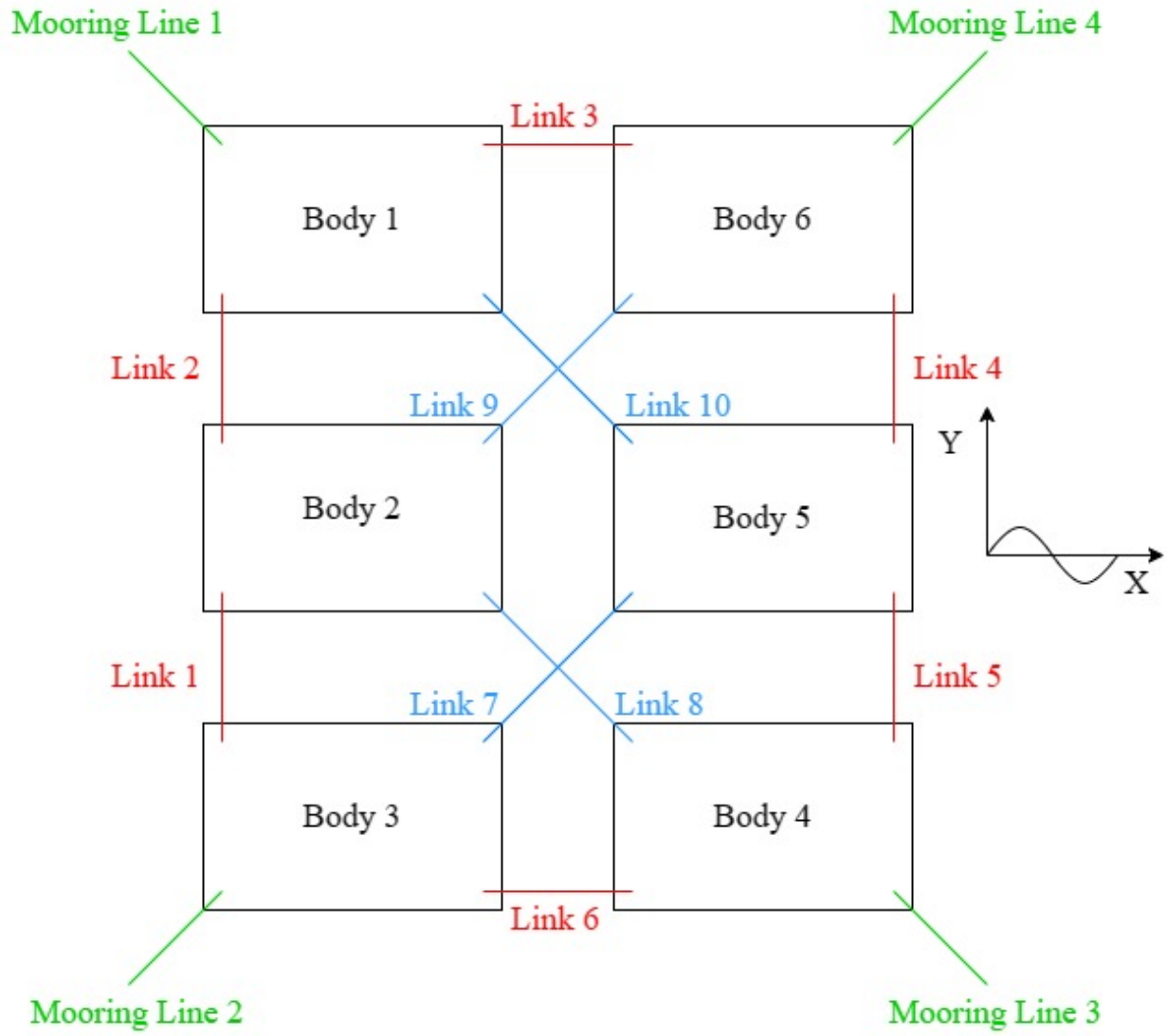

(c) 3x2 FPV array schematic.

Figure 4.4: Schematics explaining the assembled structural model.

4.3.5 General & Environmental Settings

The time step was set to 0.00833 seconds for the motion analysis and 0.02 seconds for tension analysis, same as the time steps used in the experimental results. The solution method was set to *Implicit time domain*, which is the default solution method.

To be able perform a dynamic simulation, one must first complete a static state analysis. Whole system statics were enabled for all simulations, bringing the entire system into a static equilibrium.

The water density was set to 1e-6kg/mm^3 (1000kg/m^3). The water depth used for the simulations was 2245mm, same as the depth of the wavemaker basin used in the experimental setup. The kinematic viscosity was kept at the default value which is 1.35mm^2/s. For regular waves, the wave period and height for each simulated wave correspond to the ones given in Table 3.1. For irregular waves on the other hand, the time history of waves recorded during the experimental tests were imported into OrcaFlex to get the exact same irregular waves in the physical and numerical models.

4.3.6 Damping Calibration

The method used to get the quadratic damping coefficients needed for each wave was iterative. Each load case was simulated with a quadratic damping coefficient applied to each body in the FPV array, and the resulting motion exported and compared to the results of the experimental model. This was done multiple times until a coefficient value was found that gave the best comparison with the physical model results. The calibration process is described in Fig. 4.5.

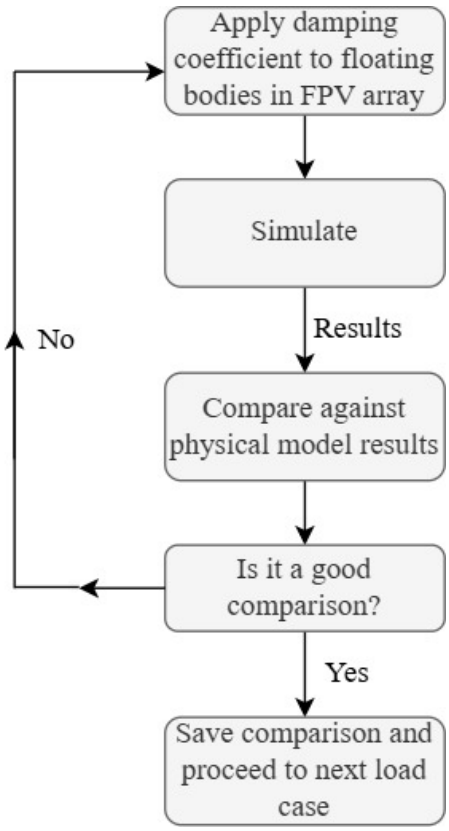

Figure 4.5: The process used during the damping calibration of the FPV system.

4.4 Limitations of Software

- OrcaFlex and OrcaWave use potential flow theory to model hydrodynamic forces, which as explained previously (see chapter 2.2), assumes that the flow is irrotational, incompressible, continuous, and also neglects viscous effects. Though, OrcaFlex does allow empirical values of viscous damping to be applied to the models.
- OrcaFlex is also limited in that it models dynamics using rigid body motion, which means it ignores structural deformations in the floats that can affect the response of the FPV array when subject to waves.
- The results will also be somewhat impacted by the what time step is used. Longer time steps result in less accurate results, but reduce the computational load.

Chapter 5

Results & Discussion

5.1 Modal Analysis of 3x2 FPV Array

The purpose of the modal analysis is to identify the natural frequencies of the FPV system. This is important because when the natural frequency of the system aligns with that of the waves, it can cause excessive motion that can be damaging to the FPV system.

OrcaFlex has a modal analysis feature that calculates the undamped natural modes of the entire system, and also animates them so that one can see the oscillations [31][32]. This allows the user to understand how the FPV system behaves during specific frequencies.

Each mode has its own frequency and shape, numbered from one and up in order of increasing frequency. The shape of each mode depicts the oscillations about the static mean position when that mode is excited [31][32]. In the case of the FPV system described in this thesis, OrcaFlex calculated 268 modes. The first ten are given in Table 5.1. The natural periods range from 0.222 to 1.271 seconds. It is observed that the natural periods of the surge and sway modes are rather close to the wave periods of two regular waves; WR3 and WR4 (refer to Table 3.1).

Table 5.1: Static state modal analysis.

Mode	Description	Period	Frequency
Mode 1	Collective sway of the array	1.271s	0.787Hz
Mode 2	Collective surge of the array	1.262s	0.792Hz
Mode 3	Collective yaw of the array	0.411s	2.434Hz
Mode 4	Half array moving inwards	0.273	3.669Hz
Mode 5	Mooring line vertical translation	0.225	4.445Hz
Mode 6	Mooring line vertical translation, 1 and 4 out of phase with 2 and 3	0.225	4.446Hz
Mode 7	Mooring line vertical translation, 1 and 2 out of phase with 3 and 4	0.225	4.447Hz
Mode 8	Mooring line vertical translation, 1 and 3 out of phase with 2 and 4	0.225	4.448Hz
Mode 9	Mooring line horizontal translation, 1 and 4 out of phase with 2 and 3	0.223	4.491Hz
Mode 10	Mooring line horizontal translation	0.222	4.497Hz

Modes 1, 2, and 7, are shown in Figures 5.1, 5.2, and 5.3 respectively. To be clear, the grey arrays represent the offset position of the FPV system when oscillating, while the red array shows the static mean position of the FPV system.

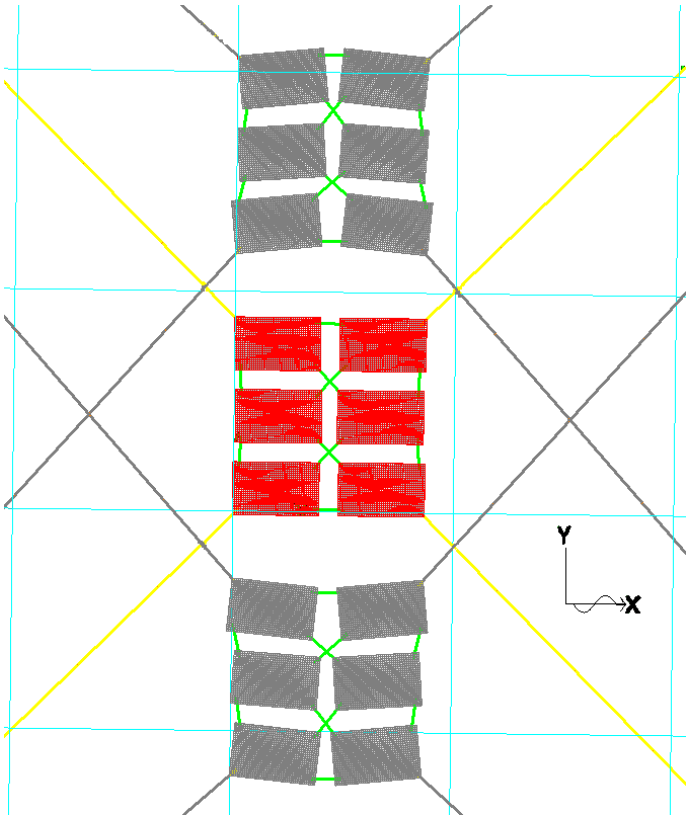

Figure 5.1: Mode 1 (sway) from modal analysis, obtained from OrcaFlex (see Table 5.1).

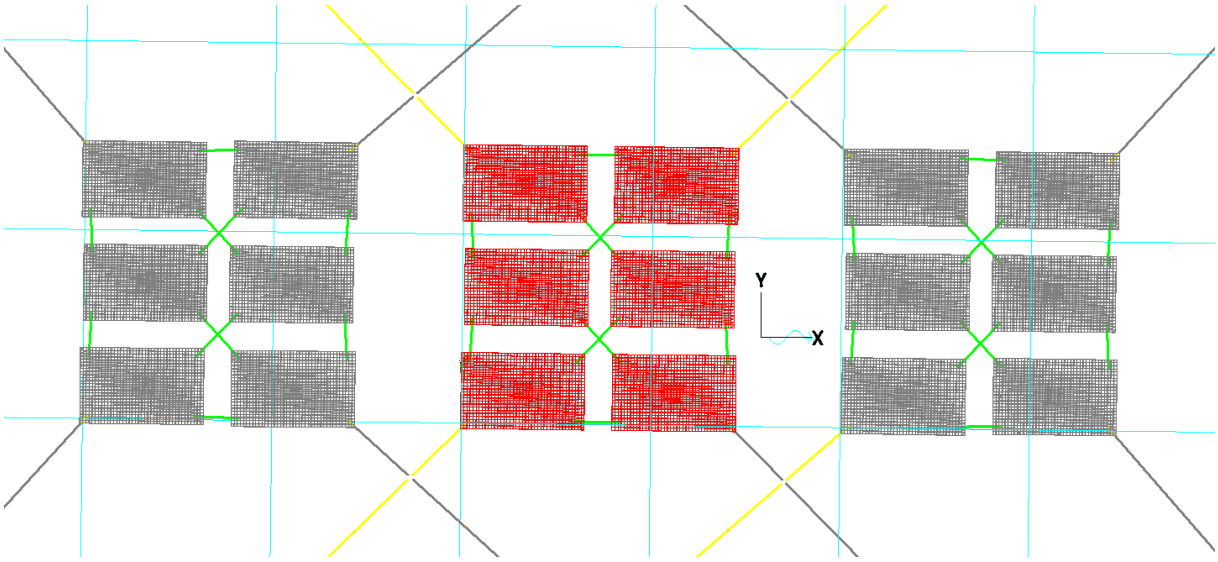

Figure 5.2: Mode 2 (surge) from modal analysis, obtained from OrcaFlex (see Table 5.1).

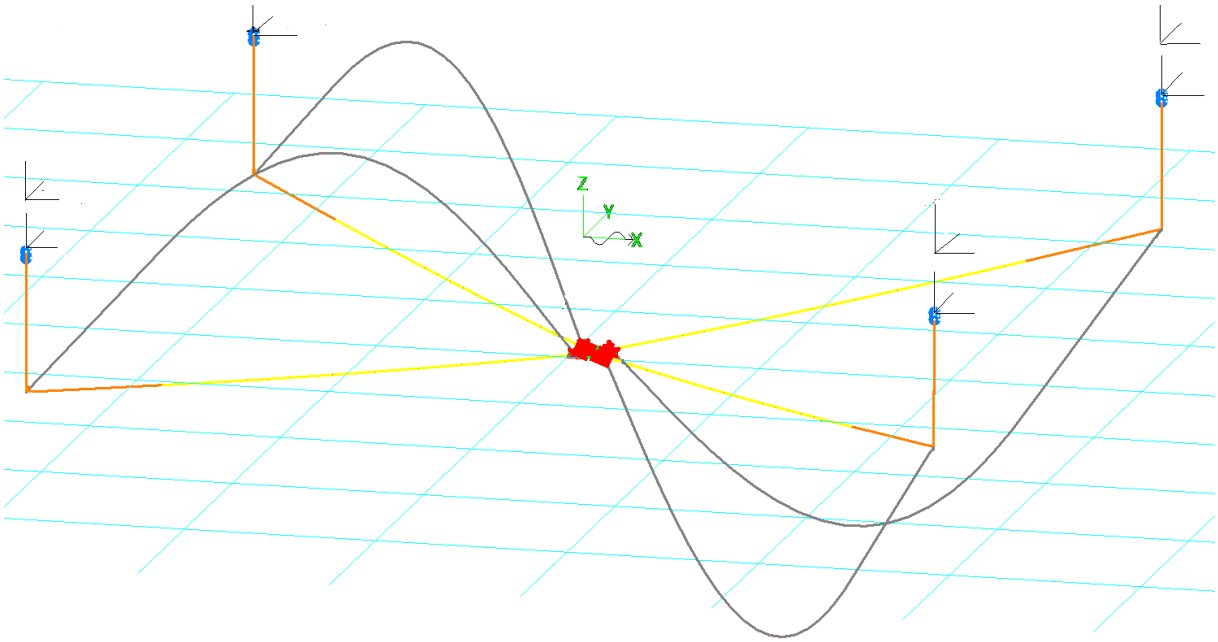

Figure 5.3: Mode 7 from modal analysis, obtained from OrcaFlex (see Table 5.1).

5.2 Damping Calibration of Numerical Results

5.2.1 Free Decay Test

Below are results from the free decay tests for both numerical and experimental tests, where k is the non-dimensional damping coefficient, and T_n is the natural period. The non-dimensional damping coefficient is calculated as shown in equation (2.11), and the natural period, T_n, is the time between two successive peaks.

The purpose of the free decay experiments was to gauge how the single float and the entire mooring system responded in calm water when subject to displacement.

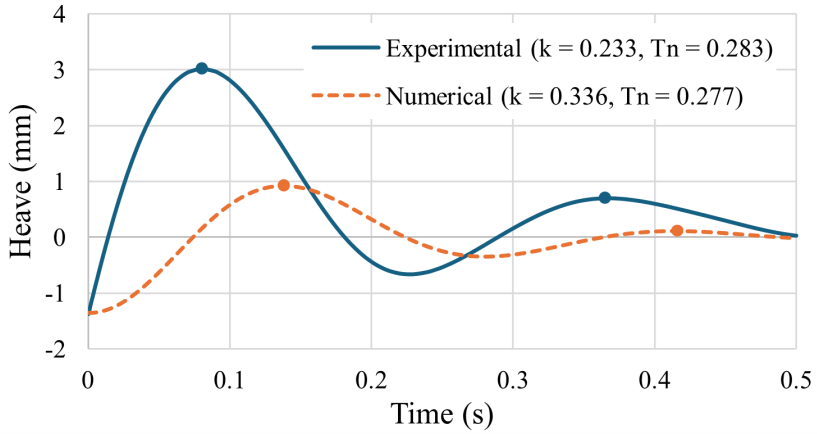

Figure 5.4: Model scale heave free decay test results for a single floating body, conducted in calm water.

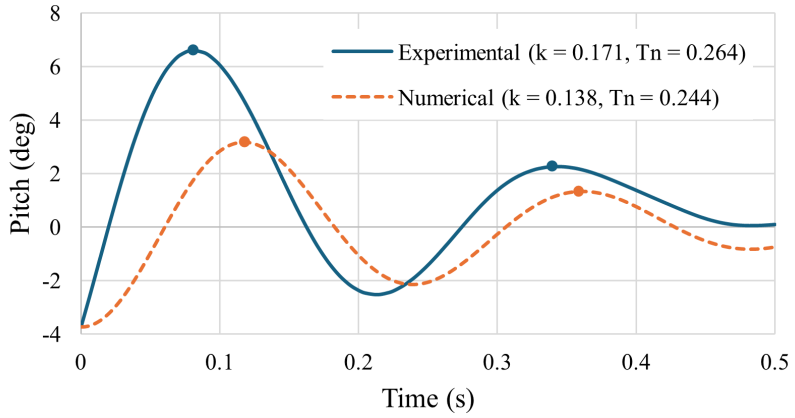

Figure 5.5: Model scale pitch free decay test results for a single floating body, conducted in calm water.

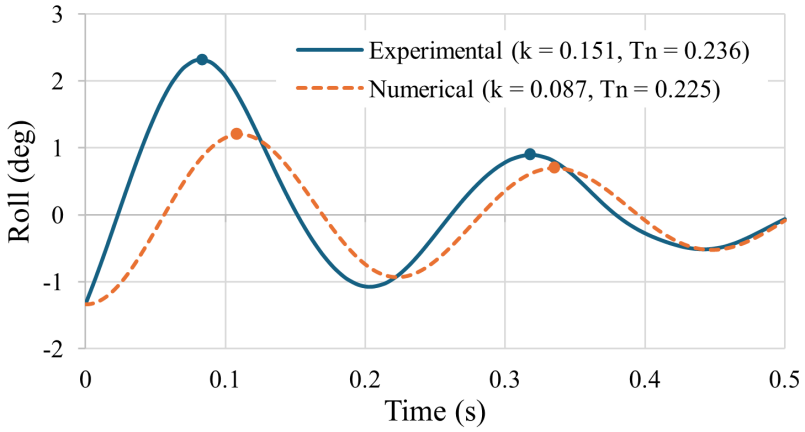

Figure 5.6: Model scale roll free decay test results for a single floating body, conducted in calm water.

Figures 5.4, 5.5, and 5.6, display the results of the free-decay tests carried out for a single float in the heave, pitch, and roll degrees of freedom. These tests were performed without mooring. The outcome shows that the natural period is nearly identical for both models in all three DOFs. The damping is slightly higher for the experimental model during pitch and roll, 3.3% and 6.4% respectively, and 10.3% higher for the numerical in heave.

A higher natural period suggests that the floating body oscillates slightly slower, which can be beneficial or a liability depending on sea conditions in that area. On one hand, taking longer time to oscillate means that the movements of the body are smoother. On the other hand, if the area in which the FPV system is stationed has waves with a similar natural period, this could lead to resonance. Resonance occurs when the natural period of the body aligns with that of the waves. This is something one tries to avoid during practical application because the increased amplitude of oscillations from resonance could damage the system.

The damping tells a person how quickly the floating body returns to rest after being disturbed. As mentioned previously, the numerical results show less damping than the experimental ones in roll and pitch, but more in heave. With no mooring lines or connecting ropes affecting the test, the differences in damping are most likely a byproduct of differences in structural design and real versus numerical fluid conditions. For one, the physical model absorbed water over time. It had a dry density of $313 kg/m^3$ and wet density of $352 kg/m^3$. This is a 12.5% increase in density over time, which can significantly affect the behaviour of the body, and is difficult to recreate in a numerical model. For simplicity, the numerical model was designed using the wet density. Also, OrcaFlex assumes the fluid to be irrotational, inviscid, continuous, and incompressible, which leads to deviations between numerical and experimental results.

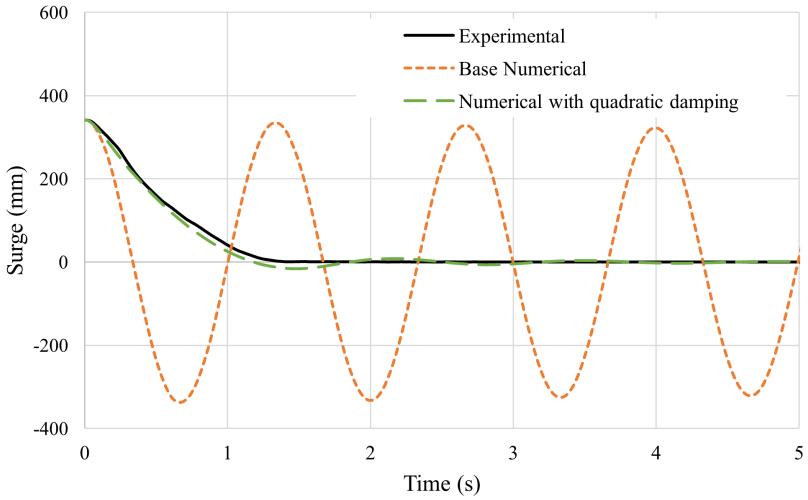

Figure 5.7: Model scale surge free decay test results for moored FPV system, conducted in calm water. Numerical simulation calibrated with 5e-7$\frac{N}{(mm/s)^2}$ quadratic damping coefficient in surge DOF.

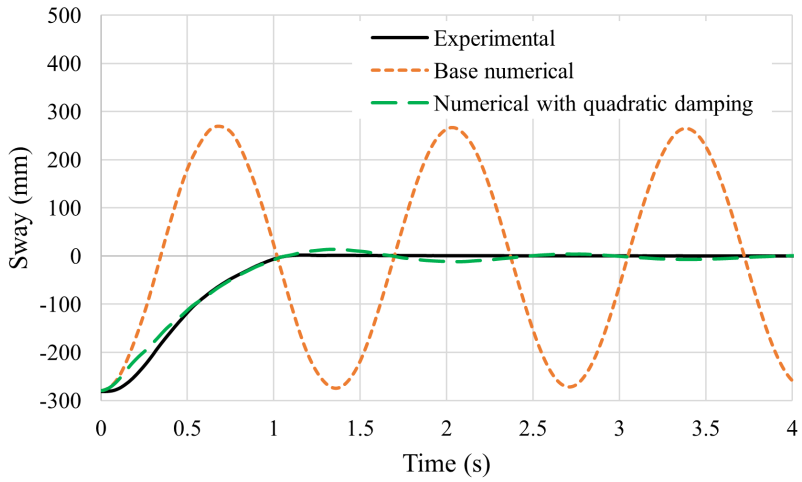

Figure 5.8: Model scale sway free decay test results for moored FPV system, conducted in calm water. Numerical simulation calibrated with 5e-7$\frac{N}{(mm/s)^2}$ quadratic damping coefficient in sway DOF.

Figs. 5.7 and 5.8 show the free decay test results for the entire mooring system in the surge and sway DOFs. The array was displaced 300mm for each test and the results calibrated to match those of the experimental tests. The numerical lines seen in the free decay test figures were achieved by applying a Quadratic Damping (QD) coefficient of 500e-9 N (mm/s)2 to each floating body in the array. Without the QD, the numerical result kept oscillating nearly indefinitely. The reason for this could be because OrcaFlex does not account for all the different types of damping that affect a real system. The OrcaFlex user manual stated that it accounted wave radiation damping and wave drift damping, but not viscous roll damping [33]. Viscous damping being the damping that comes from the friction between the water and the floating body. This is most likely the case for viscous surge and sway damping too.

5.2.2 Regular waves

The wave results are calibrated to match the experimental results as closely as possible by applying quadratic damping coefficients in the relevant degrees of freedom. The applied damping coefficients are given in Table 5.2.

Table 5.2: Quadratic damping coefficients applied to regular and irregular waves in the surge DOF.

ID	Damping $[\frac{N}{(mm/s)^2}]$
WR1	2.5e-6
WR2	4.5e-6
WR3	4.5e-6
WR4	4.5e-6
WR5	5e-6
WR6	5e-6
WR7	6e-6
WR8	5e-6
WR9	5e-6
WR10	7e-8
WIRR1	5e-6
WIRR2	2.75e-6
WIRR3	5e-7

It is clear that the required damping is similar for most load cases. The exception is regular wave 10, the extreme wave, and irregular wave 3, which is the Ultimate Limit State (ULS) wave. The anomalies are discussed later on in the thesis.

5.3 Regular Wave Cases

5.3.1 Surge Motion of Body 1

Comparisons of the numerical and experimental surge motion of body 1 when the FPV array is exposed to regular waves 3, 7, and 10, are given in Figs. 5.9, 5.10, and 5.11 respectively (the surge motion comparisons for the other regular waves can be found in appendix C). On the x-axis is the model-scale time measured in seconds, while the y-axis represents the model-scale surge motion of the body in millimeters. The results show that the floating body's surge motion is steady for each wave. This means that the mooring system reduces the influence of the waves on floating body in surge, making sure that the array holds its position even under extreme conditions, as in the case of regular wave 10. The array moves with the wave instead of absorbing all its energy.

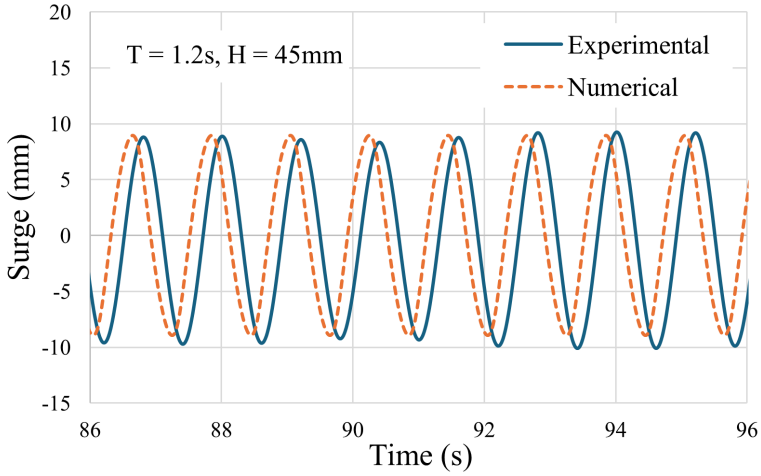

Figure 5.9: Model scale surge displacement results of body 1 when subject to regular wave 3.

For regular wave 3, the mean for the experimental model is -0.42mm, meanwhile the numerical one is 0.03. The amplitude for the numerical model if measured from mean to max is 8.91mm, whereas the experimental amplitude is 9.67mm. So, the numerical model estimates less motion for body 1 in response to WR3 than the experimental model. The reason for this could be the simplifications made by OrcaFlex. There is also the fact that a real wave, even generated in a wave maker basin to be ideal, is not 100% perfect, unlike the wave made in OrcaFlex, which is ideal with a constant, unchanging height and period. The two waves are also slightly out of phase, by approximately 0.1 degrees. These differences between numerical and experimental models become more pronounced as the wave height and period increases, as seen in Figs. 5.10, 5.11, and 5.13.

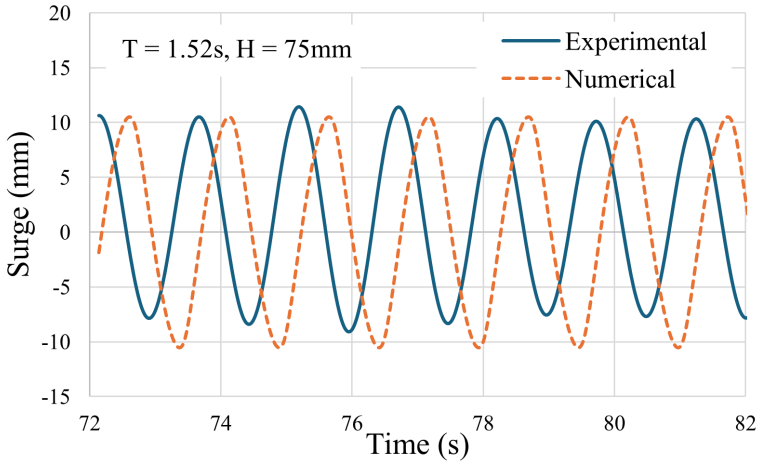

Figure 5.10: Model scale surge displacement results of body 1 when subject to regular wave 7.

Figure 5.11 shows the numerical versus experimental comparison for regular wave 10. The differences here are extreme. The mean for the physical model is approximately 51mm, while the numerical mean is 19mm. And while the maximum surge motion aligns closely, the difference in minimum is very large.

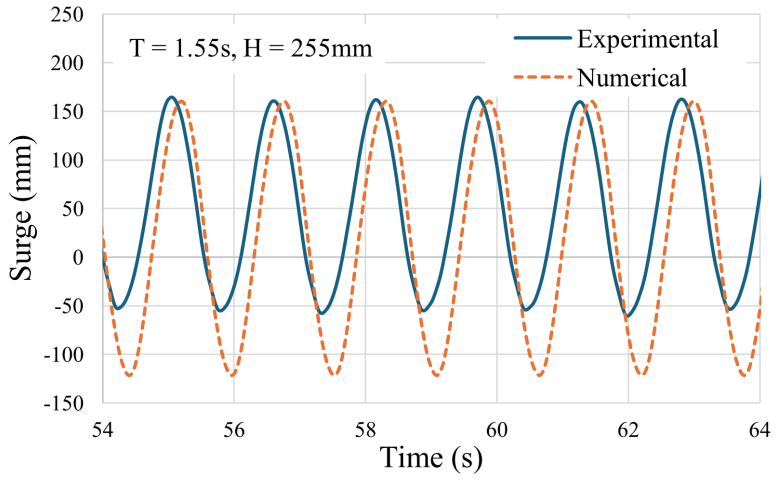

Figure 5.11: Model scale surge displacement results of body 1 when subject to regular wave 10.

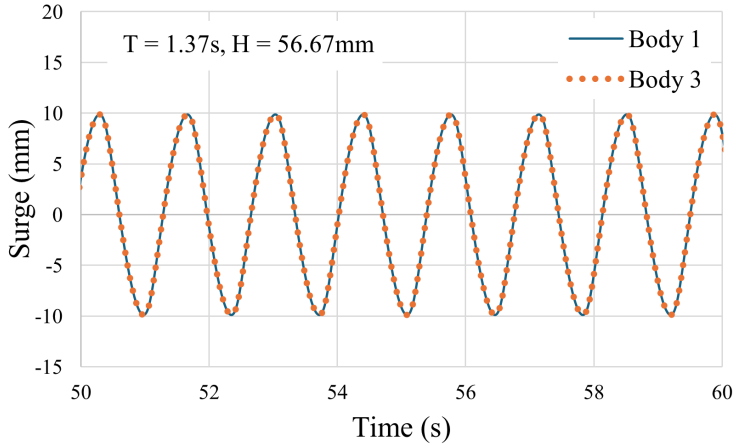

Figure 5.12: Model scale numerical surge displacement results comparison of body 1 against body 3, when subject to regular wave 5.

There is no difference in surge motion for bodies 1 and 3 during simulation for the numerical model. This holds for all waves.

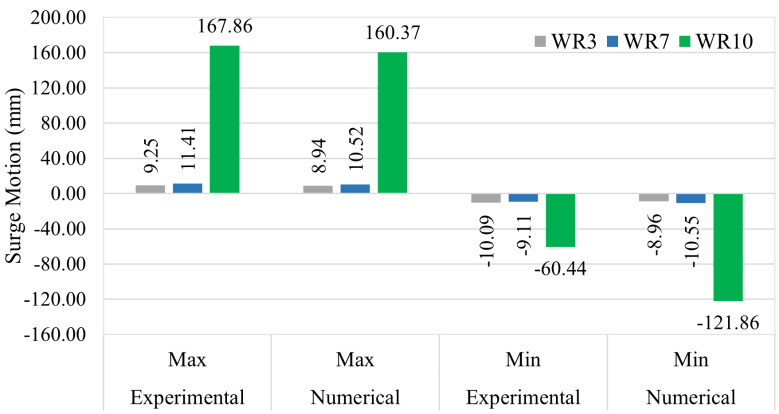

(a) Maximum, minimum, and amplitude.

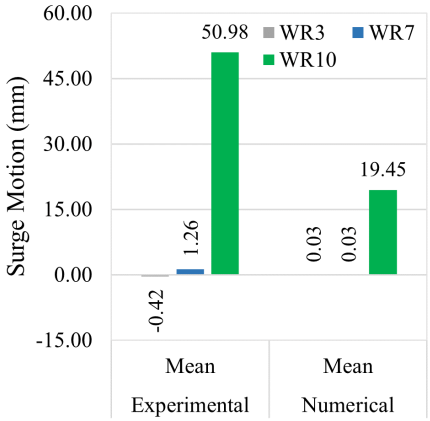

(b) Mean position of body 1.

Figure 5.13: Model scale surge motion statistics for body 1 during regular waves 3, 7, and 10.

Figure 5.13 shows the surge maximum, mean, and minimum. The maximum and minimum values tell us the furthest the body moves in the positive and negative surge directions respectively. Note that a surge motion of zero would mean that the floating body remains in its original position. The numerical model underestimates the surge maximum in each of the cases, the largest error being in WR7, where the difference is roughly 8.5% (0.89mm). The differences in minimum surge between numerical and experimental models are small for regular waves 3 and 7. But, for WR10 the simulated minimum is -121.86mm, while the physical minimum is only -60.44mm.

The reason for this may be that the numerical model underestimates the restoring forces from the mooring lines. Another possibility is a calibration error; either the stiffness or the damping of the body not being precise enough. The fault could even be with the mooring lines. Higher stiffness or damping in the mooring lines might produce better results.

It was also shown earlier in Table 3.1 that while most regular wave were calibrated with quadratic damping coefficient around 5e-6$\frac{N}{(mm/s)^2}$, WR10 was calibrated with 7e-8$\frac{N}{(mm/s)^2}$. The damping required for WR10 is significantly smaller than for the other regular waves. It is likely that the hydrodynamic damping is just naturally smaller for WR10 than for the other waves, and that quadratic damping is less significant for larger, steeper waves like this one.

5.3.2 Heave Motion of Body 1

Figures 5.14, 5.15, 5.16 depict the numerical and experimental model-scale heave response of floating body 1 when the FPV array is subjected to waves 3, 7, and 10. The heading is 0° for all waves, meaning all waves move in the positive x-direction. The heave motion results for the other regular waves can be found in appendix D.

The phase difference is clearly larger in heave for waves 3 and 10, but peak-to-peak the motion is a closer match. However, that is expected of an array with a shallow draft. The mooring system is not supposed to limit the array's heave motion. So in that regard, the mooring system appears to work as it should.

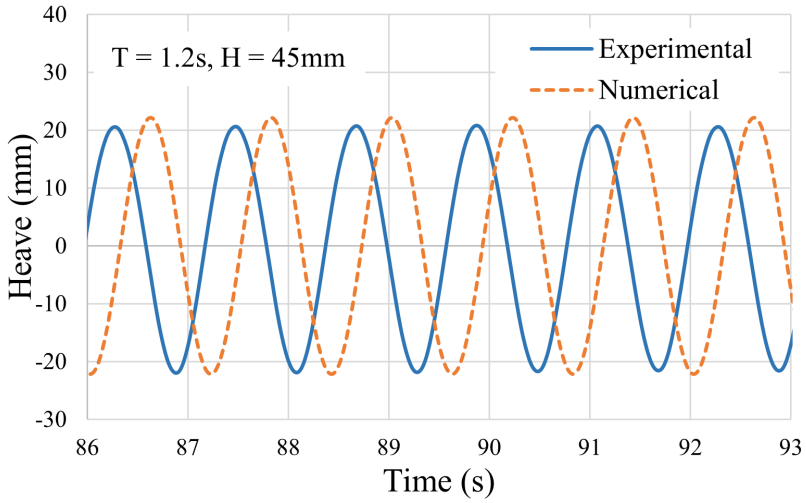

Figure 5.14: Model scale heave displacement results of body 1 when subject to regular wave 3.

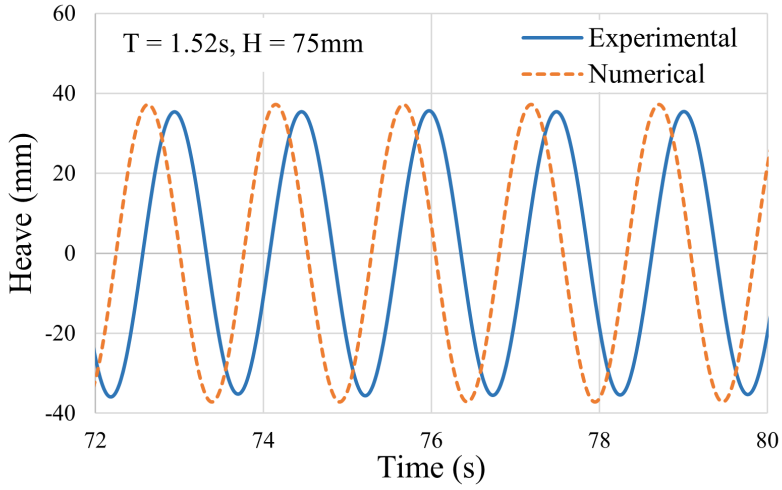

Figure 5.15: Model scale heave displacement results of body 1 when subject to regular wave 7.

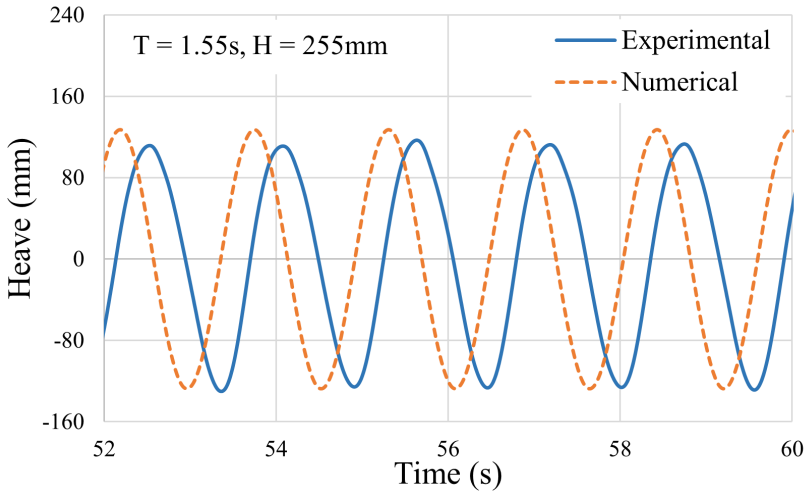

Figure 5.16: Model scale heave displacement results of body 1 when subject to regular wave 10.

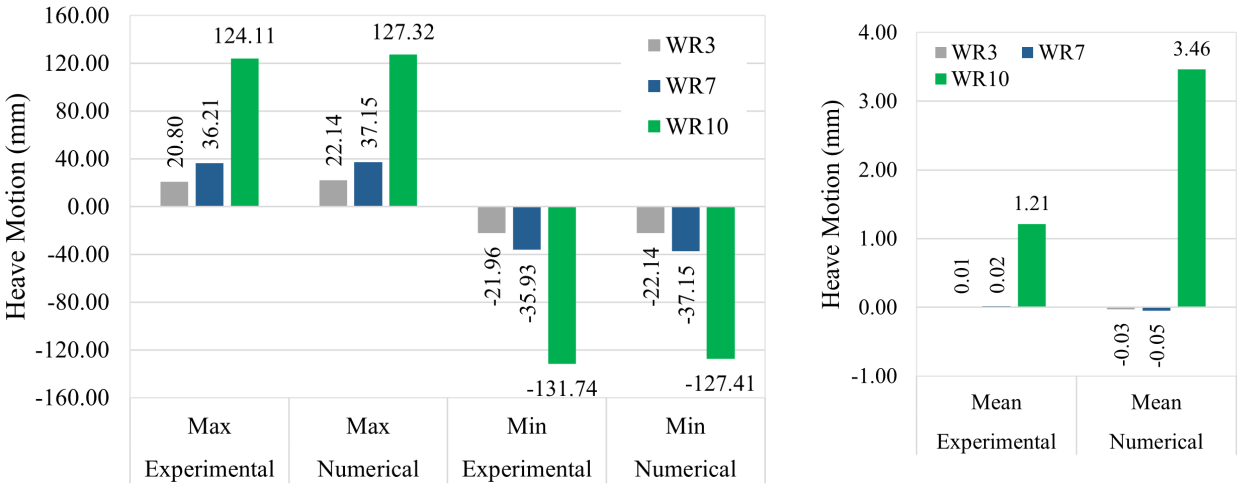

(a) Maximum, minimum, and amplitude.

(b) Mean position of the body.

Figure 5.17: Model scale heave motion statistics for regular waves 3, 7, and 10.

From figure 5.17 one can see that the difference between numerical and experimental waves are not too large. For WR3, the numerical maximum heave is 1.34mm, or 6.44%, larger than the experimental one. This corresponds to approximately 8.2cm at full scale. For WR7, this discrepancy is significantly reduced, here the numerical model overestimates by 0.94 mm or 2.59%. For WR10, the extreme wave, the difference in maximum heave 3.21mm, so the numerical model overestimates the max heave by 2.59%.

So the trend shows that the numerical model is more accurate for longer and higher waves, than for smaller, shorter waves. The numerical model overestimates the maximum heave in each case. The difference in mean position is insignificant for regular waves 3 and 7.

5.3.3 Response Amplitude Operators

Figure 5.18 shows that the surge RAO decreases almost linearly as the wave period and height increase, with the notable exception of regular wave 10, which is the survival condition wave. The RAO increases drastically for regular wave 10. This is likely caused by the steepness of the this particular wave. The steepness, H/λ, is the wave height divided by the wavelength.

Compared to the surge RAOs, the heave RAOs are more consistent, all of them have a magnitude ranging from 0.9 to 1.1. This means that the floating body follows the wave in heave almost perfectly. This agrees with the observations made in 5.3.1 and 5.3.2.

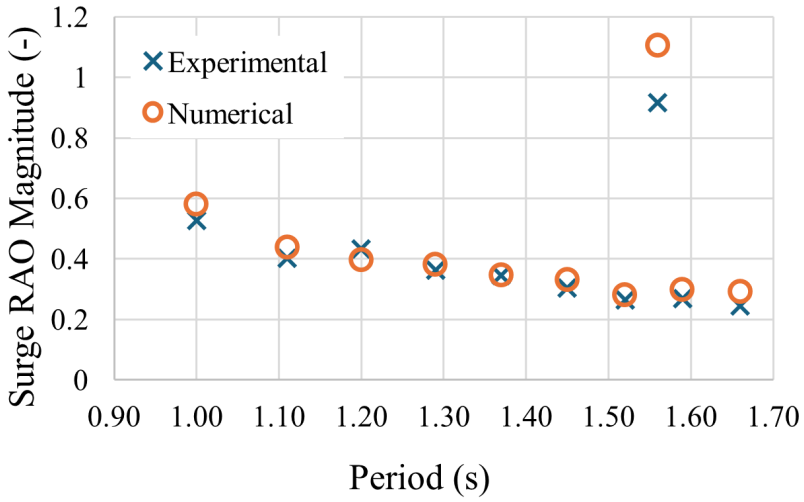

Figure 5.18: Model scale surge RAOs for regular waves.

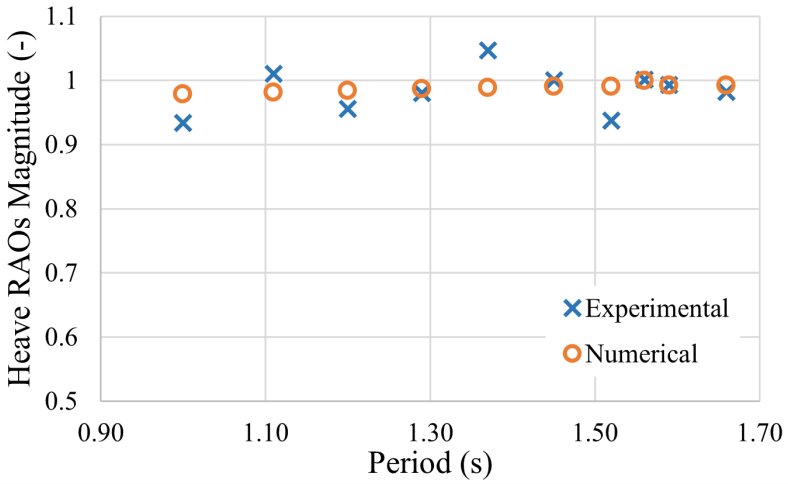

Figure 5.19: Model scale heave RAOs for regular waves.

The surge RAOs of the numerical model deviate from those of physical model by 8.35% and 6.03% for waves 3 and 7 respectively. The worst comparison is observed in regular wave 10, where the difference is 20.77%, while the best is regular wave 5 with a difference of only 0.57%.

The highest difference when comparing the heave RAOs of the ten waves from the numerical model against those of the physical model, is 5.67% in the case of regular wave 7. For WR3 the difference is 3.01%, and for WR10 it is an almost negligible 0.27%. The best comparison is observed in regular wave 8, where the difference is 0.14%.

5.3.4 Mooring Tension

Figures 5.20, 5.21, and 5.22, display a time series analysis of force exerted on mooring lines 1 and 3 for both numerical and experimental models during regular waves 3, 7 and 10. The lines have periodic shifts that point to the wave-like nature of the tension in these lines.

The tension in the experimental lines appear to jump up and down between the maximum and minimum in a pulse like manner. This is because the tools used to measure the tension in the lines had limited precision. The actual time history is continuous.

We see that the tension is higher in line 1 than 3 for the experimental model. For the numerical one, the peak-to-peak tension is higher in line 3 than line 1. Likely because of the waves forcing the array downstream, moving the array in the direction of line 3 so that tension in line 3 becomes smaller than in line 1. The tension in the lines also increase with the size of the wave. This is natural since a larger wave has more energy and thus moves the array more, thereby increasing the strain on the mooring lines.

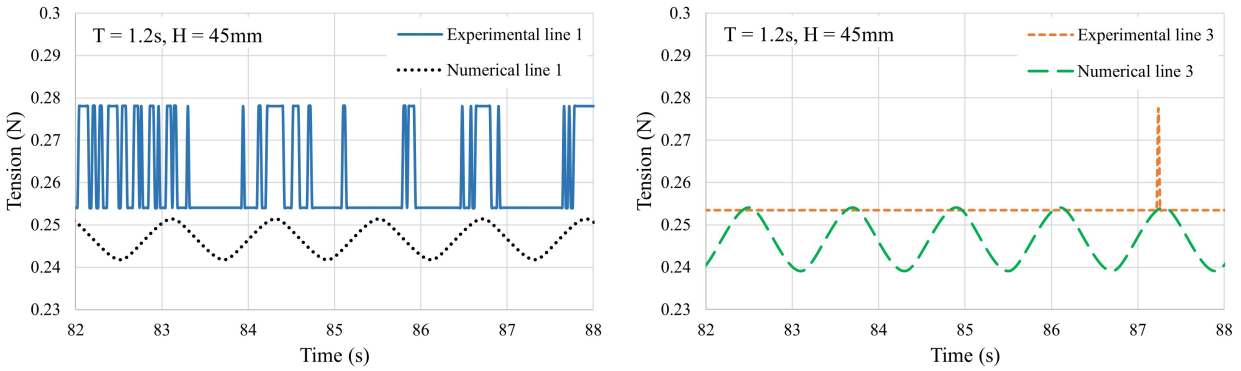

(a) Tension force in numerical and experimental line 1.

(b) Tension force in numerical and experimental line 3.

Figure 5.20: Model scale tension in mooring lines 1 (upwind) and 3 (downwind) during regular wave 3.

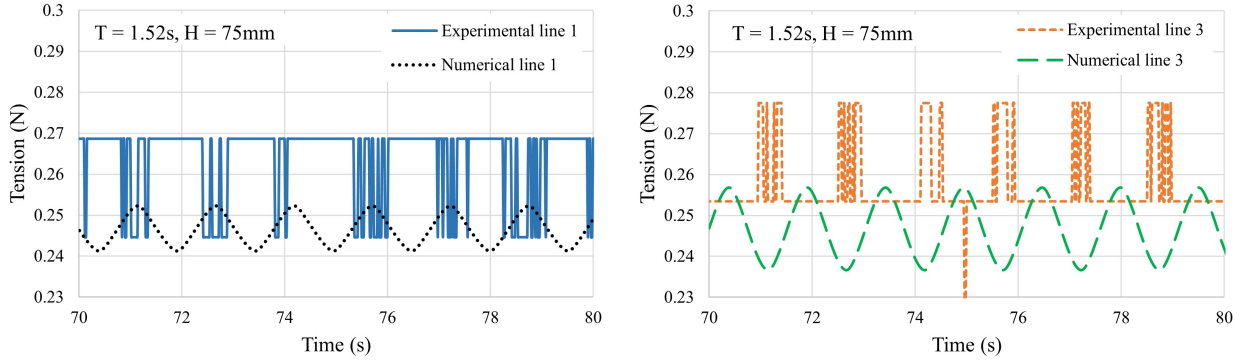

(a) Tension force in numerical and experimental line 1.

(b) Tension force in numerical and experimental line 3.

Figure 5.21: Model scale tension in mooring lines 1 (upwind) and 3 (downwind) during regular wave 7.

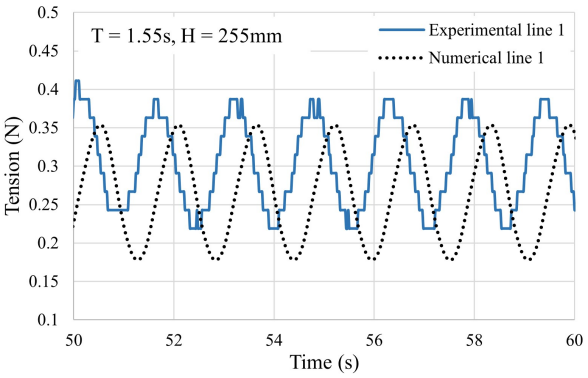

(a) Tension force in numerical and experimental line 1.

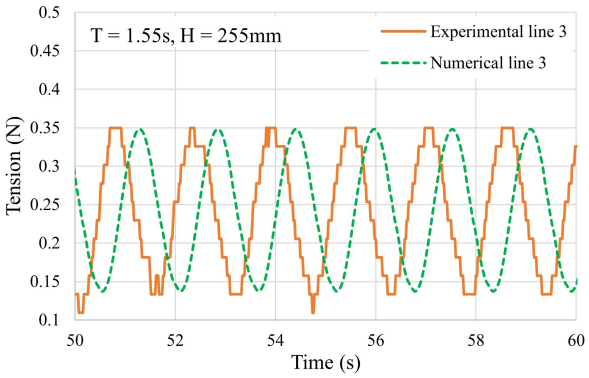

(b) Tension force in numerical and experimental line 3.

Figure 5.22: Model scale tension in mooring lines 1 (upwind) and 3 (downwind) during regular wave 10.

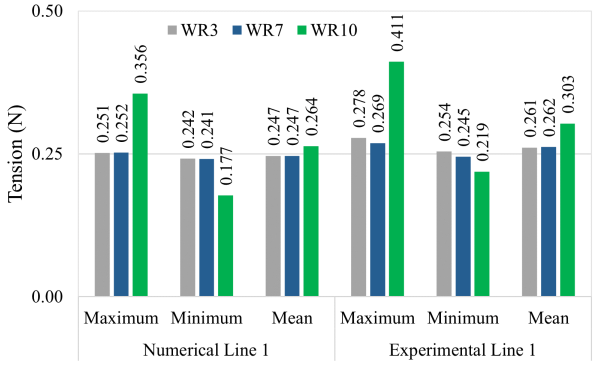

(a) Statistics for mooring line 1 during regular waves.

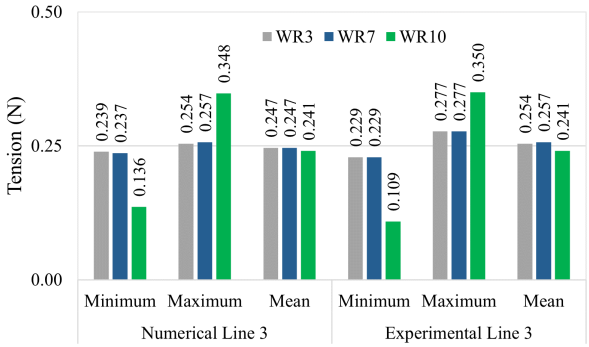

(b) Statistics for mooring line 3 during regular waves.

Figure 5.23: Model scale statistics for experimental and numerical mooring lines during regular waves 3, 7, and 10.

Tension statistics for mooring lines are given in figures 5.23a and 5.23b. For mooring line 1, the contrast in mean tension for the numerical and physical models is 0.015N and 0.0014N for regular waves 3 and 7 respectively. The numerical model underestimates the tension for mooring line 1 for not only mean tension, but maximum and minimum tension as well. In the case of mooring line 3, the numerical model underestimates the mean tension by 3.9% for WR3 and 2.8% for WR7. So the numerical model does a better job of predicting the tension in line 3. However, given the square, pulse-like form of the lines showing the experimental results during waves 3 and 7, it is difficult to make an accurate comparison.

A better comparison can be made for wave 10, seen in Fig. 5.22, where the experimental line is almost sinusoidal in shape. The mean tension in line 1 is overestimated by 12.9% by the numerical model, whereas for line 3 the mean tension is identical. The maximum tension in line 3 is also nearly identical, though the minimum is 0.027N higher for the numerical model. For line 1, the numerical model underestimates both the maximum and minimum tension.

5.3.5 Connecting Rope Tension

The connecting ropes between each of the floating bodies are also analysed. The ropes of interest are link 2, 3, and 10, which are shown in Figure 4.4c.

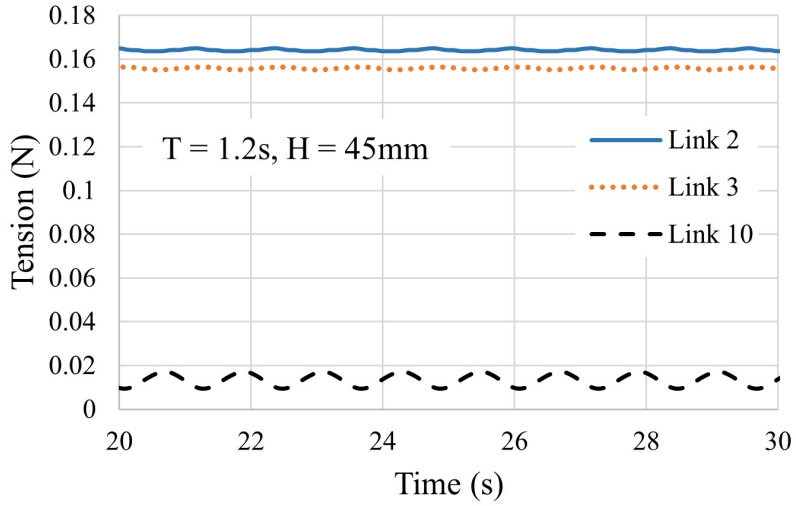

Figure 5.24: Model scale tension in links 2, 3, and 10, during regular wave 3.

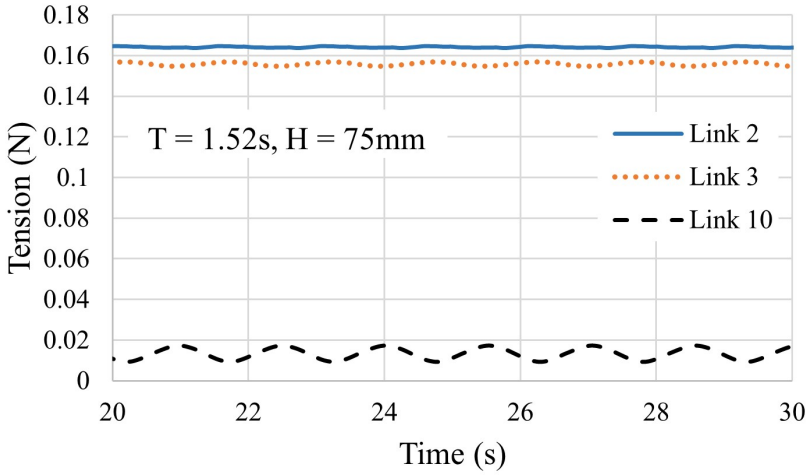

Figure 5.25: Model scale tension in links 2, 3, and 10, during regular wave 7.

In figure 5.24 we see the tension in the connecting ropes for regular wave 3. The plot shows a periodic fluctuation in force for all links, indicating that the two bodies connected by each link move closer together and then apart in a regular pattern corresponding to the wave period. The tension in links 2 and 3, the two straight ropes, are nearly identical, while the diagonal rope, link 10, experiences much less tension. The amplitude of the oscillations is consistent, the largest variation is in link 10, with a peak-to-peak value of approximately 0.008N.

For regular wave 10, 5.26, the results are quite different. For one, the bodies experience more tension. As wave energy increases with wave steepness, the bodies experience more force and thus the tension in the links are also increased. For regular wave 10, the peak-to-peak difference is highest in link 2, at approximately 0.107N.

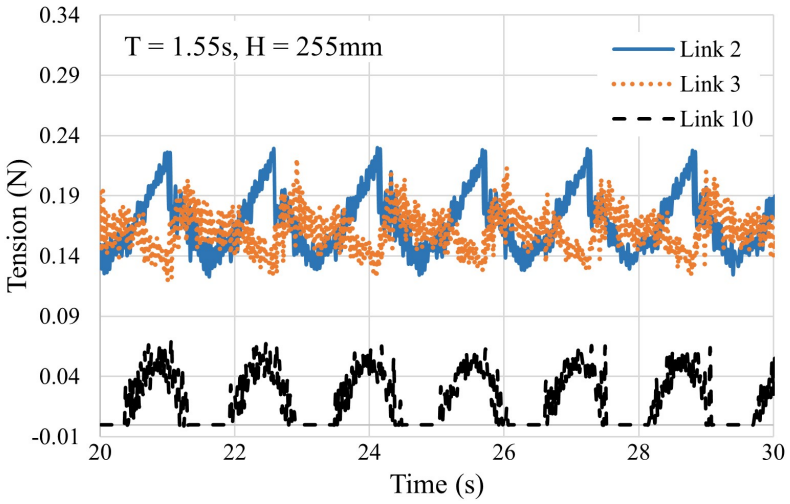

Figure 5.26: Model scale tension in links 2, 3, and 10, during regular wave 10.

It is also observed that link 10, during regular wave 10, experiences snap loads, which occurs when a line suddenly goes from being slack to taut, experiencing a quick spike of tension. Based on the information in figure 5.26, one can see that the straight links connecting the floating bodies in the FPV system are constantly under tension. The diagonal link on the other hand, keeps snatching periodically. Ideally, one would try to avoid any snatching in lines as, over time, the stress wears down the lines down and can potentially lead to the line breaking. One way to remedy this problem would be to introduce more damping to the lines, or use elastic lines or increase the pre-tension to reduce the effects. However, designing a realistic mooring system that can generate sufficient horizontal loads to pre-tension the connecting ropes is a separate challenge.

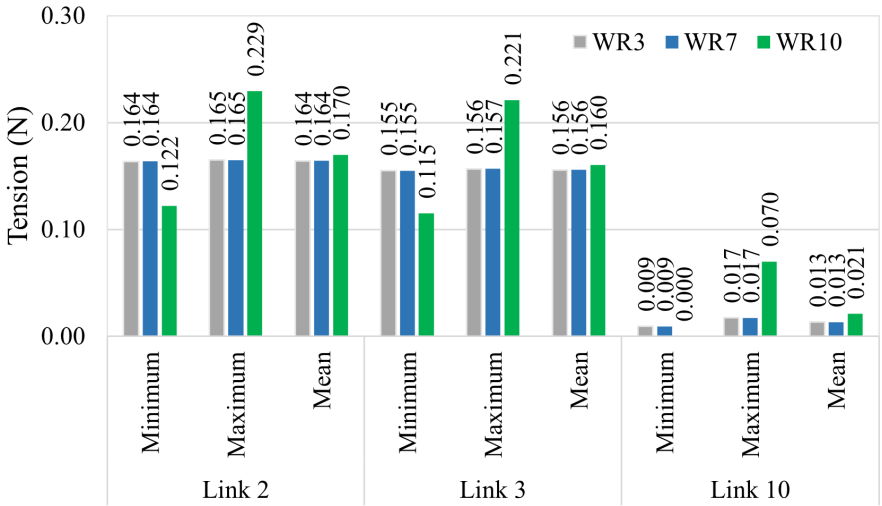

Figure 5.27: Maximum, minimum, and mean tension for connecting ropes at model scale.

The tension in links 2 and 3 shown in figure 5.27, is steady, nearly constant. The data suggests that the mooring system of the FPV array, including the links themselves, effectively absorb and dampen the movements of the floating bodies. The tension in the connecting ropes is not affected overly much by the change in period and wave height either, as evidenced by the fact that tension remains the same between regular waves 3 and 7.

5.4 Irregular Wave Cases

5.4.1 Motion Spectrum

Figure 5.28 shows the numerical and experimental surge and heave motion response spectra of body 1 for irregular wave 1. The surge and heave motion for both numerical and experimental spectra appear to be most prominent around 1.1Hz. The shapes of the spectrum's are quite similar as well. From the smoothed graphs, one can see that the heave motion is nearly identical up until 1.1Hz, after which the numerical model underestimates the heave motion slightly. The spectral density before and after the peak is very similar for the smoothed surge graphs, but the numerical peaks is significantly taller than the experimental one.

For irregular wave 2, Figure 5.29, the largest surge peaks are at approximately 0.8Hz for the numerical spectrum and closer to 1Hz for the experimental spectrum. In heave, the peaks for both models appear at 0.8Hz, but with the numerical model showing a peak more than twice as high as the tallest experimental peak. From the smoothed graphs one can tell that the surge spectra are very similar, but that the experimental is slightly higher in heave.

For irregular wave 3 (Figure 5.30), in surge there are multiple equally tall peaks in the case of the numerical spectrum, excited by frequencies between 0.6 and 0.8Hz, but the experimental surge spectrum has one very tall peak excited at approximately 0.7Hz. The smoothed graphs for WIRR3 are very similar for both the experimental and numerical spectrum's in both degrees of freedom.

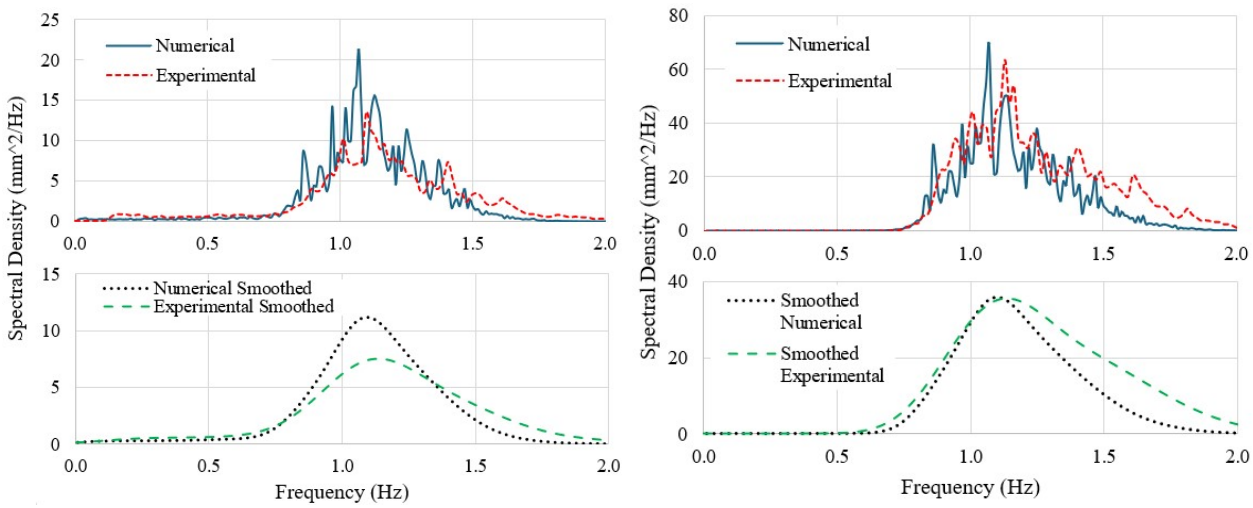

(a) Surge. (b) Heave.

Figure 5.28: Model scale spectral density plots for body 1, irregular wave 1. Smoothed using Parzen window. Experimental results obtained from Ref. [6].

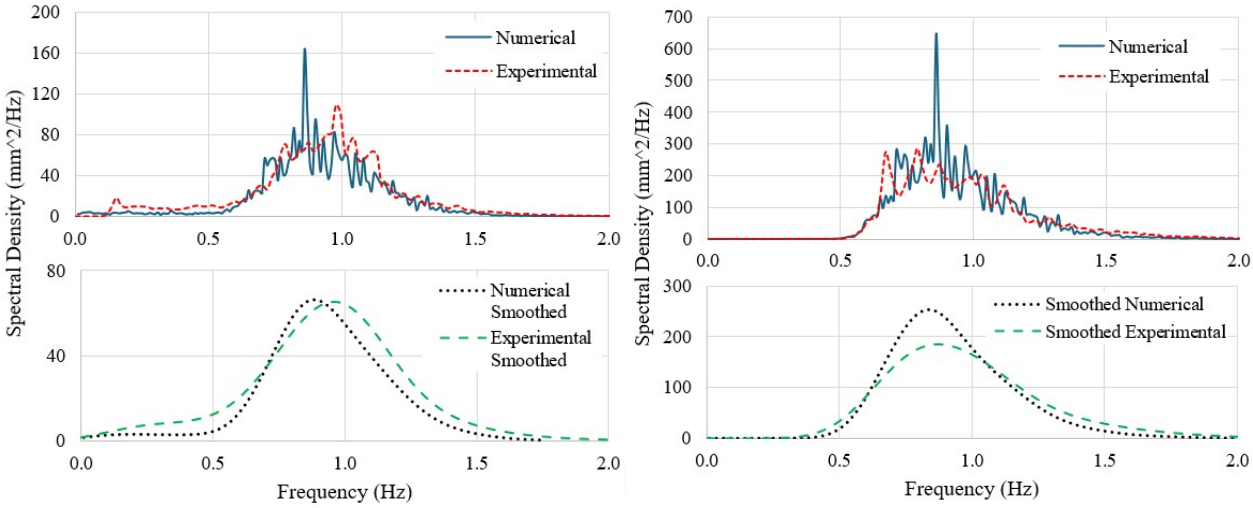

(a) Surge. (b) Heave.

Figure 5.29: Model scale spectral density plots for body 1 during irregular wave 2. Smoothed using Parzen window. Experimental results obtained from Ref. [6].

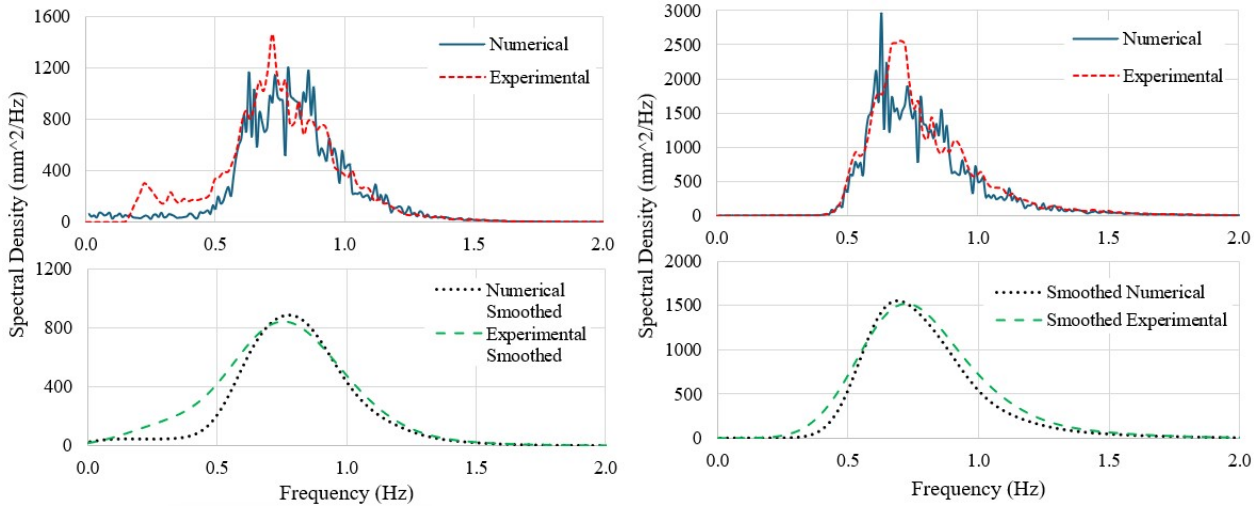

(a) Surge. (b) Heave.

Figure 5.30: Model scale spectral density plots for body 1, irregular wave 3. Smoothed using Parzen window. Experimental results obtained from Ref. [6].

5.4.2 Surge Motion of Body 1

Figures 5.31, 5.32, and 5.33, show the numerical and experimental surge motion results of body 1 during the irregular waves. While at first glance the two curves are noticeably different, there are statistical similarities in the behaviour, as seen in figure 5.35. Figure 5.34 shows that for the numerical model, the motion of bodies 1 and 3 when compared against one another is identical. Both bodies move the same distance from their respective original positions.

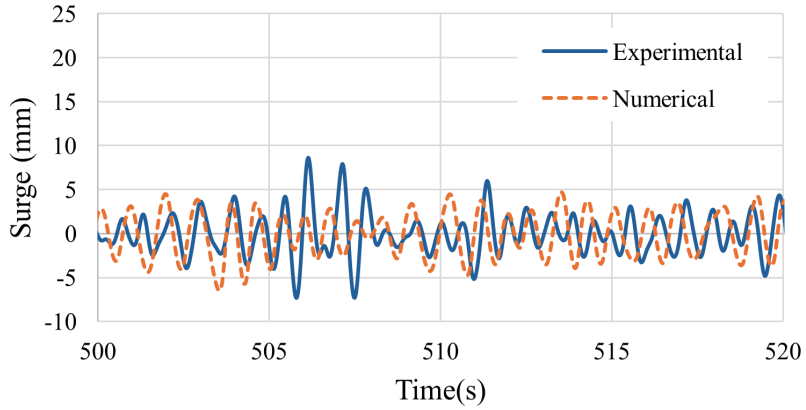

Figure 5.31: Model scale surge displacement of body 1 in irregular wave 1.

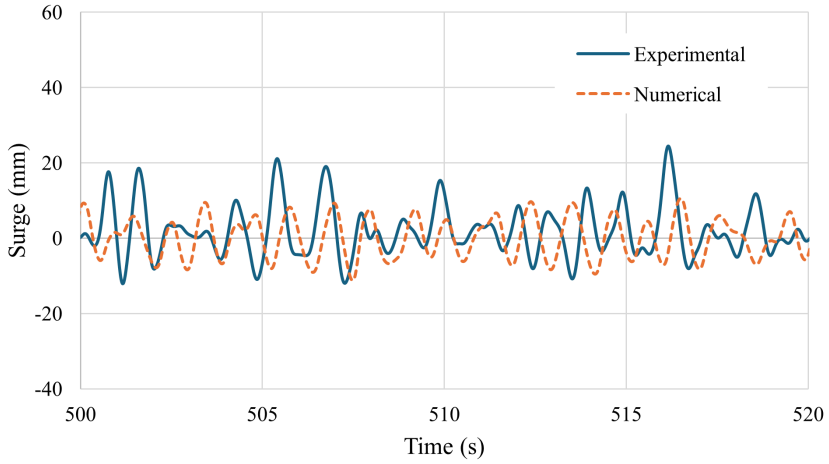

Figure 5.32: Model scale surge displacement of body 1 in irregular wave 2.

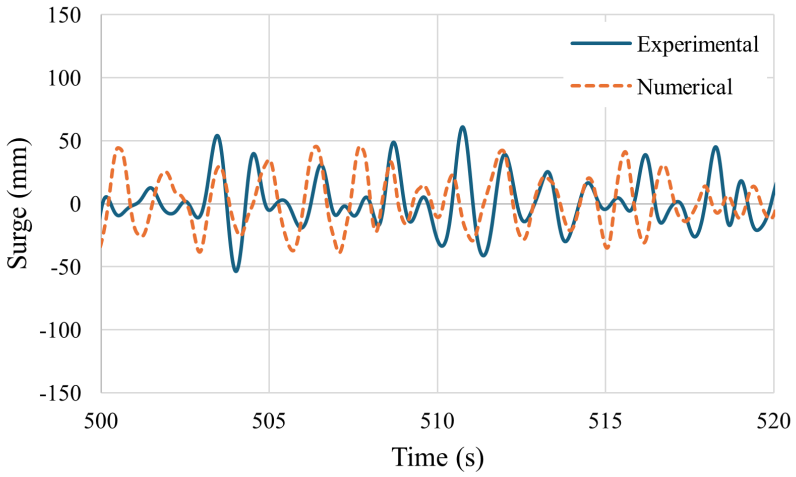

Figure 5.33: Model scale surge displacement of body 1 in irregular wave 3.

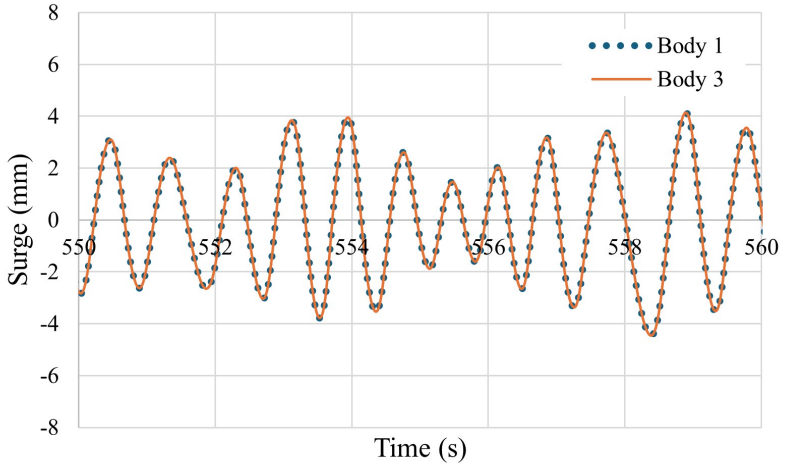

Figure 5.34: Model scale numerical surge displacement comparison of body 1 against body 3, in irregular wave 1.

In the statistical analysis, it is evident that the experimental test results yielded larger maximum and minimum surge motion for all three irregular waves. The experimental max and minimum values are more than twice the numerical ones. However, the mean surge motion and the significant surge motion are nearly equal for both models. This would indicate that the numerical model is good. Also, while the time history of the waves were imported, meaning the waves are identical, the actual tools used to measure the response of the experimental floating body are not ideal, which affects the results. It is important to note that the mean and significant surge motion is calculated in the same manner one would calculate mean wave height and significant wave height for an irregular wave, only applied for the floating body's surge motion. Essentially, the mean surge motion would tell a person the average peak value in the positive surge direction, while the significant surge motion is the average surge motion of the highest one-third peaks observed in the positive surge direction.

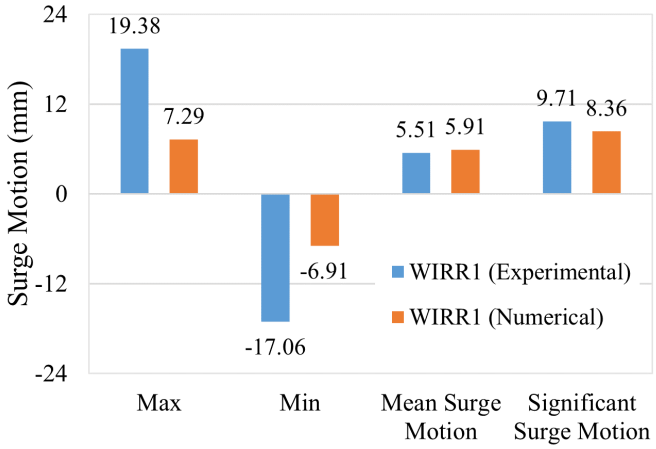

(a) Surge motion statistics for body 1 during irregular wave 1.

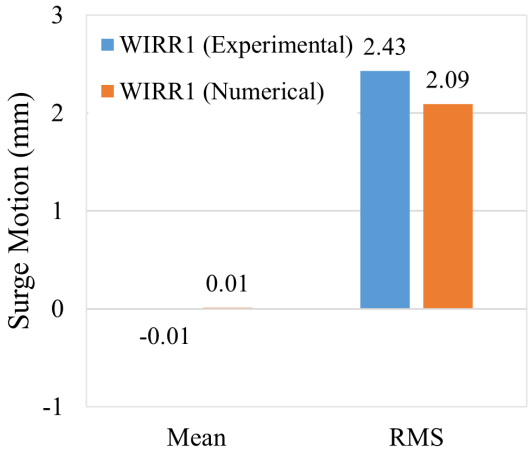

(b) Surge motion mean and rms for body 1 during irregular wave 3.

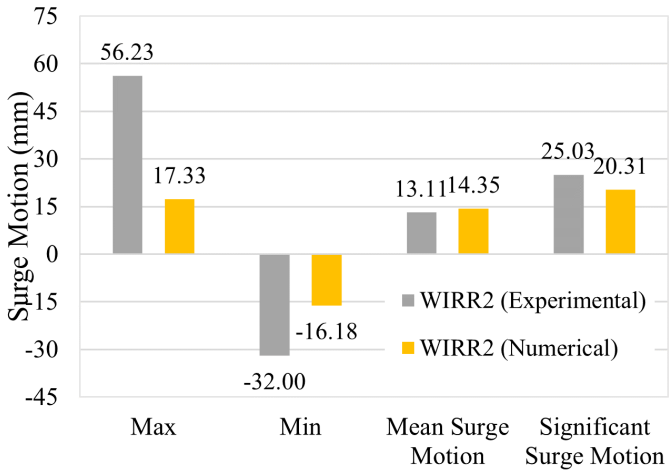

(c) Surge motion statistics for body 1 during irregular wave 2.

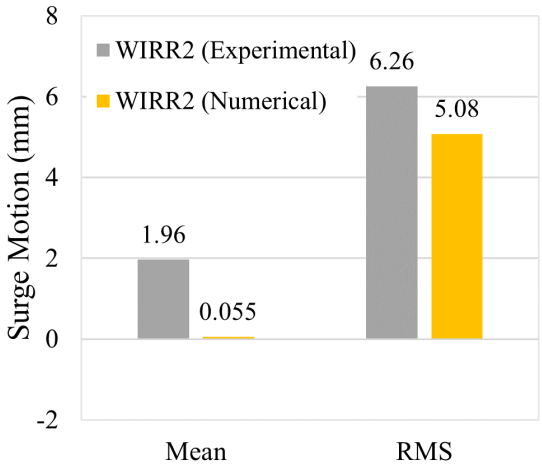

(d) Surge motion mean and rms for body 1 during irregular wave 2.

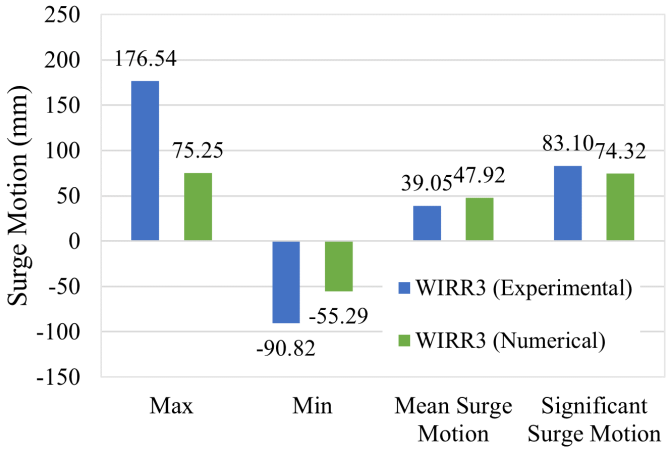

(e) Surge motion statistics for body 1 during irregular wave 3.

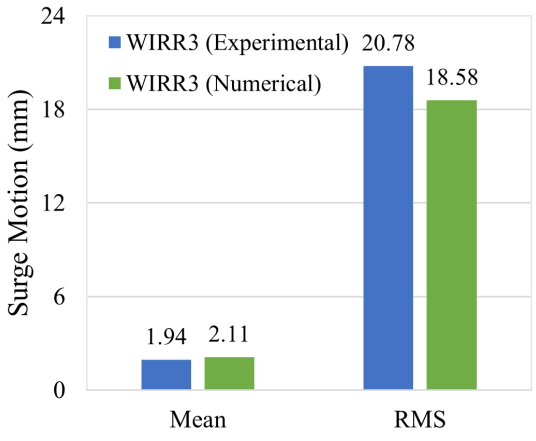

(f) Surge motion mean and rms for body 1 during irregular wave 3.

Figure 5.35: Model scale surge motion statistics for body 1 during irregular waves.

5.4.3 Heave Motion of Body 1

The heave motion of body 1 during the irregular waves are shown in figures 5.36, 5.37, and 5.38.

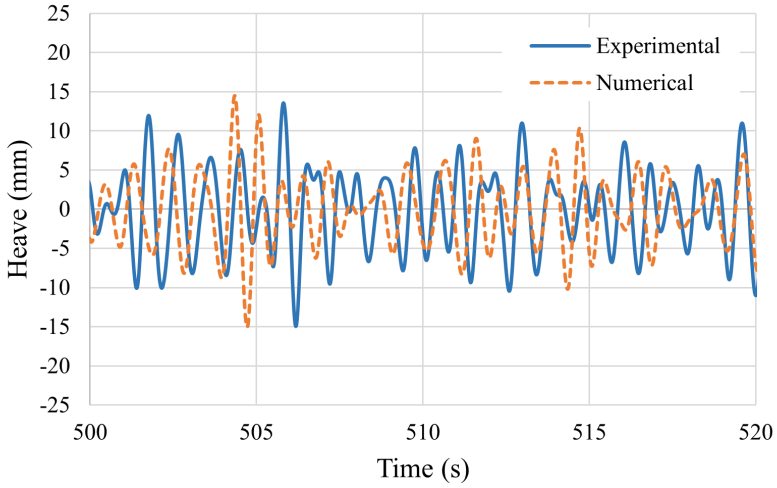

Figure 5.36: Model scale heave displacement of body 1 in irregular wave 1.

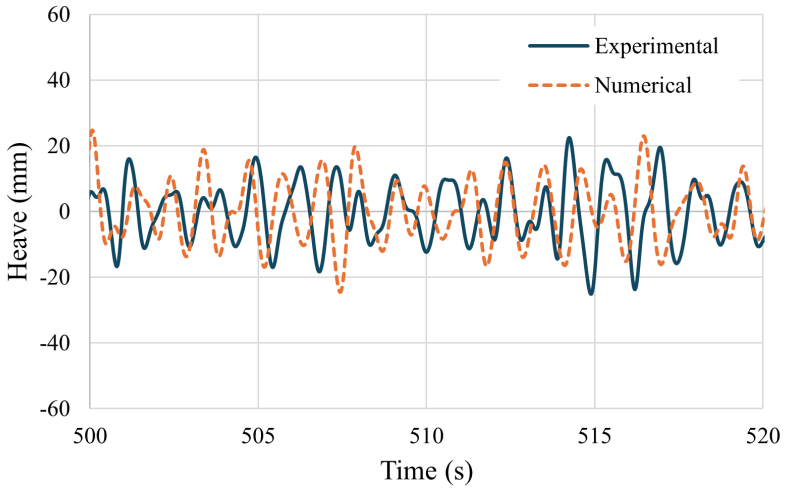

Figure 5.37: Model scale heave displacement of body 1 in irregular wave 2.

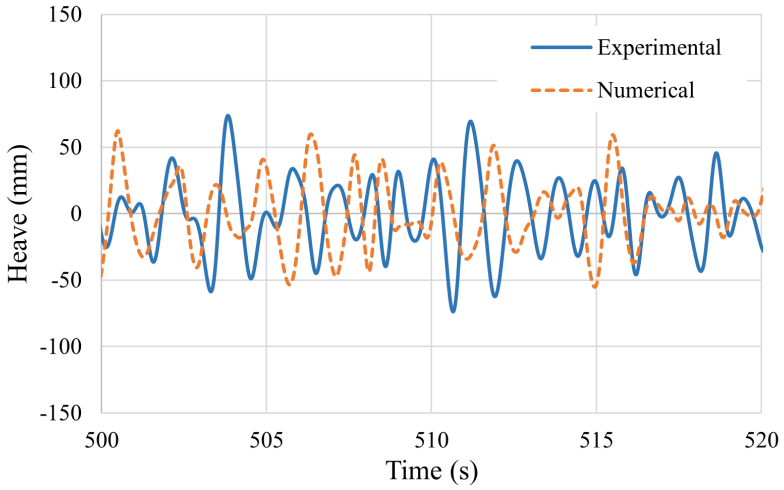

Figure 5.38: Model scale heave displacement of body 1 in irregular wave 3.

The statistical results gotten from the results are given in Figure 5.39. During irregular wave 1, the numerical and experimental maximum is quite similar, the difference in minimum is more substantial. The maximum of the experimental results is 19.16mm, while the numerical one is 17.89mm. So, the experimental maximum is 1.27mm, larger than the numerical one. For the minimum, it is 5.21mm larger.

The significant heave motion is 18.7mm for the experimental and 16.8mm for the numerical mode. At full-scale these correspond to approximately 1.12 and 1.01 meters. This tells us that the most probable maximum vertical motion is around 1 meter. The numerical model underestimates the value by 10.16% in this case. Based on this information, in the case of WIRR1, the numerical model seems to underestimate the damping effects of the physical model.

As the wave height increases the deviation becomes smaller. In the case of WIRR2, the numerical model overestimates the significant heave motion by only 7.4%. For irregular wave 3, this difference is further reduced to 6%, though this time it is an underestimate. So, again, the numerical model is more accurate at replicating the experimental results for larger waves.

The reason for more accuracy for larger waves is likely because of the fact that larger waves tend to have more significant hydrodynamic damping and added mass effects, so while the numerical model underestimates the damping of the physical model, that gap is diminished by the increased added mass and hydrodynamic damping.

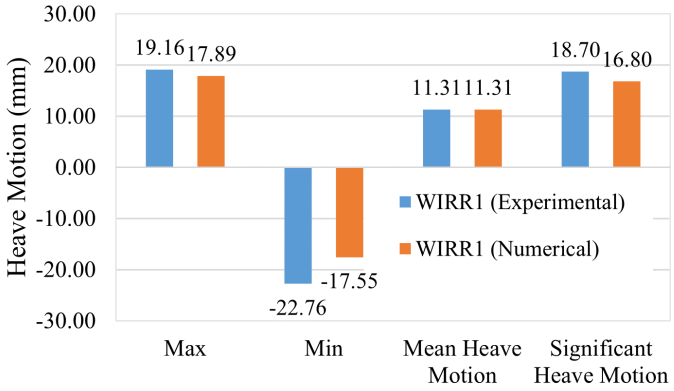

(a) Heave motion statistics for body 1 during irregular wave 1.

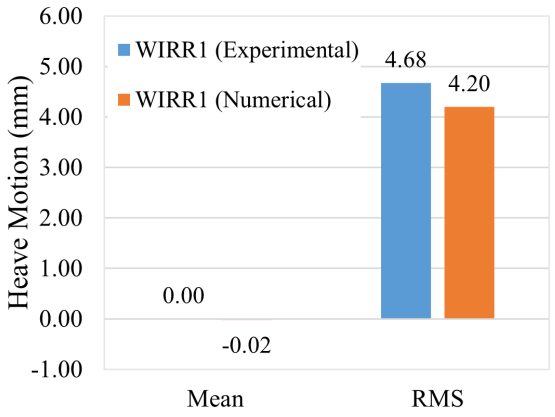

(b) Heave motion mean and rms for body 1 during irregular wave 1.

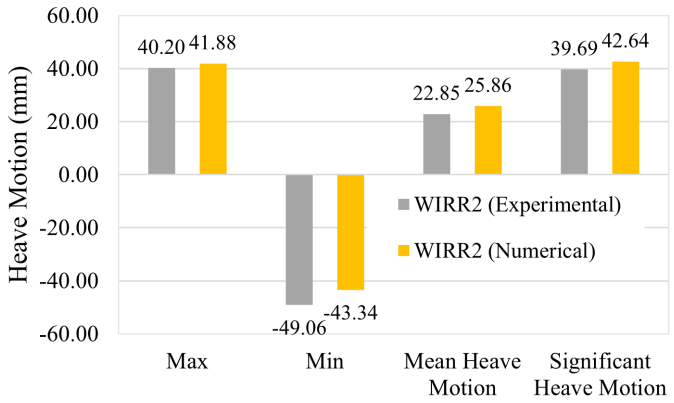

(c) Heave motion statistics for body 1 during irregular wave 2.

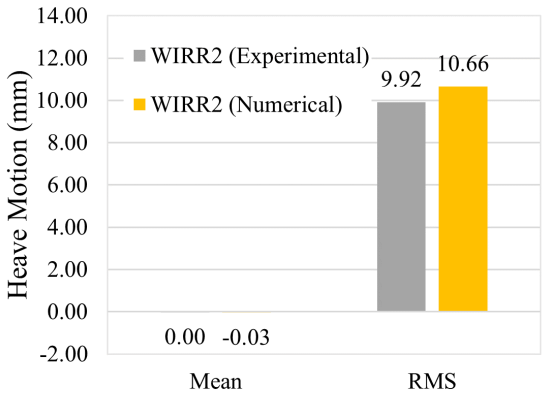

(d) Heave motion mean and rms for body 1 during irregular wave 2.

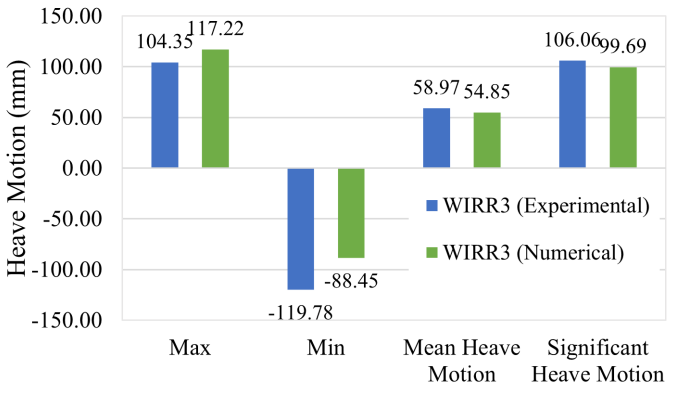

(e) Heave motion statistics for body 1 during irregular wave 3.

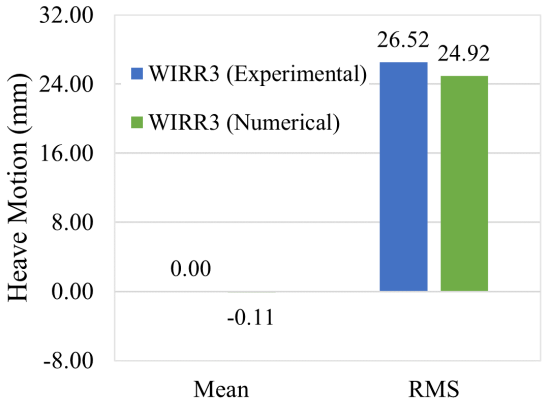

(f) Heave motion mean and rms for body 1 during irregular wave 3.

Figure 5.39: Model scale heave motion statistics for body 1 during irregular waves.

5.4.4 Response Amplitude Operators

Figures 5.40, 5.42, and 5.44 depict the numerical surge RAOs of floating body 1 for the three irregular waves. The curves show high motion response at smaller wave frequencies, after which the RAOs start rapidly decreasing and finally plateau. The transition from very responsive to almost non-responsive happens at around 0.5Hz for all three waves. The peaks are for all three curves appear between 0.01 and 0.25Hz. The reason why the RAO is so high for lower frequencies is because of resonance, where the natural frequency of the body aligns with that of the waves and result in excessive displacement. Naturally this is undesired, since these peaks in motion risk harming the FPV array. Overall, one can say that waves that are shorter and more frequent, have less of an impact on the FPV array. Meanwhile, longer and less frequent waves have a significantly higher impact on the motion of the body.

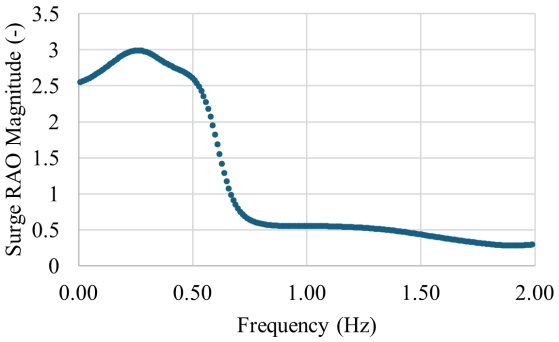

Figure 5.40: Model scale surge displacement RAO of irregular wave 1, body 1.

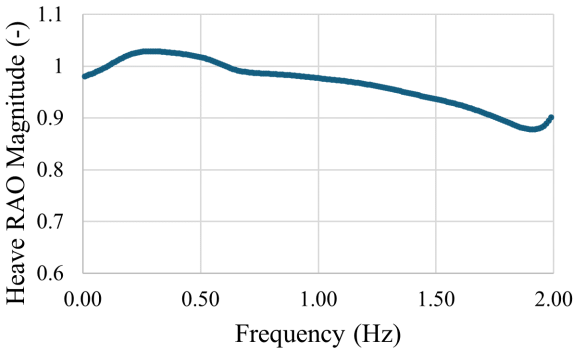

Figure 5.41: Model scale heave displacement RAO of irregular wave 1, body 1.

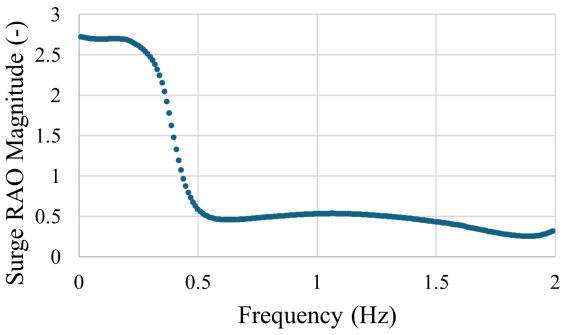

Figure 5.42: Model scale surge displacement RAO of irregular wave 2, body 1.

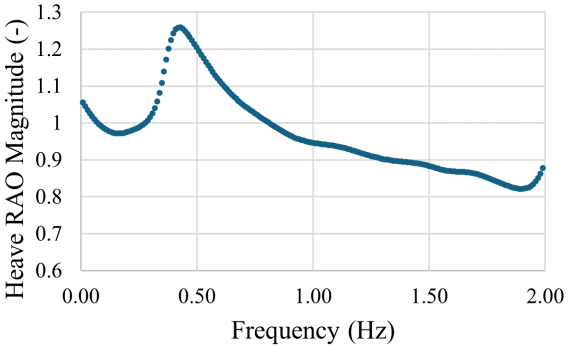

Figure 5.43: Model scale heave displacement RAO of irregular wave 2, body 1.

The heave RAOs are shown in figures 5.41, 5.43, and 5.45. As expected, the motion is more consistent in heave than surge. The motion response is slightly higher for smaller frequencies, but for most frequencies, the RAO magnitude in heave lies between 0.9 and 1. The only exception to this being at around 0.45Hz for WIRR2, where the RAO magnitude peaks, likely due to resonance. It is thus noted that waves with these frequencies lead to larger oscillations that could harm the FPV system.

Overall, these figures demonstrates that the body moves nearly the same vertical distance as the wave height during heave, though it is not unexpected that a shallow draft float would contour the waves in heave.

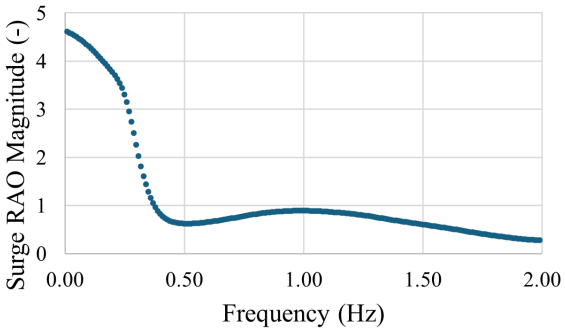

Figure 5.44: Model scale surge displacement RAO of irregular wave 3, body 1.

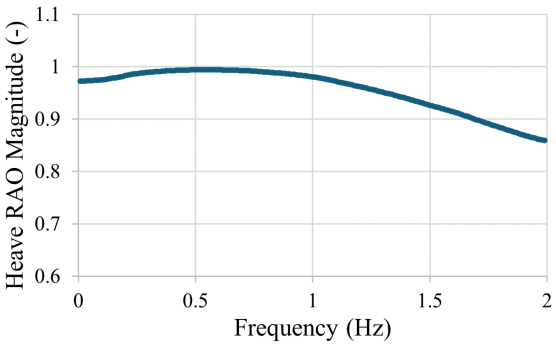

Figure 5.45: Model scale heave displacement RAO of irregular wave 3, body 1.

5.4.5 Mooring Tension

Tension in the mooring lines during irregular waves are shown in figures 5.46, 5.47, and 5.48. For irregular waves 1 and 2 the tension in the experimental lines is clearly higher than for the numerical lines. Though, as stated in 5.3.4, the comparison would be better if the precision of the measuring instrument was increased for the physical model. The comparison is better for irregular wave 3, where the differences in mean and peak-to-peak tension between the numerical and experimental tests are reduced.

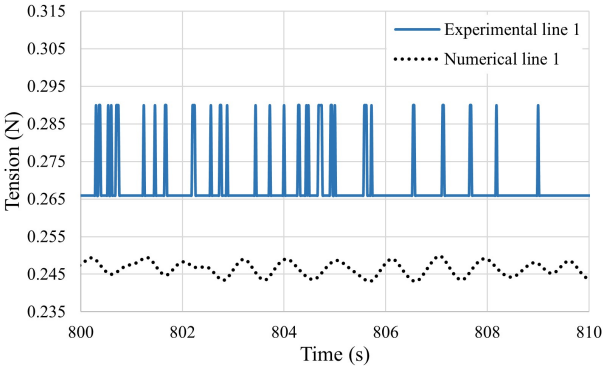

(a) Tension force in numerical and experimental line 1.

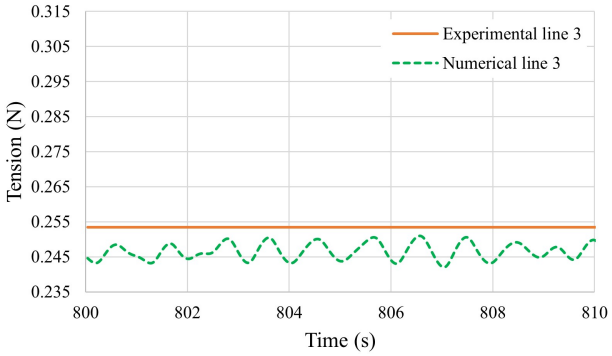

(b) Tension force in numerical and experimental line 3.

Figure 5.46: Model scale mooring tension for body 1 during irregular wave 1 (WIRR1).

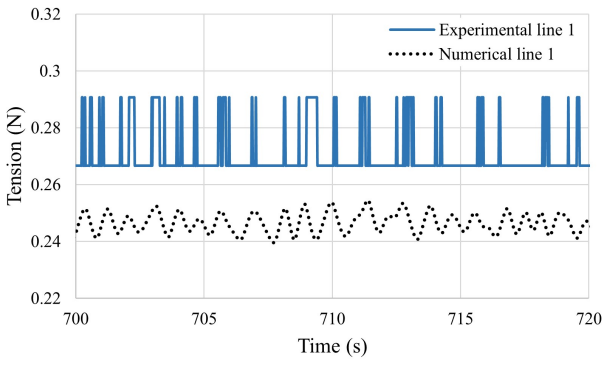

(a) Tension force in numerical and experimental line 1.

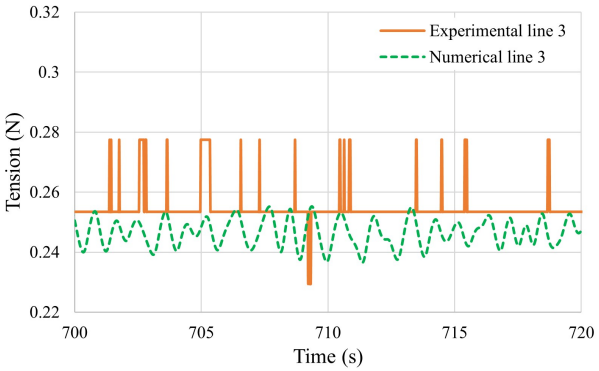

(b) Tension force in numerical and experimental line 3.

Figure 5.47: Model scale mooring tension for body 1 during irregular wave 2 (WIRR2).

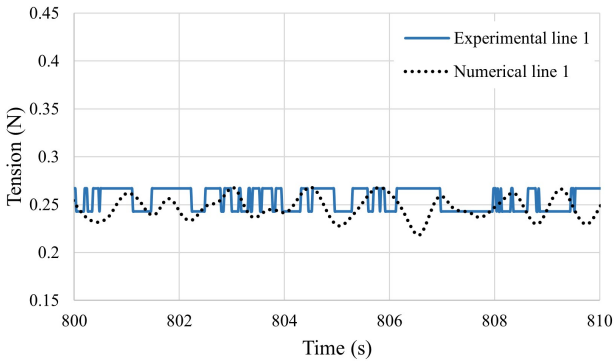

(a) Tension force in numerical and experimental line 1.

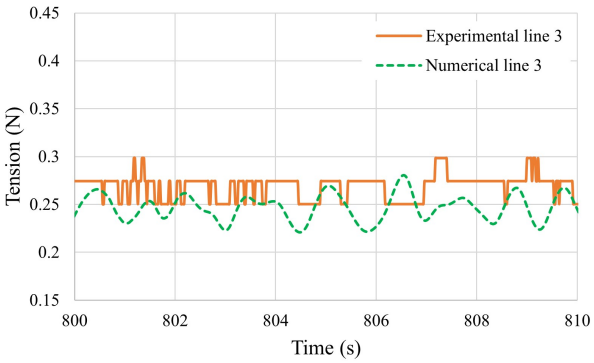

(b) Tension force in numerical and experimental line 3.

Figure 5.48: Model scale mooring tension for body 1 during irregular wave 3 (WIRR3).

Figure 5.49 shows the statistical values extracted from the mooring line time history analysis.

While the mean tension is approximately 0.247N for all three waves in numerical line 1, for the experimental test the mean ranges from 0.265 to 0.271N. The difference in mean is highest for WIRR2, being 0.024N higher for the experimental model. The numerical model also underestimates the maximum and minimum tension in line 1 for all three waves. For example, the maximum tension in line 1 during irregular wave 3 is 0.387N for the experimental model, but only 0.300N for the numerical model.

For line 3, the numerical mean tension estimate is at worst only 6.8% lower than the measured experimental result. Additionally, the numerical model predicts lower maximum tension, but higher minimum tension when compared to the experimental results. For instance, in WIRR3, the numerical maximum is 0.032N smaller than the experimental one, but the minimum tension is 0.06N higher than the experimental.

Overall, if one compares mooring line 1 to mooring line 3, in both numerical and experimental results, the tension is higher in line 1 than in 3. This relationship between the two lines is expected, considering one line is upstream and the other is downstream from the floating body. Furthermore, the tension increases with wave height. The same can be said of the variation in tension, as evidenced by the standard deviation.

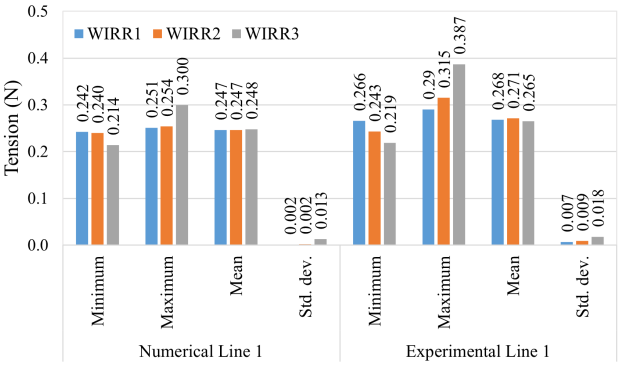

(a) Tension statistics for mooring line 1.

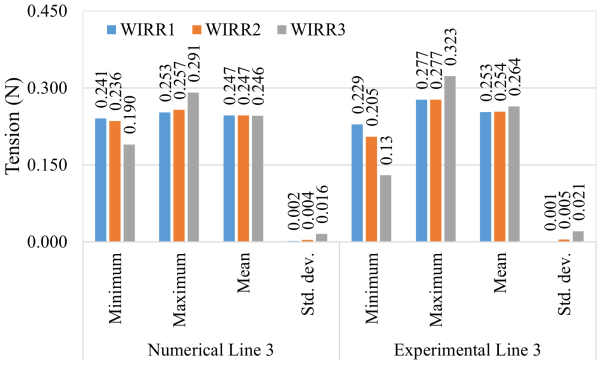

(b) Tension statistics for mooring line 3.

Figure 5.49: Model scale mooring line tension statistics for irregular waves.

5.4.6 Connecting Rope Tension

The connecting rope tension for irregular waves 1, 2, and 3 are shown in figures 5.50, 5.51, and 5.52 respectively.

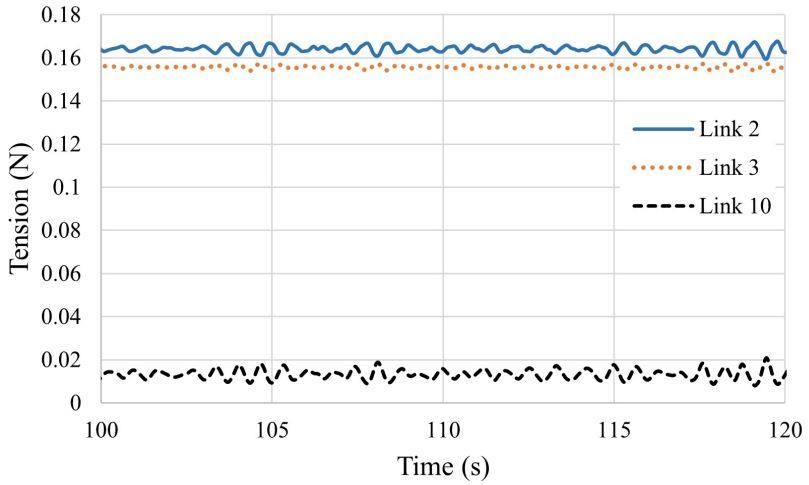

Figure 5.50: Model scale connecting rope tension for body 1, irregular wave 1.

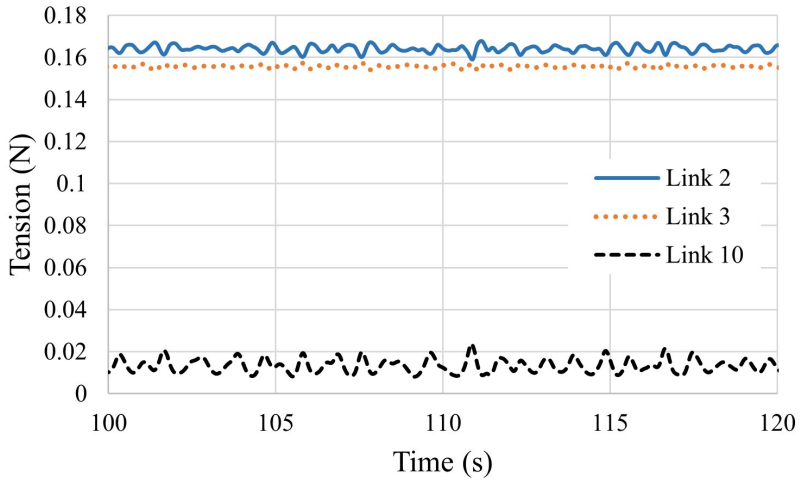

Figure 5.51: Model scale connecting rope tension for body 1, irregular wave 2.

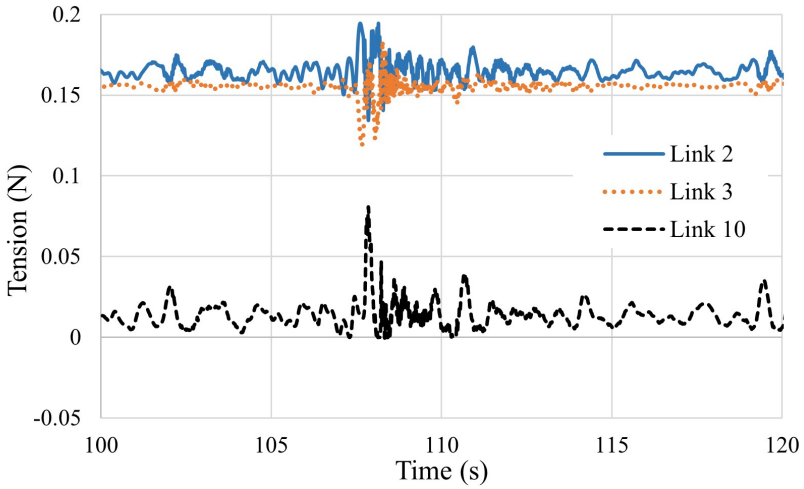

Figure 5.52: Model scale connecting rope tension for body 1, irregular wave 3.

In figure 5.53a, we see that the statistical tension values measured are nearly identical for connecting lines 2 and 3, while being significantly smaller for line 10, which is diagonal. One reason for the tension being smaller in line 10, is the wave heading. The wave heading is 0°, which means it is heading in the exact positive x-direction. The diagonal line on the other hand connects two floating bodies at a 45° angle. Thus, the diagonal line experiences less loading, and would likely last longer than the straight lines.

The standard deviation of the irregular waves are given in 5.53b. It is noted that the variability in tension for the different waves are smallest for irregular wave 1, and largest for irregular wave 3, for all three connecting ropes.

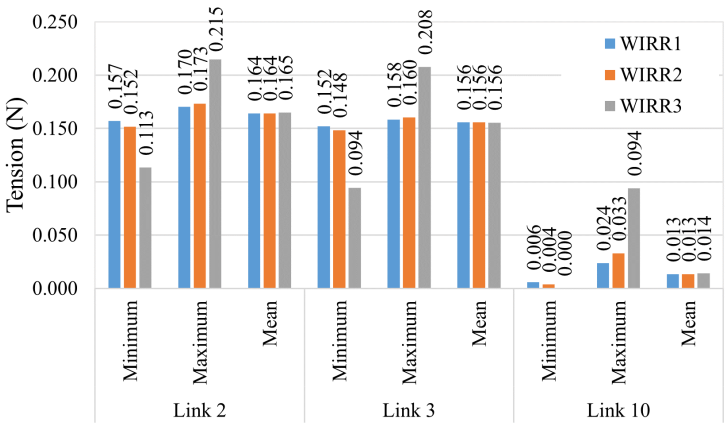

(a) Maximum, minimum, and mean of connecting ropes 2, 3, and 10.

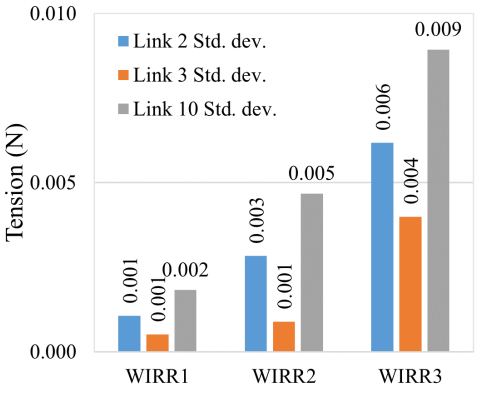

(b) Standard deviation of connecting ropes 2, 3, and 10.

Figure 5.53: Model scale statistics for connecting ropes during irregular waves.

5.5 Connecting Rope Sensitivity Study

A sensitivity study was conducted to understand how a change in stiffness might affect the connecting ropes during regular and irregular waves. The original stiffness values are given in Table 4.4.

5.5.1 Regular Wave Case

The results of the sensitivity study for connecting ropes during a regular wave is seen in figure 5.54, the wave in question being regular wave 10.

The sensitivity study reveals that reducing the stiffness of the connecting ropes eliminates snatching. It could be that the higher stiffness values might have made the ropes too rigid, leading to snatching. While reduced stiffness allows the system to smoothly adapt to variations without abrupt movements. Or, perhaps the natural frequency of the diagonal link aligned with that of the wave, causing resonance. So that when the stiffness was reduced, the natural frequency was no longer aligned, effectively eliminating the snatching.

For links 2 and 3, a lower stiffness leads to less tension as well, but higher overall tension in link 10. It also leads to more distension in links 2 and 3. Where once the length was nearly constant, reducing the stiffness has made the ropes less rigid and therefore more flexible. The unstretched length for the straight ropes was 27.26mm.

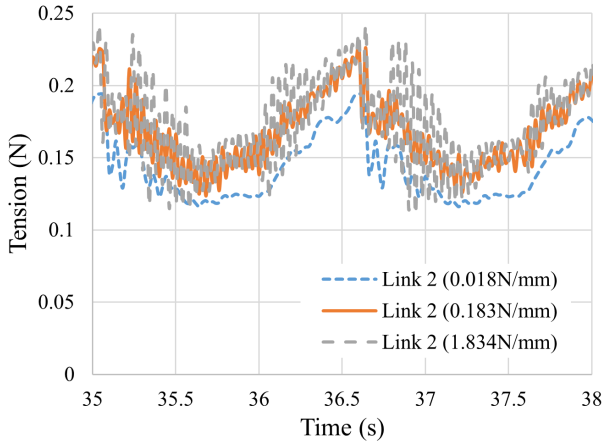

(a) Tension study for link 2 for different rope stiffness values.

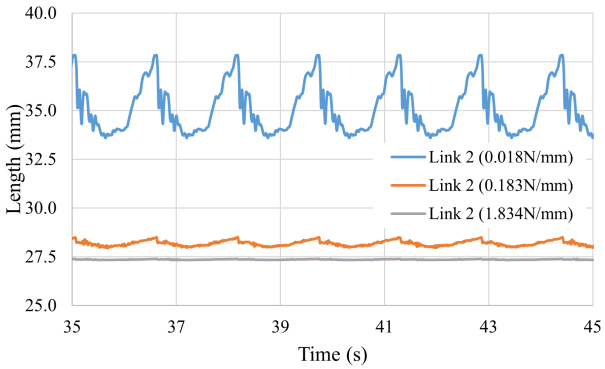

(b) Length study of link 2 for different rope stiffness values.

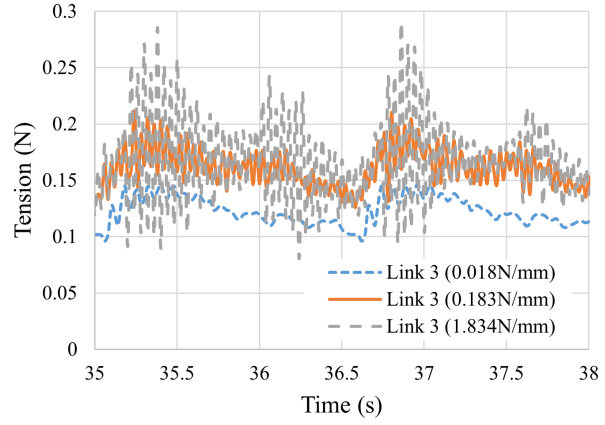

(c) Tension study for link 3 for different rope stiffness values.

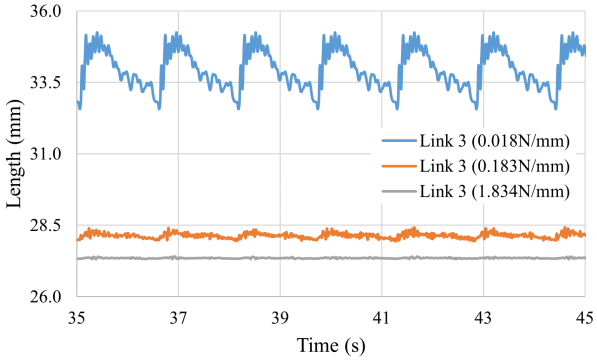

(d) Length study of link 3 for different rope stiffness values.

Figure 5.54: Sensitivity study at model scale for links 2, 3, and 10 during regular wave 10.

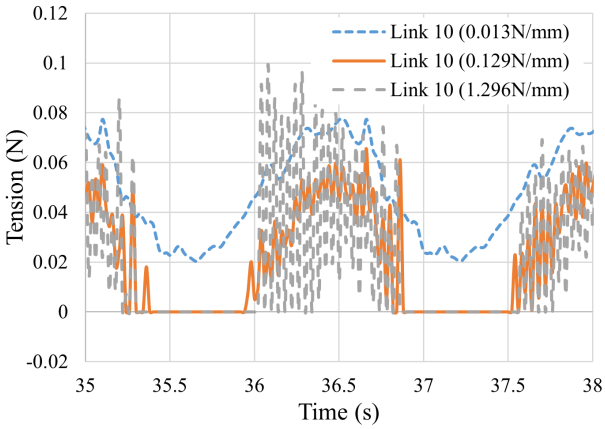

(e) Tension study for link 10 for different rope stiffness values.

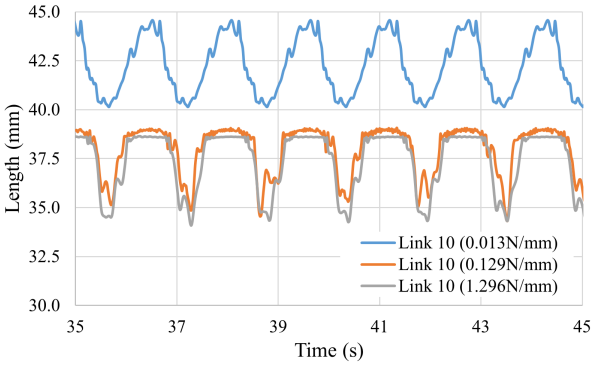

(f) Length study of link 10 for different rope stiffness values.

Figure 5.54: Sensitivity study at model scale for links 2, 3, and 10 during regular wave 10.

5.5.2 Irregular Wave Case

The results of the sensitivity study for connecting ropes during an irregular wave is seen in figure 5.55, the wave in question being irregular wave 1.

Similarly to the regular wave results, it is observed that reducing the stiffness helps remove snatch loads. The same trend seen in the regular wave sensitivity study resurfaces for the irregular wave. That, if one reduces the stiffness, the tension in links 2 and 3 decrease, while the tension in link 10 (diagonal link) increases. It is also noted that the length in the links are smaller and more constant for higher stiffness values. The diagonal link (connecting rope 10) also experiences less tension than the other two connecting ropes.

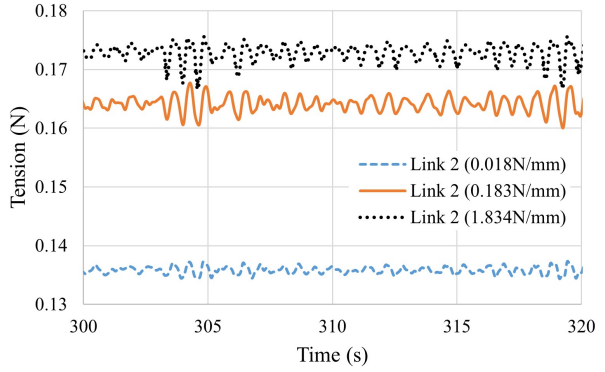

(a) Tension study for link 2 for different rope stiffness values during WIRR1.

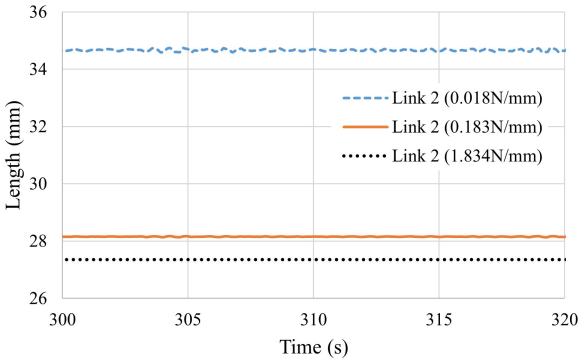

(b) Length study of link 2 for different rope stiffness values during WIRR1.

Figure 5.55: Sensitivity study at model scale for links 2, 3, and 10 during irregular wave 1 (WIRR1).

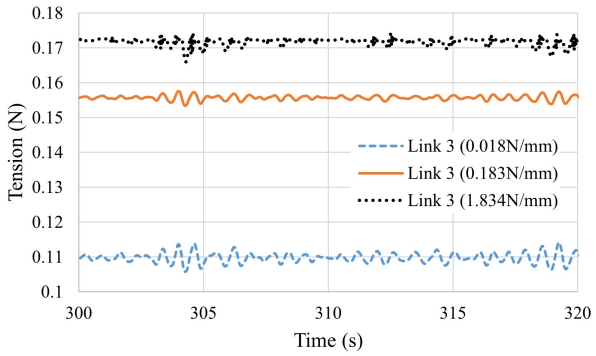

(c) Tension study for link 3 for different rope stiffness values during WIRR1.

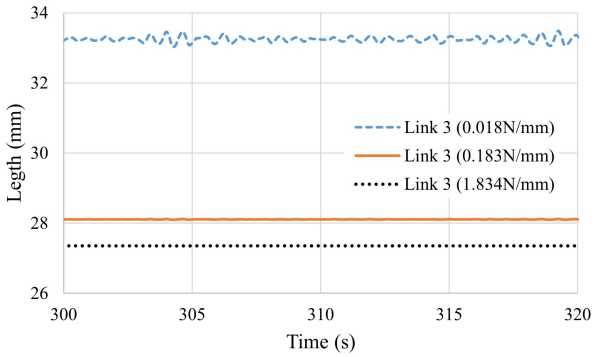

(d) Length study of link 3 for different rope stiffness values during WIRR1.

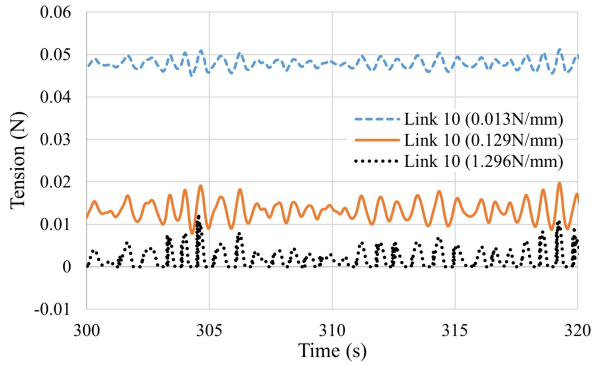

(e) Tension study for link 10 for different rope stiffness values during WIRR1.

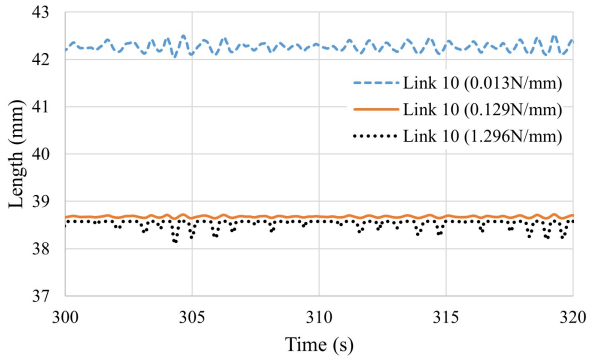

(f) Length study of link 10 for different rope stiffness values during WIRR1.

Figure 5.55: Sensitivity study at model scale for links 2, 3, and 10 during irregular wave 1 (WIRR1).

Chapter 6

Conclusions & Further Work

The aim of this thesis was to create, calibrate, and analyse a numerical model of a 3x2 Floating Photovoltaic (FPV) array, and comparing those results against the results obtained from a physical model. The physical and numerical models were 1/60th full scale.

The thesis completes the objective of creating a numerical model that is capable of simulating realistic results. The FPV system was exposed to regular and irregular waves, and through comparison to the physical model, showed the following.

- Free decay tests are performed for a single floating body within the array in the heave, pitch, and roll degrees of freedom. The numerical model, when compared against the physical model, underestimates the damping in heave by 10.3%, and overestimates the pitch and roll by 6.4% and 3.3% respectively.
- Surge and sway free decay test are performed for the moored 3x2 FPV system, and it is found that the numerical model keeps oscillating indefinitely unless a linear or quadratic damping coefficient is applied to the floating bodies. The surge and sway decay motion of the physical and numerical models align when a quadratic damping coefficient of 5e-7$\frac{N}{(mm/s)^2}$ is applied to the floating bodies in the surge and sway degrees of freedom.
- The surge motion of floating body 1 is analysed when subject to regular waves 3, 7, and 10. The maximum surge motion is very similar for numerical and physical models. The numerical model underestimates the maximum surge for all three waves, but the worst estimate, which is for Regular Wave 7 (WR7), is only off the mark by 0.89mm (an 8.5% underestimation). The comparison of minimum surge motion paints another picture. While the minimum surge motion of body 1 during regular waves 3 and 7 align closely for the two models, for Regular Wave 10 (WR10), the numerical model overestimates the minimum surge by 61.42mm, which is approximately twice as much surge motion as the physical model showed.
- The statistical analysis of surge motion of floating body 1 during irregular waves reveal that the numerical model generally underestimates the maximum and minimum motion. The numerical maximum and minimum values are between 2 to 3 times smaller than the experimental ones for all three waves. The mean and significant surge motion yield better comparisons. The numerical model underestimates the significant surge motion for all three irregular waves, by 18.86% at worst to 10.57% at best. The numerical mean surge motion on the other hand is overestimated for all three waves. Here the best numerical estimate is 0.4mm (7.26%) higher than the physical, in the case of Irregular Wave 1 (WIRR1).
- The numerical model has high accuracy in heave when comparing numerical against experimental motions, based on the statistical results for heave motion of the floating

body during regular waves. The numerical model overestimates the maximum heave for body 1 during Regular Wave 3 (WR3) by 1.34mm (6.44%). For WR7, which is longer and taller than regular wave 3, the numerical model overestimates the maximum heave by 0.94mm (2.59%). In the case of WR10, the extreme wave, the overestimate is also 2.59% (3.21mm).

- The statistical analysis of heave motion of floating body 1 during irregular waves show the numerical model is far more precise at predicting the maximum and minimum heave motion than surge, with the worst prediction being that the numerical model underestimates the minimum heave motion by 26.16% or 31.33mm. The best comparison appears in Irregular Wave 2 (WIRR2), where the numerical model overestimates the maximum heave by 1.68mm or 4.18%. The numerical model also predicts the mean heave motion of body 1 perfectly for WIRR1, at exactly 11.31mm.

- When the FPV system is exposed to regular waves, the magnitude of the surge Response Amplitude Operators (RAOs) decrease with increasing wave period. The exception to this trend is WR10, the extreme wave, which is significantly taller but has a similar wave period to the other regular waves, making this wave much steeper than the others. The RAO for body 1 during WR3 obtained from the numerical model, has a difference of 8.35% compared to the physical model. In the case of WR7, the difference is reduced to 6.03%. The least accurate prediction occurs for WR10, the extreme wave, where the difference is 20.77%.

- The heave RAOs obtained from the regular wave test show that the motion response of the floating body in this particular Degree of Freedom (DOF) is stable. The magnitude of the RAOs range between 0.9 and 1.1, meaning the body follows the wave as desired in heave. The heave RAOs of the numerical model have a percentage difference of less then 5.67% compared with those of the physical model for all ten waves. The highest difference is for WR7 at 5.67%. Regular wave 3 has a difference of 3.01%, and WR10 has an almost negligible difference of only 0.27%.

- The surge RAOs for the numerical model are obtained for floating body 1 when subjected to the three irregular waves. The RAOs show a trend of high magnitude at low frequency. For WIRR1, the surge RAO has a magnitude of 2.5 at 0.1Hz, peaking at a magnitude of 3 at 0.25Hz, then rapidly decreasing until 0.75Hz, and reaching a plateau. A similar trend is observed for irregular waves 2 and 3, with no peaks however.

- The heave RAOs for the numerical model in irregular waves depict a stable trend. The magnitude of all the RAOs range between 0.9 and 1 for most frequencies, with the notable except of WIRR2, where the heave RAO peaks with a magnitude of approximately 1.25 at 0.4Hz.

- Tension in mooring lines 1 and 3 is analysed when the FPV system is exposed to irregular waves. The numerical model is more accurate in predicting tension in line 3 than line 1. At worst, the numerical model underestimates the mean tension in line 3 by 6.82% and by 8.9% in line 1. The numerical model also underestimates both the maximum and minimum tension in line 1 for all three irregular waves, the largest discrepancy appearing in Irregular Wave 3 (WIRR3), where the maximum tension is estimated by the numerical model to be 0.3N, but 0.387N by the experimental model.

- The diagonal connecting lines exhibited snatch loads under WR10 and WIRR3. The pretension in the diagonal connecting lines should be increased so as to avoid these snatch loads, as over time these loads could lead to failure of the lines. The lines should preferably always be in tension. A sensitivity study also revealed that smaller line stiffness contributed to reducing snatch loads.

There are many possibilities for future work. The most interesting would be to study the power performance of the kind of FPV array described in this thesis, for which the pitch and roll motion of the floating bodies during waves would also need to be studied. One could also do a structural analysis of which materials work best for the FPV array. Different types of mooring systems could also be of interest, such as catenary or taut-leg systems, to see if there are more realistic ways of mooring the FPV array to the seabed.

Appendix A

Energy Research Project Abstract

Offshore Floating Photovoltaics (FPV) has recently emerged as a possible solution to the increased renewable energy demand. However, the ocean is a harsh environment that presents many challenges, such as waves, wind, and current. As such, the aim of this study is to analyse the hydrodynamic behaviour of a single body and how it is affected by additional damping in the form of Morison elements, and external stiffness. As well as exploring the hydrodynamic interaction of multi-body FPV array's. To this end, a diffraction analysis program called OrcaWave was used, which calculates loads on the bodies and their motion response, as well as the added mass and damping, for wet bodies because of waves using potential flow theory. The results indicate that the bodies become almost independent of the wave periods as the wave periods increase. It is also observed that expanding array's affect the added mass, damping, as well as the displacement experienced by bodies due to waves [17].

Appendix B

Software Platforms

B.1 OrcaFlex

OrcaFlex is an often used software in hydrodynamics when it comes to analysing offshore structures. It was developed by Orcina and offers a wide range of tools for modeling, such as lines for mooring systems, links to create tethers, springs, buoys, winches, and vessels, which together can be used to create complex models such a a moored offshore floating wind turbine. OrcaFlex also allows the user to perform static and dynamic simulations of systems that are exposed to waves, winds, and currents. And with these features, an engineer can assess the safety, risks, stability, fatigue, and other important aspects of a project located on a body of water [34][35][36].

B.2 OrcaWave

OrcaWave is a software developed by Orcina that allows the user to perform diffraction analysis. It is commonly used to analyse offshore projects, by enabling users to create models and simulate its interaction with water and waves. OrcaWave calculates the loading and response on the immersed part of bodies, such as ships and other floating objects, by using potential flow theory. A simulation produces results such as displacement RAOs, added mass, and damping of the floating body among others, that provide the user with insight into how the structure behaves in water under different waves, and even accounts for multi-body interaction [24][36].

B.3 GeniE

GeniE is a flexible and user-friendly software developed by DNV (Det Norske Veritas) for the conceptual modelling of offshore and maritime structures. It allows the modelling of high level geometry such as beams, flat plates, and stiffened shells. It is also possible to perform simulations that include environmental loads such as winds, waves, and currents to inspect the impact of fatigue and stress, whereupon one can improve the quality of the model. It also allows for the creation of finite element meshes (FEM), that can be further refined [37].

Appendix C

Surge Motion of Body 1

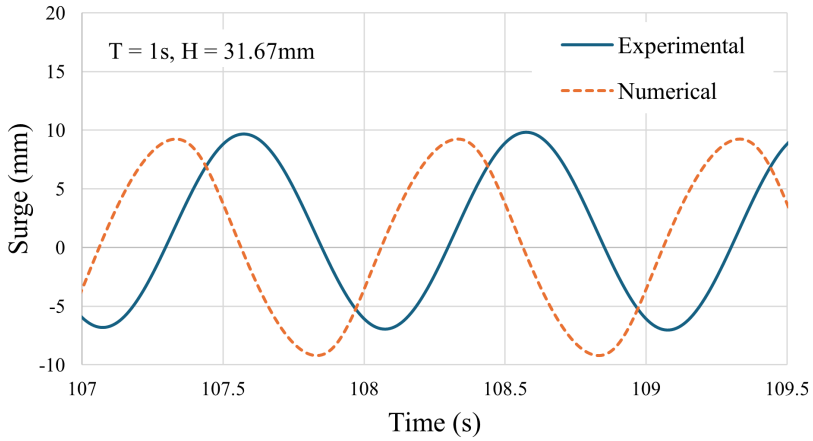

Figure C.1: Model scale surge displacement results of body 1 when subject to regular wave 1.

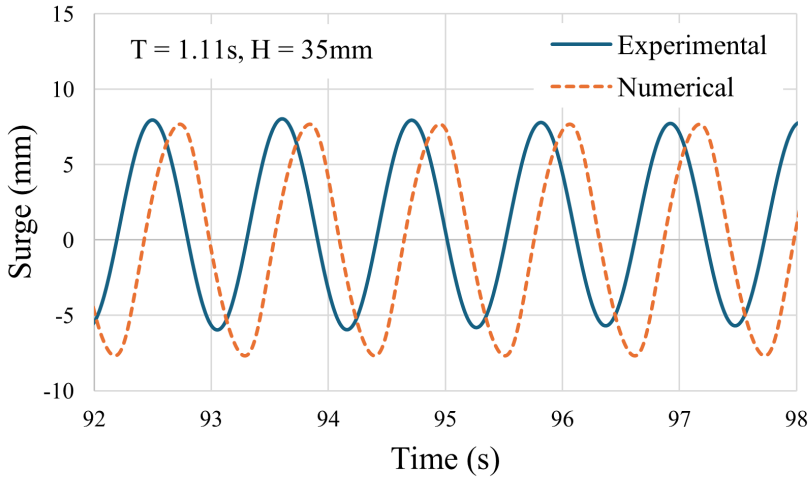

Figure C.2: Model scale surge displacement results of body 1 when subject to regular wave 2.

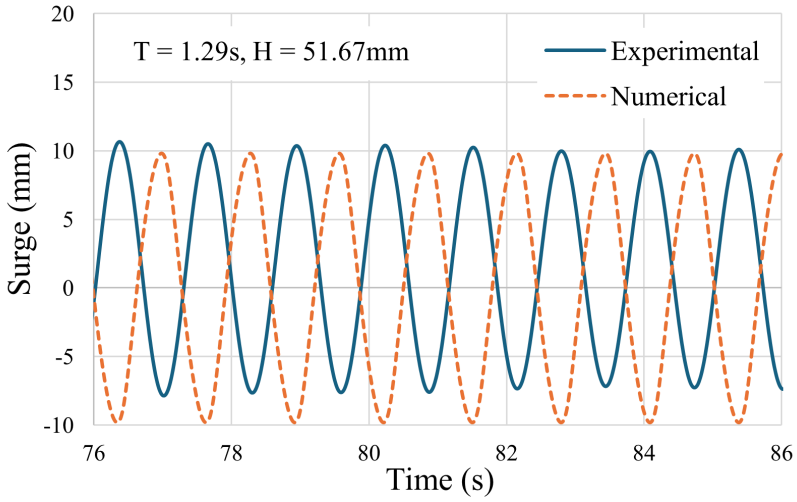

Figure C.3: Model scale surge displacement results of body 1 when subject to regular wave 4.

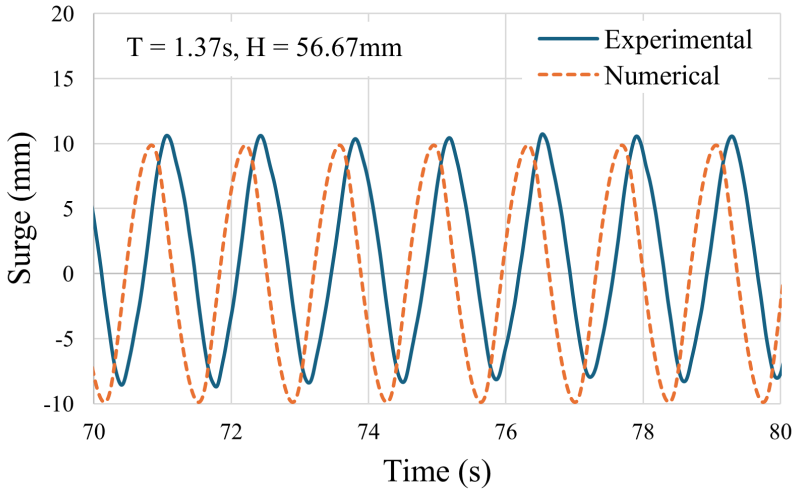

Figure C.4: Model scale surge displacement results of body 1 when subject to regular wave 5.

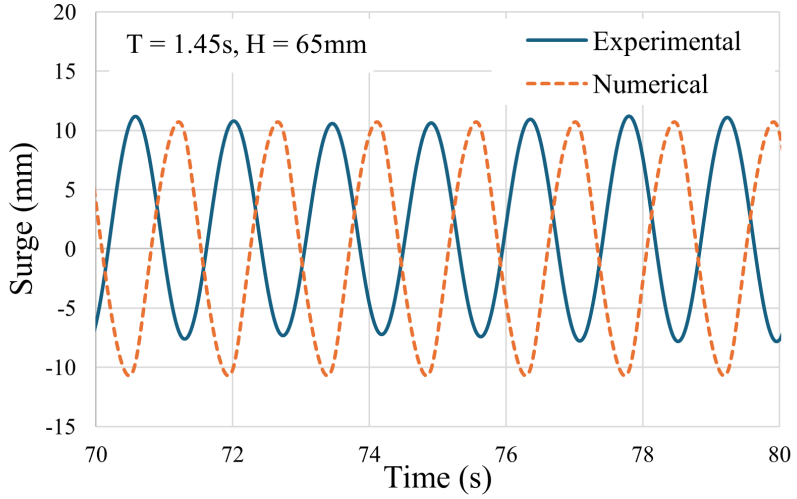

Figure C.5: Model scale surge displacement results of body 1 when subject to regular wave 6.

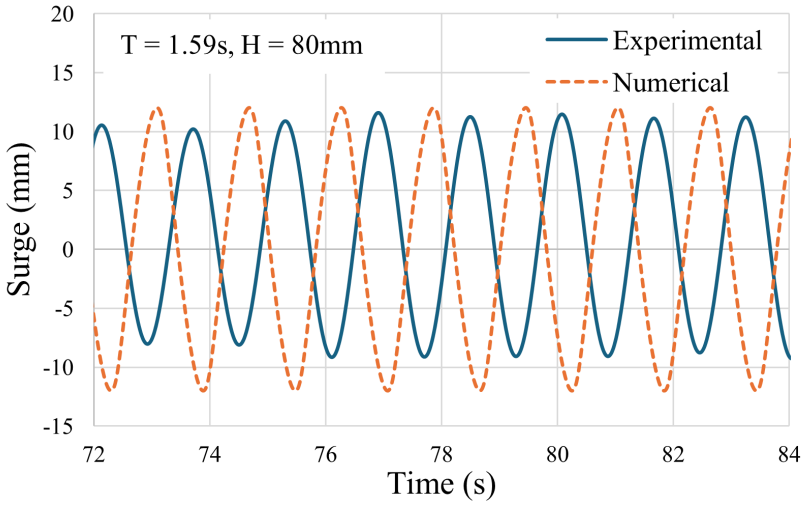

Figure C.6: Model scale surge displacement results of body 1 when subject to regular wave 8.

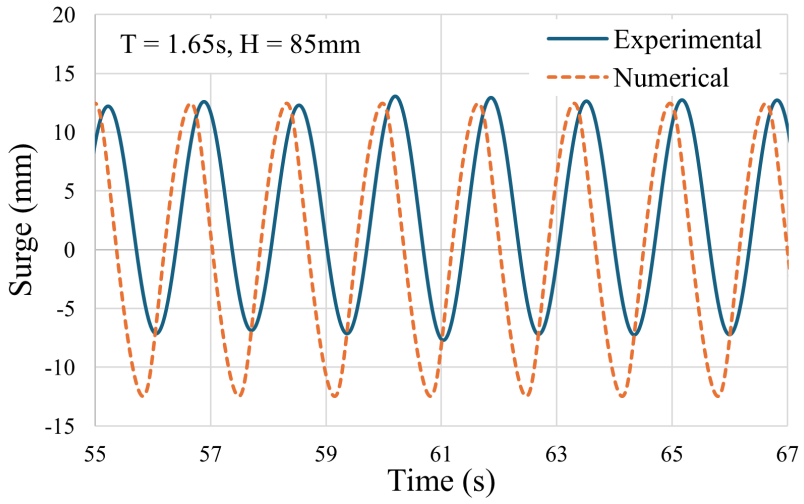

Figure C.7: Model scale surge displacement results of body 1 when subject to regular wave 9.

Appendix D

Heave Motion of Body 1

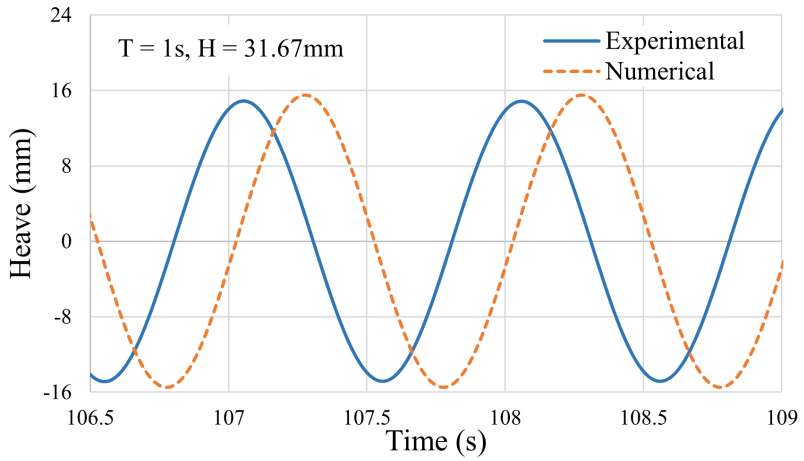

Figure D.1: Model scale heave displacement results of body 1 when subject to regular wave 1.

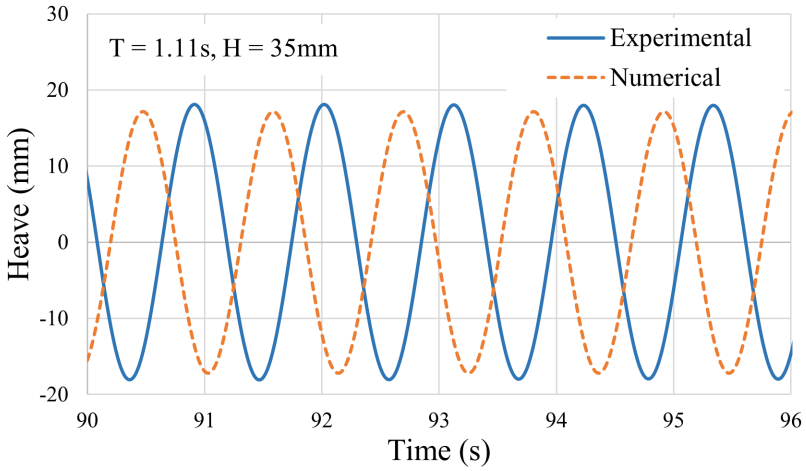

Figure D.2: Model scale heave displacement results of body 1 when subject to regular wave 2.

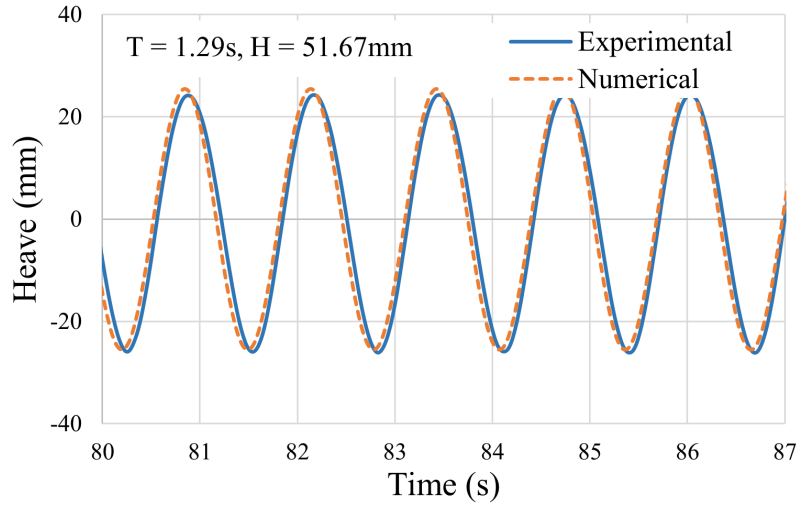

Figure D.3: Model scale heave displacement results of body 1 when subject to regular wave 4.

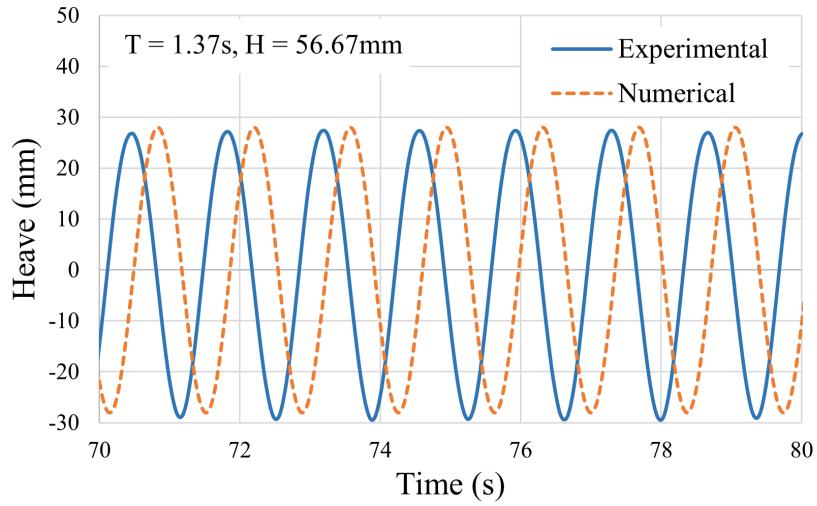

Figure D.4: Model scale heave displacement results of body 1 when subject to regular wave 5.

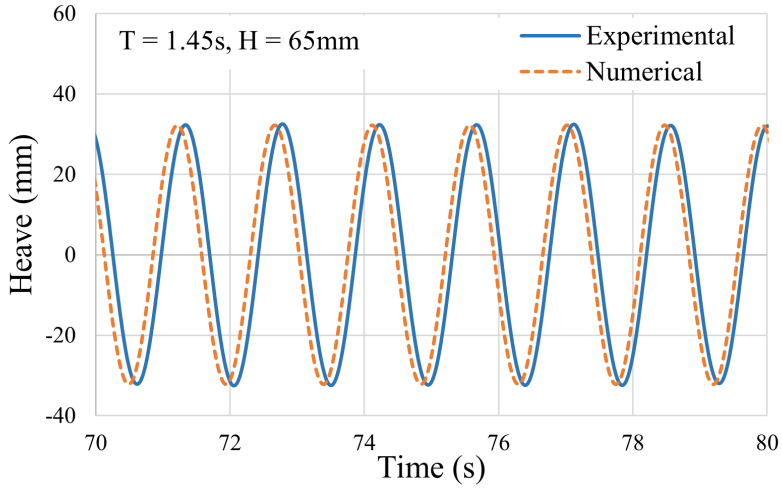

Figure D.5: Model scale heave displacement results of body 1 when subject to regular wave 6.

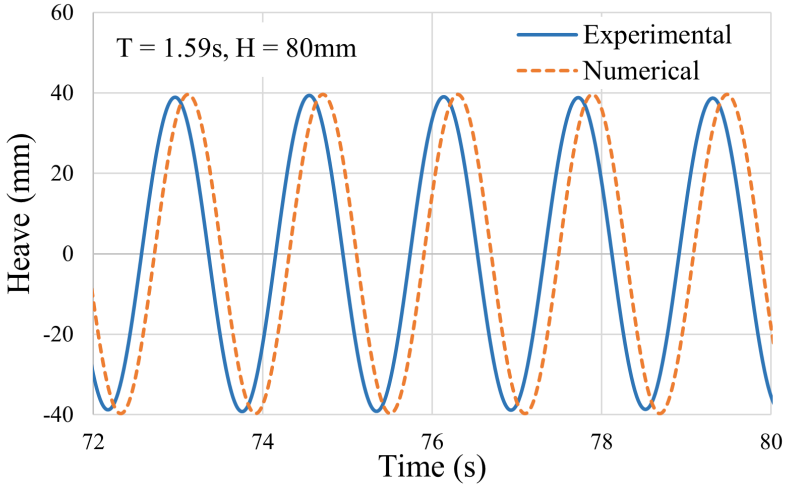

Figure D.6: Model scale heave displacement results of body 1 when subject to regular wave 8.

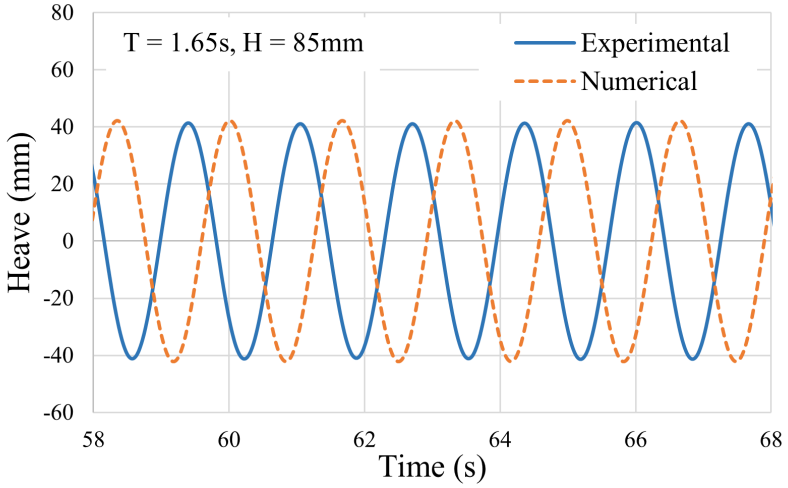

Figure D.7: Model scale heave displacement results of body 1 when subject to regular wave 9.

Appendix E

Mooring Tension

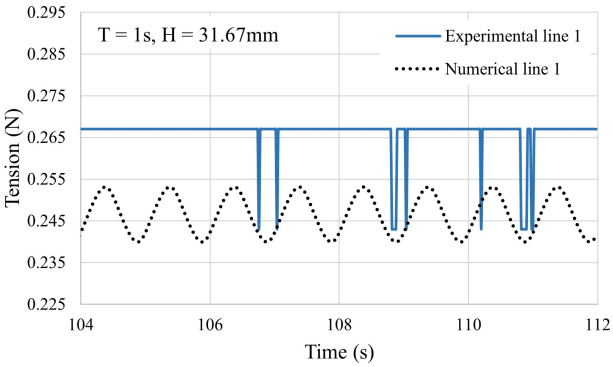

(a) Tension force in numerical and experimental line 1.

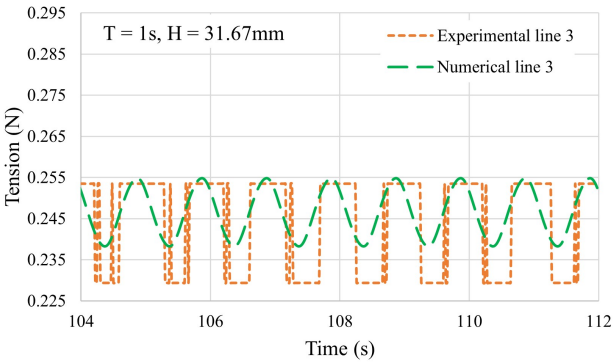

(b) Tension force in numerical and experimental line 3.

Figure E.1: Tension in mooring lines 1 (upwind) and 3 (downwind) during regular wave 1.

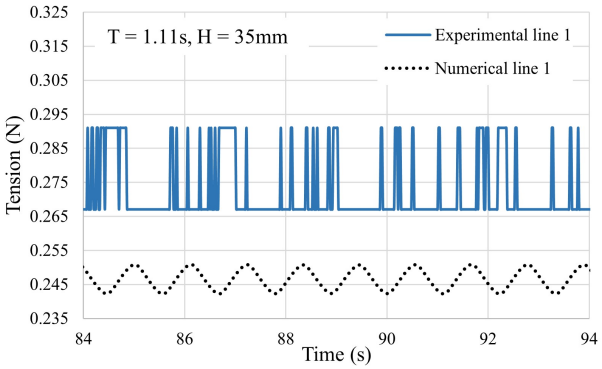

(a) Tension force in numerical and experimental line 1.

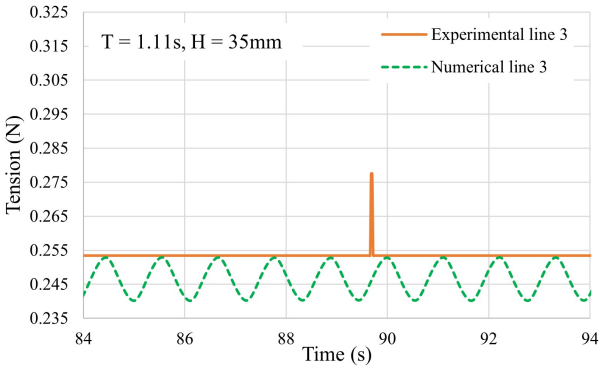

(b) Tension force in numerical and experimental line 3.

Figure E.2: Tension in mooring lines 1 (upwind) and 3 (downwind) during regular wave 2.

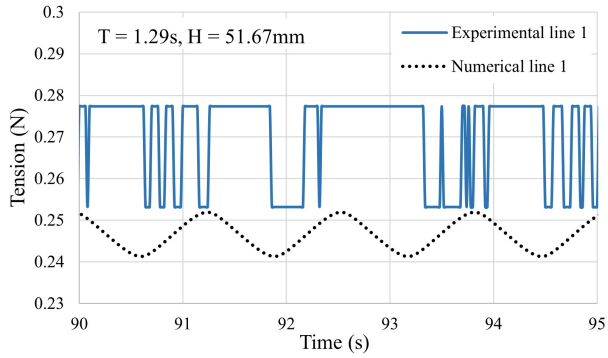

(a) Tension force in numerical and experimental line 1.

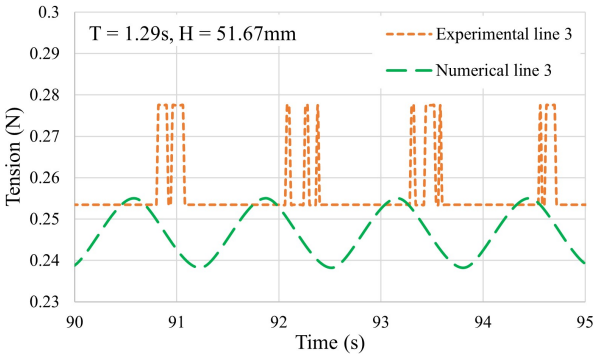

(b) Tension force in numerical and experimental line 3.

Figure E.3: Tension in mooring lines 1 (upwind) and 3 (downwind) during regular wave 4.

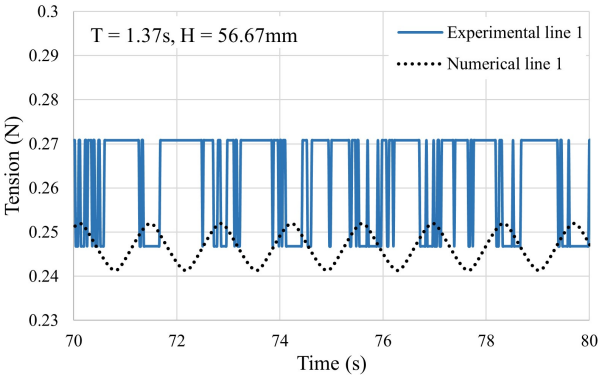

(a) Tension force in numerical and experimental line 1.

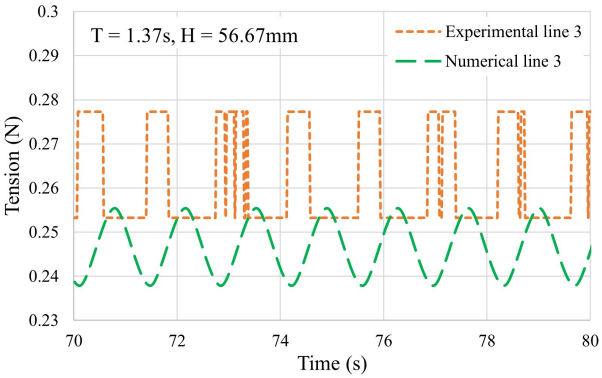

(b) Tension force in numerical and experimental line 3.

Figure E.4: Tension in mooring lines 1 (upwind) and 3 (downwind) during regular wave 5.

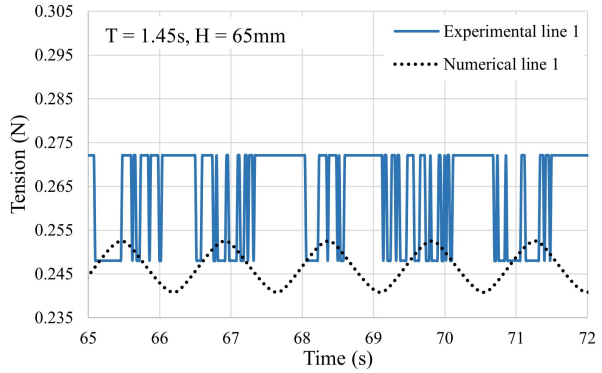

(a) Tension force in numerical and experimental line 1.

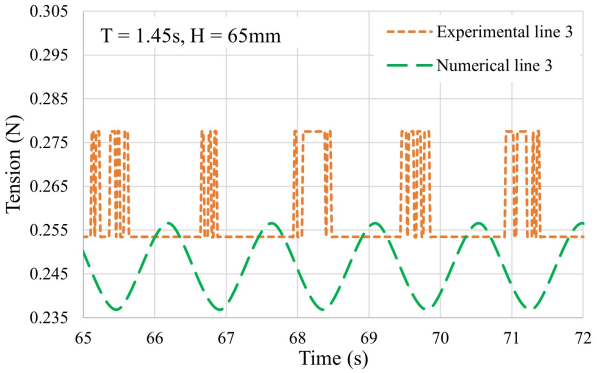

(b) Tension force in numerical and experimental line 3.

Figure E.5: Tension in mooring lines 1 (upwind) and 3 (downwind) during regular wave 6.

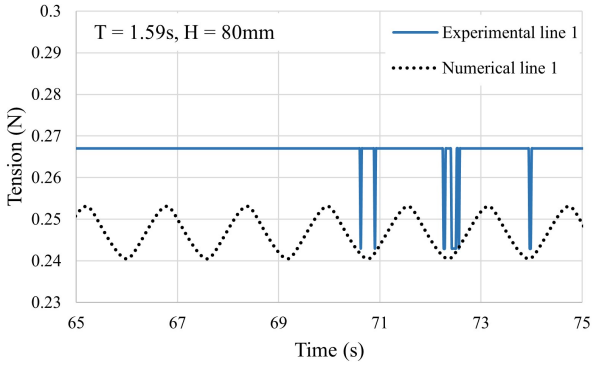

(a) Tension force in numerical and experimental line 1.

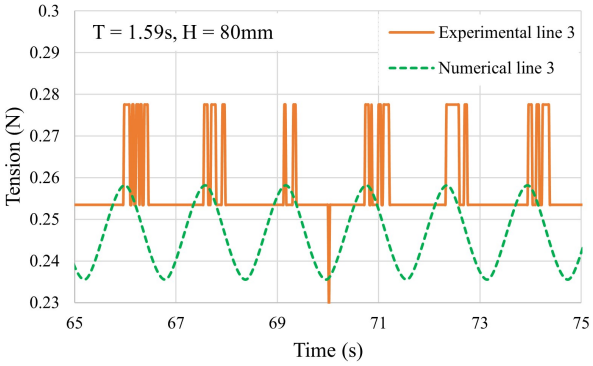

(b) Tension force in numerical and experimental line 3.

Figure E.6: Tension in mooring lines 1 (upwind) and 3 (downwind) during regular wave 8.

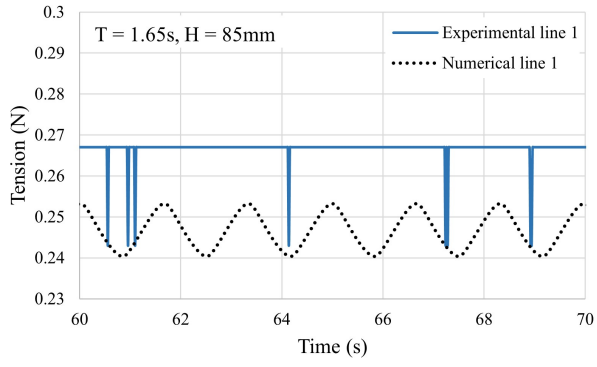

(a) Tension force in numerical and experimental line 1.

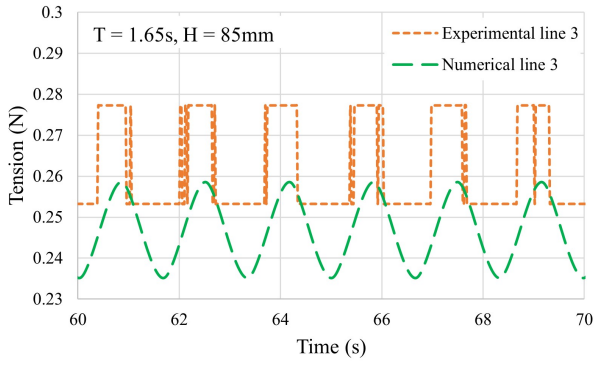

(b) Tension force in numerical and experimental line 3.

Figure E.7: Tension in mooring lines 1 (upwind) and 3 (downwind) during regular wave 9.

Appendix F

Connecting Rope Tension

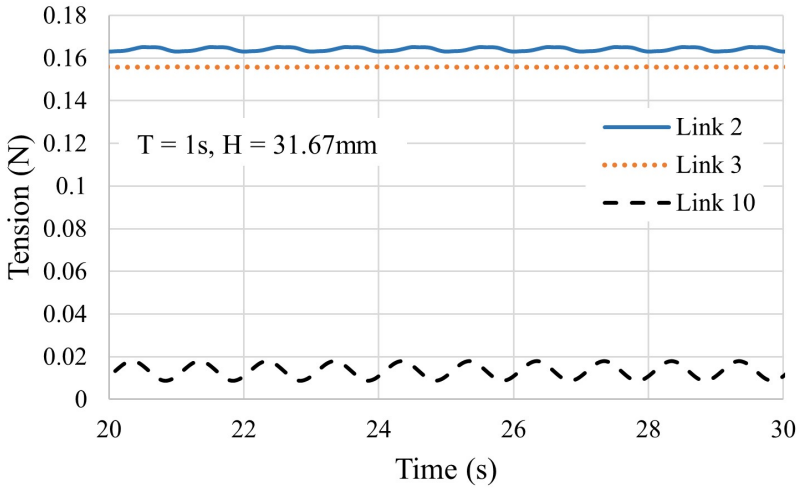

Figure F.1: Connecting rope tension in links 2, 3, and 10 during regular wave 1.

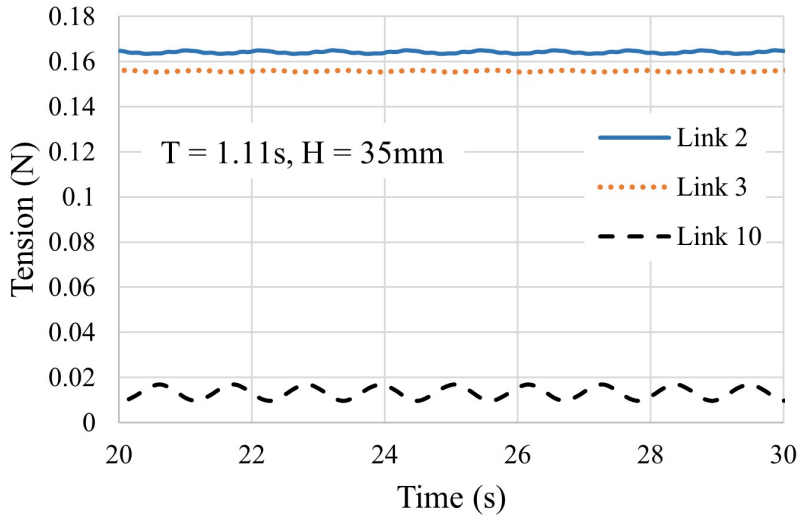

Figure F.2: Connecting rope tension in links 2, 3, and 10 during regular wave 2.

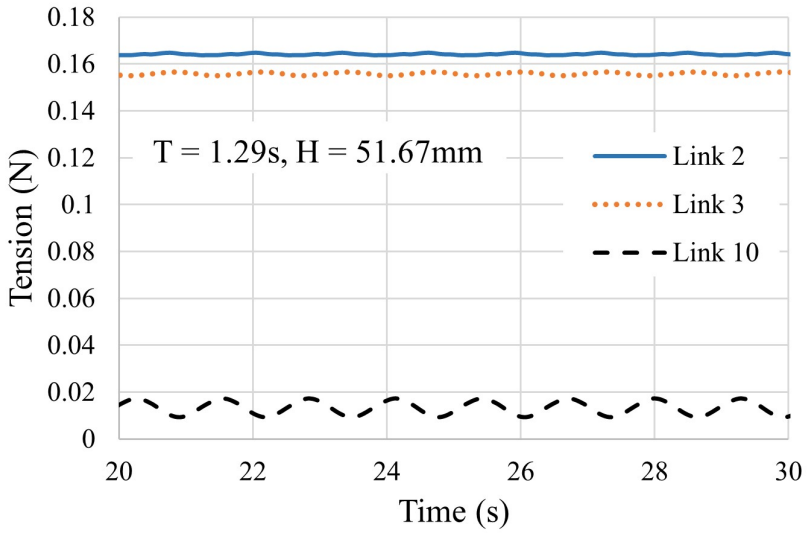

Figure F.3: Connecting rope tension in links 2, 3, and 10 during regular wave 4.

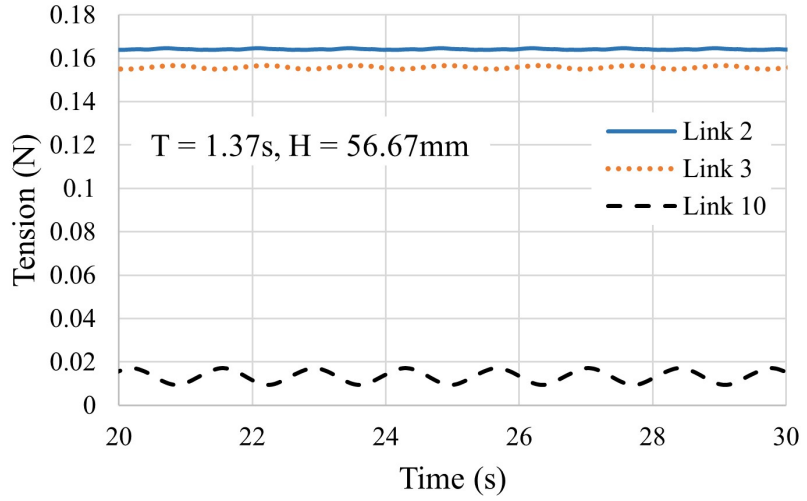

Figure F.4: Connecting rope tension in links 2, 3, and 10 during regular wave 5.

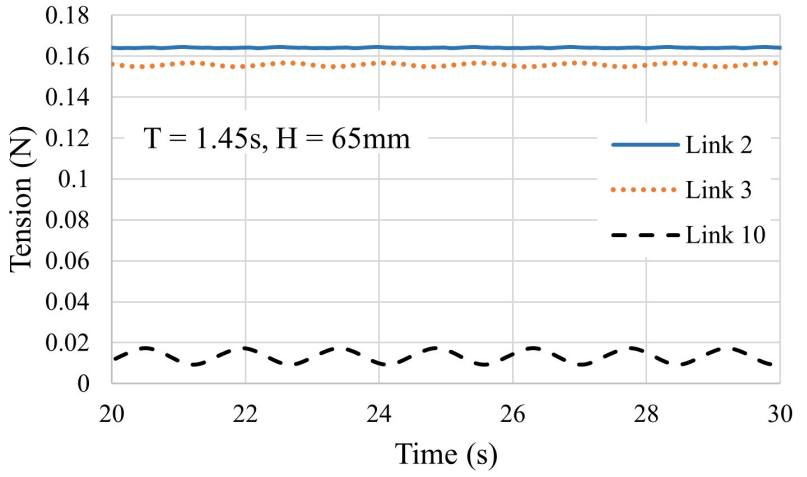

Figure F.5: Connecting rope tension in links 2, 3, and 10 during regular wave 6.

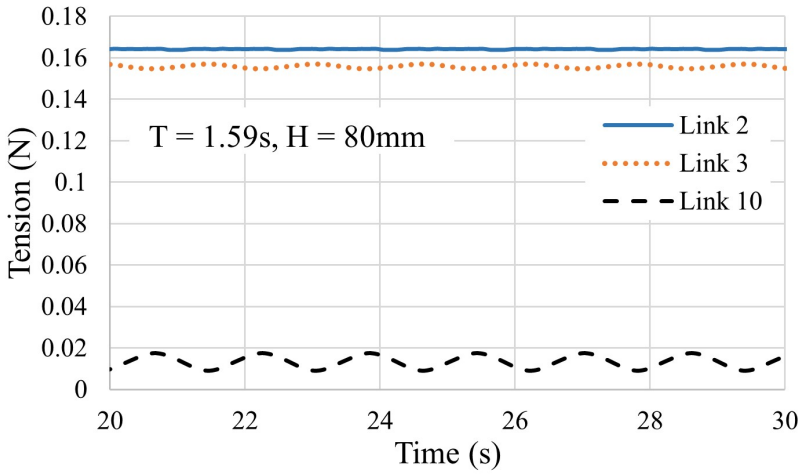

Figure F.6: Connecting rope tension in links 2, 3, and 10 during regular wave 8.

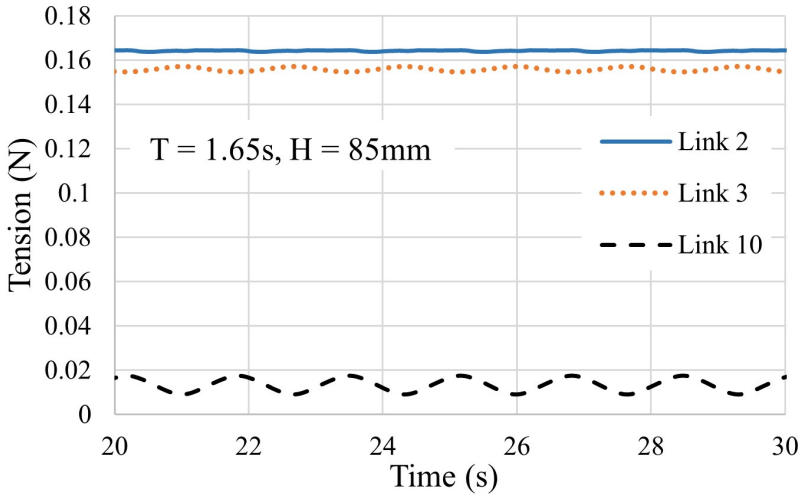

Figure F.7: Connecting rope tension in links 2, 3, and 10 during regular wave 9.

Appendix G

Modelling details in OrcaFlex

Centre of mass (mm):

x	y	z
0.0	0.0	1.736

Mass (kg):

0.0135

Moment of inertia tensor (kg.mm^2):

x	y	z
2.85	0.0	0.0
0.0	7.06	0.0
0.0	0.0	9.52

Inertia origin:

- ○ Body origin
- ○ Centre of mass
- ◉ User specified

User specified inertia origin (mm):

x	y	z
0.0	0.0	0.0

Figure G.1: OrcaWave 3x3 inertia matrix for the floating body.

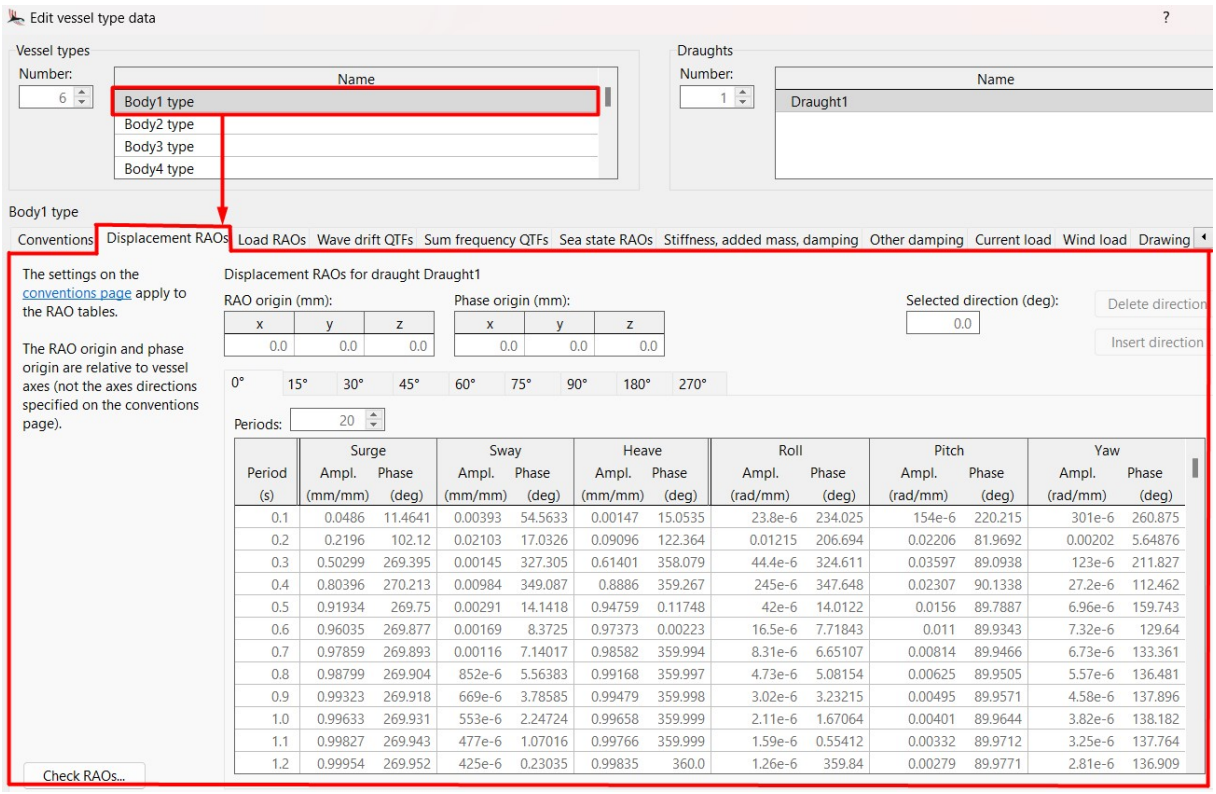

Period (s)	Surge Ampl. (mm/mm)	Surge Phase (deg)	Sway Ampl. (mm/mm)	Sway Phase (deg)	Heave Ampl. (mm/mm)	Heave Phase (deg)	Roll Ampl. (rad/mm)	Roll Phase (deg)	Pitch Ampl. (rad/mm)	Pitch Phase (deg)	Yaw Ampl. (rad/mm)	Yaw Phase (deg)
0.1	0.0486	11.4641	0.00393	54.5633	0.00147	15.0535	23.8e-6	234.025	154e-6	220.215	301e-6	260.875
0.2	0.2196	102.12	0.02103	17.0326	0.09096	122.364	0.01215	206.694	0.02206	81.9692	0.00202	5.64876
0.3	0.50299	269.395	0.00145	327.305	0.61401	358.079	44.4e-6	324.611	0.03597	89.0938	123e-6	211.827
0.4	0.80396	270.213	0.00984	349.087	0.8886	359.267	245e-6	347.648	0.02307	90.1338	27.2e-6	112.462
0.5	0.91934	269.75	0.00291	14.1418	0.94759	0.11748	42e-6	14.0122	0.0156	89.7887	6.96e-6	159.743
0.6	0.96035	269.877	0.00169	8.3725	0.97373	0.00223	16.5e-6	7.71843	0.011	89.9343	7.32e-6	129.64
0.7	0.97859	269.893	0.00116	7.14017	0.98582	359.994	8.31e-6	6.65107	0.00814	89.9466	6.73e-6	133.361
0.8	0.98799	269.904	852e-6	5.56383	0.99168	359.997	4.73e-6	5.08154	0.00625	89.9505	5.57e-6	136.481
0.9	0.99323	269.918	669e-6	3.78585	0.99479	359.998	3.02e-6	3.23215	0.00495	89.9571	4.58e-6	137.896
1.0	0.99633	269.931	553e-6	2.24724	0.99658	359.999	2.11e-6	1.67064	0.00401	89.9644	3.82e-6	138.182
1.1	0.99827	269.943	477e-6	1.07016	0.99766	359.999	1.59e-6	0.55412	0.00332	89.9712	3.25e-6	137.764
1.2	0.99954	269.952	425e-6	0.23035	0.99835	360.0	1.26e-6	359.84	0.00279	89.9771	2.81e-6	136.909

Figure G.2: Displacement RAOs imported from OrcaWave into OrcaFlex. There are 6 body types, one for each floating body in the FPV array.

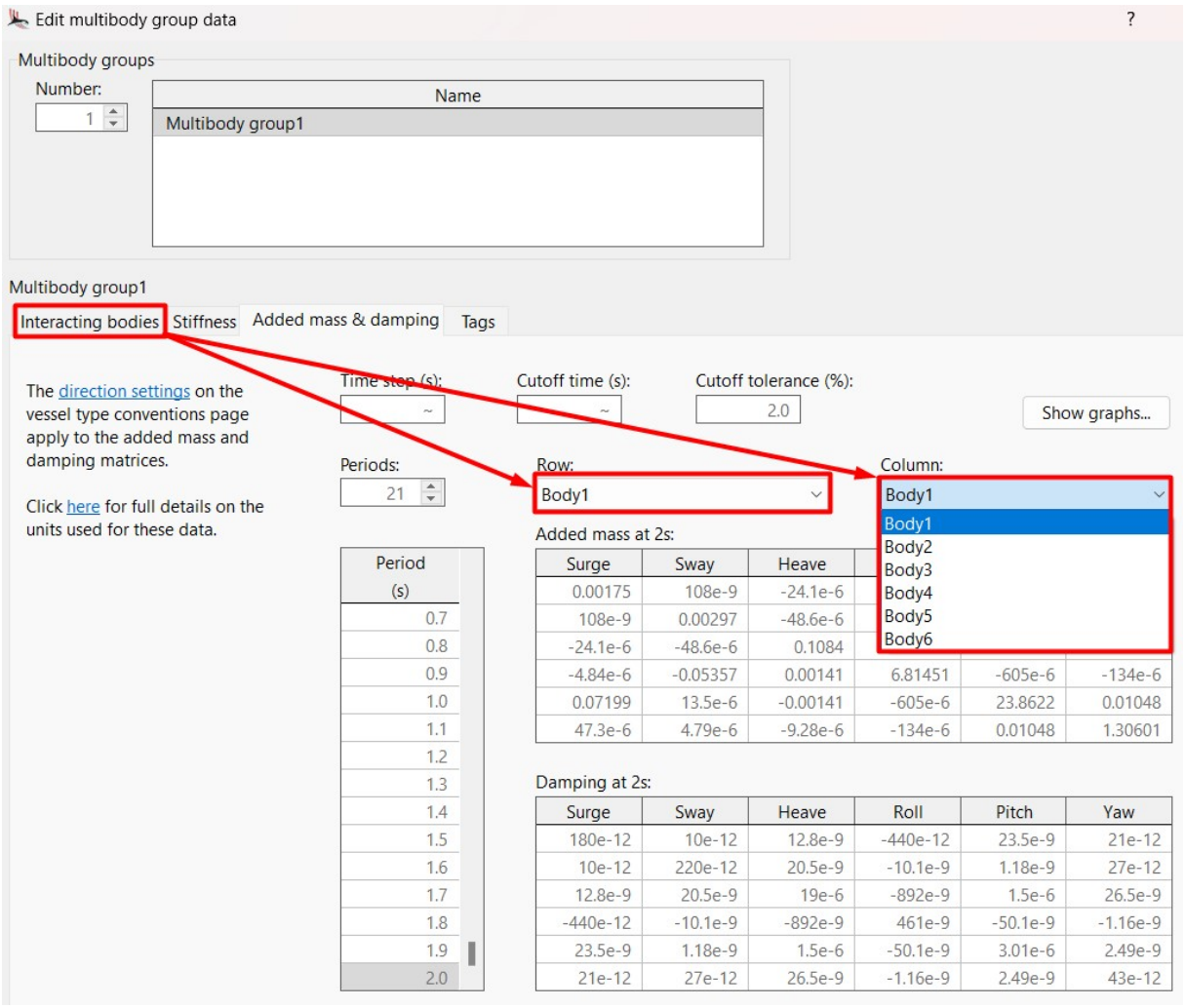

Figure G.3: Added mass and damping data imported from OrcaWave into OrcaFlex. The added mass and damping data is different for each body in the FPV array.

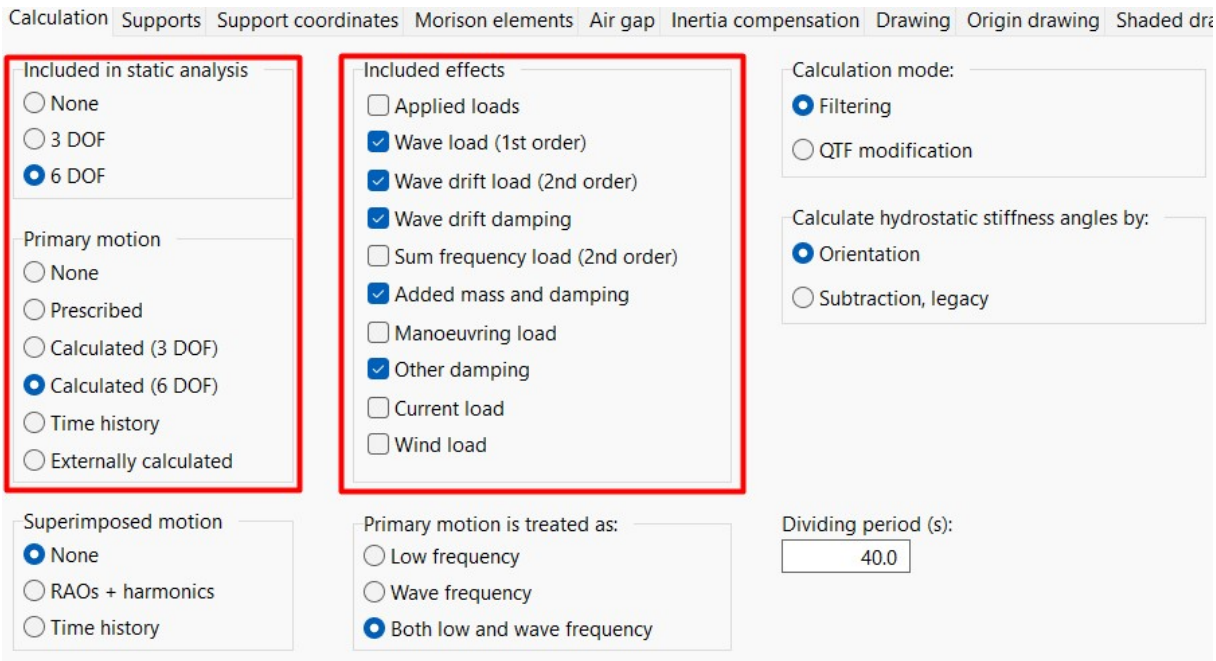

Figure G.4: OrcaFlex caculation interface for floating bodies.

Bibliography

[1] E. Kabir, P. Kumar, S. Kumar, A. A. Adelodun, and K.-H. Kim, "Solar energy: Potential and future prospects," *Renewable and Sustainable Energy Reviews*, vol. 82, pp. 894–900, 2018, (accessed: 15.05.2024), ISSN: 1364-0321. DOI: https://doi.org/10.1016/j.rser.2017.09.094. [Online]. Available: https://www.sciencedirect.com/science/article/pii/S1364032117313485.

[2] S. Oliveira-Pinto and J. Stokkermans, "Assessment of the potential of different floating solar technologies – overview and analysis of different case studies," *Energy Conversion and Management*, vol. 211, p. 112 747, 2020, ISSN: 0196-8904. DOI: https://doi.org/10.1016/j.enconman.2020.112747. [Online]. Available: https://www.sciencedirect.com/science/article/pii/S0196890420302855.

[3] E. Cuce, P. M. Cuce, S. Saboor, A. Ghosh, and Y. Sheikhnejad, "Floating pvs in terms of power generation, environmental aspects, market potential, and challenges," *Sustainability*, vol. 14, no. 5, 2022, ISSN: 2071-1050. DOI: 10.3390/su14052626. [Online]. Available: https://www.mdpi.com/2071-1050/14/5/2626.

[4] J. Song, H. Imani, J. Yue, and S. Yang, "Hydrodynamic characteristics of floating photovoltaic systems under ocean loads," *Journal of Marine Science and Engineering*, vol. 11, no. 9, 2023, (accessed: 15.05.2024), ISSN: 2077-1312. DOI: 10.3390/jmse11091813. [Online]. Available: https://www.mdpi.com/2077-1312/11/9/1813.

[5] M. Ikhennicheu, A. Blanc, B. Danglade, and J.-C. Gilloteaux, "Orcaflex modelling of a multi-body floating solar island subjected to waves," *Energies*, vol. 15, no. 23, 2022, (accessed: 15.05.2024), ISSN: 1996-1073. DOI: 10.3390/en15239260. [Online]. Available: https://www.mdpi.com/1996-1073/15/23/9260.

[6] Z. Jiang, J. Dai, S. Saettone, *et al.*, "Design and model test of a soft-connected lattice-structured floating solar photovoltaic concept for harsh offshore conditions," *Marine Structures*, vol. 90, p. 103 426, 2023, (accessed: 25.03.2024), ISSN: 0951-8339. DOI: https://doi.org/10.1016/j.marstruc.2023.103426. [Online]. Available: https://www.sciencedirect.com/science/article/pii/S095183392300059X.

[7] K. Mertens, *Photovoltaic - Fundamentals, Technology, and Practice*. Wiley, 2018, ISBN: 9781119401049, (accessed: 01.05.2023).

[8] A. Sahu, N. Yadav, and K. Sudhakar, "Floating photovoltaic power plant: A review," *Renewable and Sustainable Energy Reviews*, vol. 66, pp. 815–824, 2016, ISSN: 1364-0321. DOI: https://doi.org/10.1016/j.rser.2016.08.051. [Online]. Available: https://www.sciencedirect.com/science/article/pii/S1364032116304841.

[9] J. Journée and W. Massie, *Offshore Hydromechanics*, 1st ed. Delft, the Netherlands: Delft University of Technology, 2001.

[10] M. Chrolenko, "Dynamic analysis and design of mooring lines," (accessed: 09.05.2024), Master's thesis, Norwegian University of Science and Technology, Department of Marine Technology, Jun. 2013. [Online]. Available: https://ntnuopen.ntnu.no/ntnu-xmlui/bitstream/handle/11250/238576/648748_FULLTEXT01.pdf?sequence=3.

[11] Y. Bai and W.-L. Jin, *Marine Structural Design*. Oxford: Butterworth-Heinemann, 2019, (accessed: 09.05.2024). [Online]. Available: https://books.google.no/books?id=Bx2bDwAAQBAJ.

[12] K. Trapani and D. L. Millar, "The thin film flexible floating pv (t3f-pv) array: The concept and development of the prototype," *Renewable Energy*, vol. 71, pp. 43–50, 2014, ISSN: 0960-1481. DOI: https://doi.org/10.1016/j.renene.2014.05.007. [Online]. Available: https://www.sciencedirect.com/science/article/pii/S0960148114002584.

[13] pv magazine. "Offshore floating PV demonstrator to go online on belgium's north sea coast." (accessed: 22.05.2024). (Jul. 2023), [Online]. Available: https://www.pv-magazine.com/2023/07/25/offshore-floating-pv-demonstrator-to-go-online-on-belgiums-north-sea-coast/.

[14] A. H. Techet, Massachusetts Institute of Technology: MIT OpenCourseWare, *Design principles for ocean vehicles 13.42 - wave spectra*, (accessed: 29.04.2024), 2005. [Online]. Available: https://ocw.mit.edu/courses/2-22-design-principles-for-ocean-vehicles-13-42-spring-2005/3fd34b15f4d9ddbe167697b3c4e7cca5_r8_wavespectra.pdf.

[15] J. N. Newman, *Marine Hydrodynamics*. Cambridge: The MIT Press, 2018, (accessed: 09.04.2024), ISBN: 9780262534826. [Online]. Available: https://library.oapen.org/handle/20.500.12657/26039.

[16] F. M. White, *Fluid Mechanics*, 7th ed. New York: McGraw-Hill Education, 2011, ISBN: 9780073529349.

[17] K. Saitov, *Hydrodynamic analysis of a floating photovoltaic concept*, Unpublished, 2023.

[18] A. H. Techet, Massachusetts Institute of Technology: MIT OpenCourseWare, *Hydrodynamics 13.012 - linear potential theory*, (accessed: 28.04.2024), 2005. [Online]. Available: https://ocw.mit.edu/courses/2-016-hydrodynamics-13-012-fall-2005/c472432debcf6ee250209b68cf18cc1
2005reading4.pdf.

[19] Orcina, *Vessel theory, impulse response and convolution*, (accessed: 02.05.2024), 2023. [Online]. Available: https://www.orcina.com/webhelp/OrcaFlex/Content/html/Vesseltheory,Impulseresponseandconvolution.htm.

[20] Orcina, *Results: Displacement RAOs*, (accessed: 22.03.2024), 2023. [Online]. Available: https://www.orcina.com/webhelp/OrcaWave/Content/html/Results,DisplacementRAOs.htm#:~:text=The%20displacement%20RAOs%20for%20all%20other%20degrees%20of,equation%20is%20written%20using%20the%20summation%20convention%2C%20and.

[21] S. Steen, *Experimental Methods in Marine Hydrodynamics*. Trondheim, Norway: Norwegian University of Science and Technology (NTNU), Aug. 2014, Lecture Notes, TMR7.

[22] J. H. Todalshaug, "Hydrodynamics of wecs," in *Handbook of Ocean Wave Energy*, A. Pecher and J. P. Kofoed, Eds. Cham: Springer International Publishing, 2017, pp. 139–158, (accessed: 24.03.2024), ISBN: 978-3-319-39889-1. DOI: 10.1007/978-3-319-39889-1_6. [Online]. Available: https://doi.org/10.1007/978-3-319-39889-1_6.

[23] O. M. Faltinsen, *Sea Loads on Ships and Offshore Structures*. Cambridge, UK: Cambridge University Press, 1990, ISBN: 0521458706.

[24] Orcina, *OrcaWave - introduction*, (accessed: 18.04.2024), 2023. [Online]. Available: https://www.orcina.com/webhelp/OrcaWave/Content/html/Introduction.htm.

[25] Orcina, *Vessel data: Calculation data*, (accessed: 08.05.2024). [Online]. Available: https://www.orcina.com/webhelp/OrcaFlex/Content/html/Vesseldata,Calculationdata.htm.

[26] Orcina, *Lines*, (accessed: 04.05.2024), 2023. [Online]. Available: https://www.orcina.com/webhelp/OrcaFlex/Content/html/Lines.htm.

[27] Orcina, *Line type wizard*, (accessed: 03.05.2024), Orcina, 2023. [Online]. Available: https://www.orcina.com/webhelp/OrcaFlex/Content/html/Linetypewizard.htm.

[28] Orcina, *Links: Data*, accessed: 31.03.2024), 2023. [Online]. Available: https://www.orcina.com/webhelp/OrcaFlex/Content/html/Links,Data.htm.

[29] Orcina, *Winches*, (accessed: 07.04.2024), 2023. [Online]. Available: https://www.orcina.com/webhelp/OrcaFlex/Content/html/Winches.htm.

[30] Orcina, *Constraints*, (accessed: 07.04.2024), 2023. [Online]. Available: https://www.orcina.com/webhelp/OrcaFlex/Content/html/Constraints.htm.

[31] Orcina, *Modal analysis, data and results*, (accessed: 03.05.2024), 2023. [Online]. Available: https://www.orcina.com/webhelp/OrcaFlex/Content/html/Modalanalysis,Dataandresults.htm.

[32] Orcina, *Modal analysis: Theory*, (accessed: 03.05.2024), 2023. [Online]. Available: https://www.orcina.com/webhelp/OrcaFlex/Content/html/Modalanalysis,Theory.htm.

[33] Orcina, *Vessel types: Other damping*, (accessed: 08.05.2024), 2023. [Online]. Available: https://www.orcina.com/webhelp/OrcaFlex/Content/html/Vesseltypes,Otherdamping.htm.

[34] Orcina, *Orcina: Leading the Way in Offshore Dynamics*, (accessed: 02.03.2024). [Online]. Available: https://www.orcina.com/.

[35] Orcina, *OrcaFlex: The World's Leading Software for Offshore Dynamic Analysis*, (accessed: 02.03.2024). [Online]. Available: https://www.orcina.com/orcaflex/.

[36] Orcina, *OrcaFlex Specification: Detailed Technical Information*, (accessed: 02.03.2024). [Online]. Available: https://www.orcina.com/orcaflex/specification/.

[37] DNV GL. "Conceptual modelling of offshore and maritime structures - genie." (accessed: 25.03.2024). (2023), [Online]. Available: https://www.dnv.com/services/conceptual-modelling-of-offshore-and-maritime-structures-genie-89128/.